แขนกล 6 องศาอิสระ สำหรับงานขนาดเล็ก

นายสุภชัย วงศ์บุณย์ยง

วิทยานิพนธ์นี้เป็นส่วนหนึ่งของการศึกษาตามหลักสูตรปริญญาวิศวกรรมศาสตรมหาบัณฑิต
สาขาวิชาวิศวกรรมเครื่องกล ภาควิชาวิศวกรรมเครื่องกล
คณะวิศวกรรมศาสตร์ จุฬาลงกรณ์มหาวิทยาลัย
ปีการศึกษา 2551

A 6-DOF MANIPULATOR FOR MINIATURE TASKS

Mr. Supachai Vongbunyong

A Thesis Submitted in Partial Fulfillment of the Requirements
for the Degree of Master of Engineering Program in Mechanical Engineering
Department of Mechanical Engineering
Faculty of Engineering
Chulalongkorn University
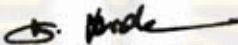Academic year 2008
Copyright of Chulalongkorn University

511746

Thesis Title   A 6-DOF MANIPULATOR FOR MINIATURE TASKS

By   Mr. Supachai Vongbunyong

Filed of study   Mechanical Engineering

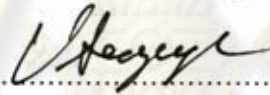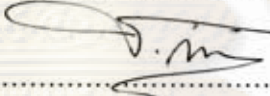Advisor   Associate Professor Viboon Sangveraphunsiri, Ph.D.

Accepted by the Faculty of Engineering, Chulalongkorn University in Partial Fulfillment of the Requirements for the Master's Degree

.... Dean of the Faculty of Engineering

(Associate Professor Boonsom Lerdhirunwong, Dr.Ing.)

THESIS COMMITTEE

.... Chairman

(Assistant Professor Witaya Wannasuphoprasit, Ph.D.)

.... Advisor

(Associate Professor Viboon Sangveraphunsiri, Ph.D.)

.... Examiner

(Associate Professor Chairote Kunpanitchakit, Ph.D.)

.... Examiner

(Associate Professor Ratchatin Chanchareon, Ph.D.)

สุภชัย วงศบุณย์ยง : แขนกล 6 องศาอิสระสำหรับงานขนาดเล็ก.
(A 6-DOF Manipulator for Miniature Tasks) อ. ที่ปรึกษาวิทยานิพนธ์หลัก : รศ.ดร.วิบูลย์
แสงวีระพันธุ์ศิริ, 159 หน้า.

งานวิจัยนี้เป็นการศึกษาระบบแขนกลแบบนำ-ตาม หรือระบบควบคุมระยะไกล 6 องศาอิสระ
สำหรับทำงานขนาดเล็กทั่วไป แขนกลตามในงานวิจัยนี้ได้ออกแบบโดยใช้โครงสร้างแบบอนุกรม ซึ่ง
การออกแบบได้พิจารณาเน้นถึงพื้นที่การทำงาน การเข้าถึงงาน และความสะดวกในการตอบสนอง
กับผู้ใช้ สำหรับพื้นที่ในการทำงานนั้น ระบบถูกออกแบบให้สามารถใช้งานสับเปลี่ยนกันได้ระหว่าง
การทำงานสองลักษณะคือ การเคลื่อนที่แบบหยาบ และการเคลื่อนที่แบบละเอียด สำหรับการ
เคลื่อนที่แบบหยาบจะถูกใช้เพื่อการเคลื่อนที่อย่างรวดเร็วภายในพื้นที่ทำงาน ในขณะที่การเคลื่อนที่
แบบละเอียดจะถูกใช้เพื่อการเข้าถึงงานและทำงานในบริเวณเล็กๆที่ต้องการความแม่นยำ นอกจากนี้
รูปแบบโครงสร้างของแขนกลตามได้ถูกออกแบบให้สัมพันธ์กับแขนกลนำ เพื่อเพิ่มความสามารถใน
การบังคับของผู้ใช้ด้วย ในงานวิจัยนี้แขนกลนำแฟนท่อม ออมนิ (Phantom Omni®) ซึ่งเป็น
ผลิตภัณฑ์จากบริษัท เซนเซเบิล เทคโนโลยี ได้ถูกเลือกมาใช้เป็นแขนกลนำ เนื่องจากมีอุปกรณ์
ตรวจรู้สำหรับวัดการเคลื่อนที่ได้ถึง 6 องศาอิสระ ซึ่งเพียงพอต่อการระบุตำแหน่ง และการวางตัว ใน
การควบคุมแขนกลตาม สำหรับการทดสอบนั้น ได้ทำการติดตั้งกล้องวงจรปิดเข้ากับระบบเพื่อ
บันทึกภาพเคลื่อนไหวตลอดการทำงาน เพื่อให้ผู้ใช้สามารถเห็น และ บังคับการทำงานของแขนกล
ได้สะดวกมากยิ่งขึ้น

ภาควิชา   วิศวกรรมเครื่องกล   ลายมือชื่อนิสิต _____
สาขาวิชา   วิศวกรรมเครื่องกล   ลายมือชื่ออาจารย์ที่ปรึกษาวิทยานิพนธ์หลัก _____
ปีการศึกษา _____ 2551 _____

4870629121 : MAJOR MECHANICAL ENGINEERING

KEYWORDS : MASTER SLAVE SYSTEM / ROBOT FOR MINIATURE TASKS

SUPACHAI VONGBUNYONG : A 6-DOF MANIPULATOR FOR MINIATURE TASKS.
ADVISOR : ASSOC.PROF.VIBOON SANGVERAPHUNSIRI, Ph.D., 159 pp.

This research work is a novel design of a general purpose 6-DOF master-slave system for miniature tasks. The work focuses on design of a slave manipulator based on a serial mechanism. Many significant criteria are considered in the design process, for instance, workspace, task approach, and comfortable user interaction. Concerning the workspace and task approach, the slave robot was designed to operate in both large (coarse motion) and limited space (fine motion) by switching between coarse and fine control scheme. The coarse one will be applied for moving in large travelling distances. On the other hands, another scheme will be used for approaching and working with-in the small workspace delicately. Furthermore, its configurations are formed based on the master device, which can be performed effectively by an operator. In this case, Phantom Omni, a commercial haptic device from Sensible Technologies Company, is selected as the master arm. Thanks to its 6-DOF positional sensing, this device can provide enough motion information, 3 for positions and 3 for orientation, to control the slave manipulator. Finally, in the experimental setup, a CCTV camera with high scale zooming is installed in the system to improve operation as an operator can view real-time images during performing a miniature task.

ศูนย์วิทยทรัพยากร
จุฬาลงกรณ์มหาวิทยาลัย

Department : __Mechanical Engineering__ Student's Signature : _____

Field of Study : __Mechanical Engineering__ Advisor's Signature : _____

Academic Year : _____2008_____

ACKNOWLEDGEMENTS

CONTENTS

LIST OF TABLES

LIST OF FIGURES

ศูนย์วิทยทรัพยากร
จุฬาลงกรณ์มหาวิทยาลัย

CHAPTER I

INTRODUCTION

1.1 Motivation and objective of study

At present, robotic manipulators are used in many applications because of their ability to work in some specific tasks, especially accurate and precise work. A lot of these applications have been presented in many fields, especially medical techniques. Overall, many topics relating to the manipulator that serves specific tasks have been continuously researched and developed.

In addition to concept of conventional robots that have been pre-programmed to perform repeated task, a master-slave robotic system is partially different. The major concept of master-slave robotic system (or teleoperation system) is to merge ability among human being and robots. The human being has great ability in decision making while the robots are more enduring, precise, and accurate. Moreover, as regard to physical constraints, mechanism of robots can be designed more suitable for specific works than human's body. In brief, this robotic system can provide outstanding advantage and serve a number of applications.

The master-slave robotic system with high precision and accuracy is widely used in a number of specific and complicated applications; for example the Minimally Invasive Surgery (MIS) [1]. This kind of surgery is operated through small incisions using specialized techniques. All small devices consisted of manipulators, small cameras, and a flash-light will be penetrated and operated through these incisions on patients' body. The most significant benefit of this technique is to allow the patients recover much faster than the conventional surgery. Furthermore, this system is also widely used in many industries, such as microelectronic industries, small parts assembly, micro-sized particles handling.

In conclusion, this research covers details in design and control of a multi-purpose master-slave system for miniature tasks. Mechanical design, manufacturing, mathematics computation and control scheme are clearly described in this document.

1.2 Objectives

1.2.1 Design, build, and control a 6-DOF manipulator.

1.2.2 Able to control position and orientation according to desired movement paths.

1.2.3 Able to work with a 6-DOF master arm device.

1.2.4 Study the concept of co-operated work between human and robots.

1.3 Outline of thesis

1.3.1 Design, build, and control a manipulator which appropriates for miniature tasks, with 0.1 mm. resolution.

1.3.2 Able to control position and orientation according to desired movement paths.

1.3.3 Able to work with a 6-DOF master arm device.

1.4 Procedures

1.4.1 Literature review.

1.4.2 Design mechanical configurations of the manipulator, manufacture and analyze a basic prototype mechanism.

1.4.3 Simulate the manipulator with appropriate software.

1.4.4 Design in details and manufacture parts of the manipulator.

1.4.5 Assembly the robot, revise and correct any errors that may occur.

1.4.6 Design the motion control system based on PID control scheme.

1.4.7 Test the basic movements.

1.4.8 Connect the manipulator with the master arm (Phantom Omni® Haptic Device).

1.4.9 Test the master-slave system movements.

1.4.10 Test overall system and conclusion.

1.5 Benefits

1.5.1 Obtain the multi-purpose 6-DOF manipulator with a large workspace and sufficient precision for miniature tasks.

1.5.2 The manipulator can be used as a 6-DOF slave manipulator in master-slave operation.

1.5.3 The manipulator can be further used as a test bed for advanced controls and force controls.

1.5.4 The manipulator can be developed to specific and suitable applications in many fields, namely industrial, science, and medical.

CHAPTER II

LITERATURE REVIEW AND GENERAL KNOWLEDGE

This chapter gives information of manipulators typically used in performing miniature tasks. Moreover, some mathematics model are presented for some mechanical system

2.1 Literature reviews on a manipulator for miniature tasks

2.1.1 Manual manipulator

Most of the manipulators that have been designed for manipulating very small objects are operate manually. The typical purpose is to handle, probe, and interact with the small items e.g. MEMs and biological samples. The resolution ranges between 1 micron and 1 mm according to specific purposes. Furthermore, the precise movements in orthogonal directions (X-Y-Z) are allowed. The structures are typically based on simple linear stages and rotary stages.

Figure 2.1: MM110 and MM525 Bio/MEMS Manipulators [2]

Figure 2.1 shows two commercial products from Micromanipulator Company [2]. These manual manipulators are designed for different applications. Therefore, their configurations and precision are significantly different. First, the MM110 model is designed for manipulating >10 micron objects such as biological samples. Second, the

MM525 model is designed for manipulating >1 micron objects and commonly used with MEMS products.

2.1.2 Robotic manipulator

Robotic manipulators for miniature tasks can be generally used in a number of specific applications such as handling micro protein crystal [3], electronic parts assembly, and MEMs manipulation. However, most of them are operate by human as a master-slave system.

Nowadays, the number of research in the area of the master-slave system, especially in medical application, is dramatically increased. Most of the research currently focus on the activities consisted of the MIS, eye surgery, ultrasonic probing etc. They are continuously developed to the practical products

Apparently, applications of MIS or surgical assisted system are definitely interesting. Thereby, many robotic systems relating to MIS are commercially available, including ZEUS[TM] Surgical System [4] and DaVinci[®] Surgical System [5]. Furthermore, other research about medical application is dexterous system for laryngeal surgery [6], a steady-hand manipulator for retinal surgery [7] etc. The details of these MIS systems are described as follows

2.1.2.1 The ZEUS[TM] Surgical System

The ZEUS[TM] Robotic Surgical System is manufactured by Computer Motion, Inc. The system typically consists of a surgeon console and three slave robotic arms at the patient-side. The three robotic arms are used for different purposes. The first two arms are used to manipulate the surgical devices while another is arm used to hold the endoscope sending 2D or 3D visual feedbacks to the operator console. During the operation, the surgeon can control both manipulators through two handles on the console. The manipulators and surgical devices are approximately 5 mm in diameter. They are able to provide 5 DOF motion for the device tips. The ZEUS[TM] Surgical System is shown in Figure 2.2.

Figure 2.2: Three arms at a patient-side and a surgeon console of
The ZEUS^{TM} Robotic Surgical System [4]

2.1.2.2 The DaVinci$^{®}$ Surgical System

The DaVinci$^{®}$ Surgical System is manufactured by Intuitive Surgical, Inc. This system comprises a surgeon console and a patient-side robotic cart with four 7-DOF robotic arms. Three of them are used to manipulate surgical devices while another one is used to hold a high-resolution 3D endoscope camera. The patent surgical devices, named "EndoWrist$^{®}$", are mounted on these manipulators. These devices are approximately 5 mm and 8 mm in diameter (see Figure 2.4). The size is depended on each device type. In general, the surgeon commonly uses only two manipulators as the left and the right hand but the DaVinci$^{®}$ surgical system provides the optional arm. The optional arm (the 4th arm) performs additional tasks like applying countertraction and following running sutures without assistance from other surgeons. Moreover, the intelligent system scales and translates the surgeon's movements to more precise movements of the manipulators. The DaVinci$^{®}$ Robotic Surgical System is shown in Figure 2.3.
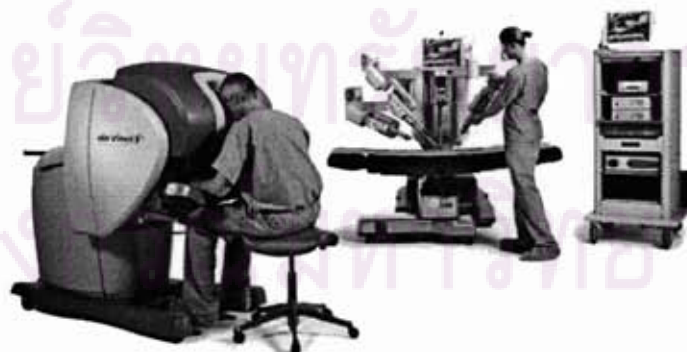
Figure 2.3: A patient-side cart and a surgeon console of
the DaVinci$^{®}$ Surgical System [5]
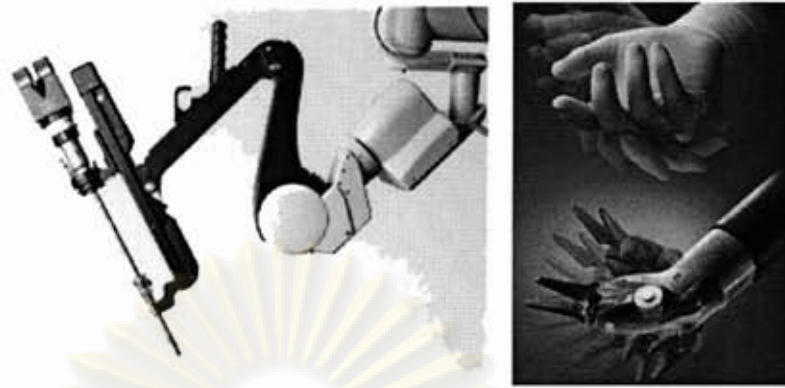
Figure 2.4 the DaVinci® Surgical System manipulator and EndoWrist® [5]

2.2 Manipulator mechanism

The general mechanism of the manipulator is categorized into two types according to its configuration of the kinematics chain: a serial mechanism and a parallel mechanism. The serial manipulator is commonly used in industry for a long time while the parallel manipulator is quite novel. Overall, advantage and disadvantage of them are shown in Table 1 [8].

Table 2.1: Qualification comparison between a serial and a parallel mechanism

	Serial Manipulator	Parallel Manipulator
1. Workspace	✓	
2. Load Capacity		✓
3. Stiffness		✓
4. Inertia		✓
5. Kinematics Complexity		
- Forward Kinematics	✓	Complex
- Inverse Kinematics	Complex	✓
6. Design Complexity	✓	

✓ represent advantage

2.2.1 Serial mechanism

Large workspace and relatively more simple in structure are the main advantage of the serial mechanism. On the other hand, location of actuators is the main drawbacks. Because, the actuators are located on the moving links, the manipulator has to carry and move large weight with respect to actuators the whole time. Consequently, this arrangement of the actuator leads to very high inertia. Furthermore, according to the nature of the open-loop or open-kinematics structure, this kind of manipulator has low stiffness and can manipulate relatively small loads. Due to these reasons, errors are also cumulative and amplified from link to link.

However, the serial manipulators are generally used in many industrial works, including pick-and-place, part assembly, welding, spraying etc. The notable examples of commercial serial manipulator are PUMA560, Mitsubishi PA-10 [9], and Motoman's HP200 [10] (see Figure 2.5).

(a)   (b)
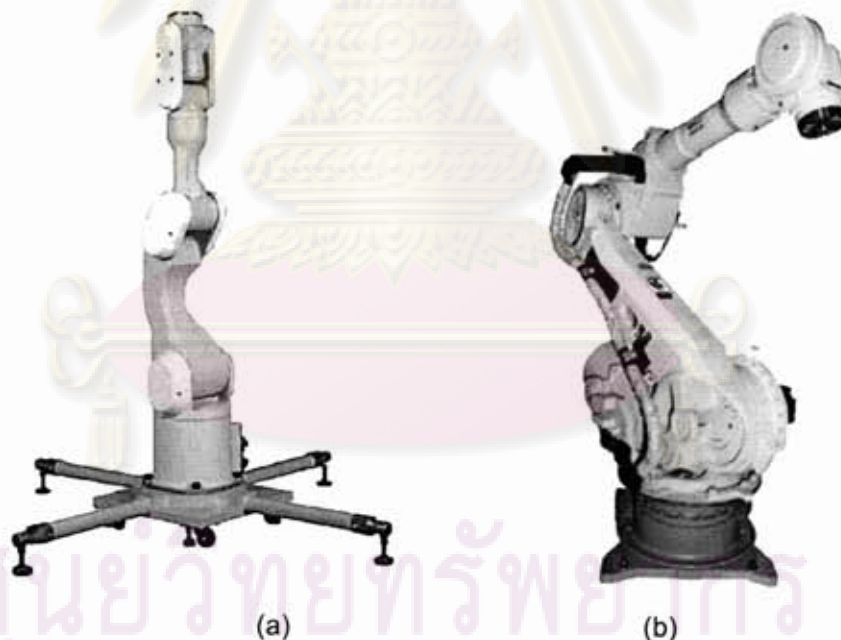
Figure 2.5: Mitsubishi PA10 [9] (a) and Motoman's HP200 [10] (b)

2.2.2 Parallel mechanism

Due to the closed-loop kinematics structure, every actuator can be located on the base. This structure makes the parallel manipulators have considerably high

stiffness and low inertia. Consequently, the manipulators are able to carry large load and move very fast. Furthermore, error accumulation is significantly low.

However, very limited workspace is main disadvantage of parallel manipulators. Therefore, this type of manipulator is rarely used in real application; for example Stewart Platform, Hexapod, Adept Quattro [11].

The Adept Quattro [11] is manufactured by Adept Technology, Inc. This manipulator obviously represents the advantage of the parallel mechanism. It has been designed for high-speed work such as packaging and part assembly (see Figure 2.6).
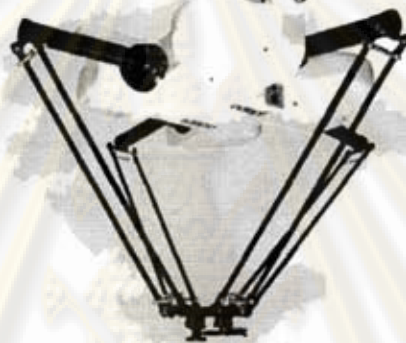
Figure 2.6: Adept Quattro [11]

2.2.3 Hybrid serial - parallel mechanism

Hybrid serial-parallel manipulators merge the outstanding features between serial and parallel mechanism. Large workspace, low stiffness, and high stiffness can be obtained from the proper design. The manipulators can be designed based on each requirement. There are a number of researches that design based on this mechanism; namely, a parallel hybrid micro-SCARA robot for high precision assembly [12] (see Figure 2.7), a 5-DOF hybrid micro-manipulator for medical applications [13] (see Figure 2.8), and a new laparoscope manipulator with an optical zoom [14] (see Figure 2.9).
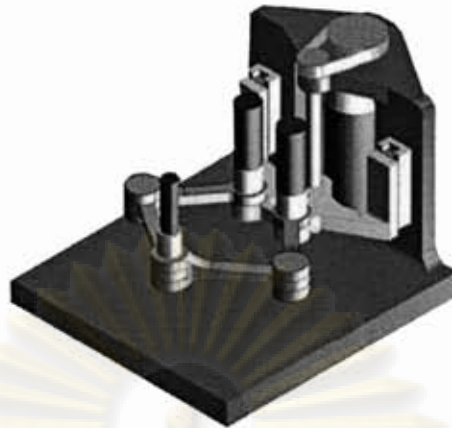
Figure 2.7: The Parallel Hybrid MICRO-SCARA Robot for High Precision Assembly [12]
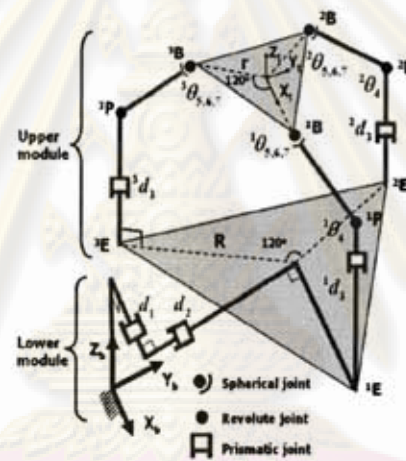
Figure 2.8: The 5-DOF Hybrid Micro-Manipulator for Medical Applications [13]
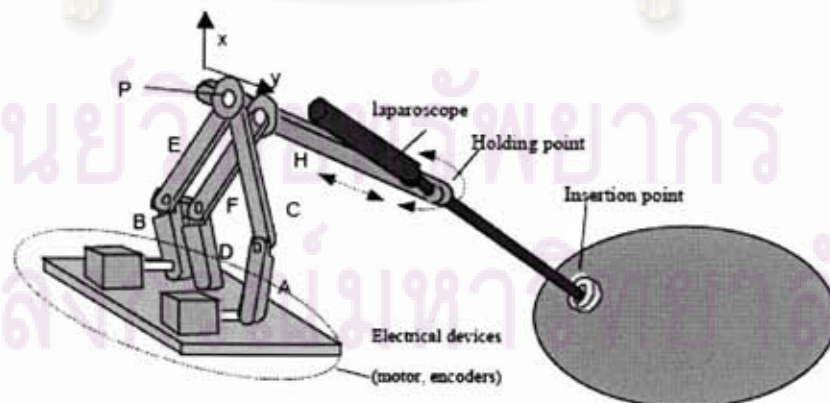
Figure 2.9: A New Laparoscope Manipulator with an Optical Zoom [14]

2.3 Power transmission for high precision design

Backlash is a clearance between mating components, sometimes described as the amount of lost motion due to slackness or clearance when movement is reversed and contact is re-established (see Figure 2.10). For example, in a pair of gears, backlash is the amount of clearance between mated gear teeth. This gap means that when a gear-train is reversed the driving gear must be turned a short distance before all the driven gears start to rotate. Moreover, backlash results in inaccurate calculation from the small errors introduced at each change of direction.

Nevertheless, the backlash leads to a nonlinear phenomenon and other complicated errors. Then, the backlash-components should be avoided or carefully limited in the high precision system. However, backlashes can not be eliminated perfectly. Many techniques and devices have been created to lessen this clearance as much as possible, for instance harmonic drives, zero-backlash gears, and belt-and-pulley systems. The details are described as follows.
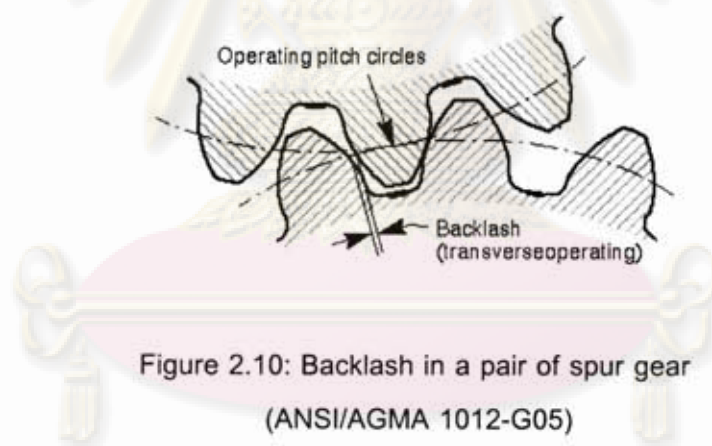
Figure 2.10: Backlash in a pair of spur gear
(ANSI/AGMA 1012-G05)

2.3.1 Harmonic gear

Many characteristics of harmonic gears suit robot specifications. The harmonic gears provide zero-backlash, high torque, excellent positional accuracy, and very high reduction ratio. Moreover, the harmonic gears are compact is compact and cannot be back driven. The mechanism consists of three components which are a wave generator, a flexcpline, and a circular spline (see Figure 2.11). The reduction ratio is depended on the number of the teeth in each gear and can be calculated from Equation (2.3.1)

$$\frac{\omega_{in}}{\omega_{out}} = \frac{N_o}{N_c - N_f} \tag{2.3.1}$$

Where

N_o = the number of teeth on output member of flexspline or circular spline

N_c = the number of teeth on circular spline

N_f = the number of teeth on flexspline
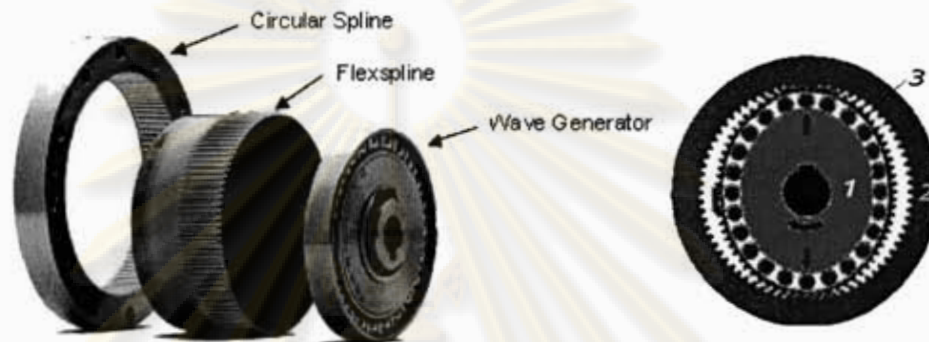
Figure 2.11: Three main components of harmonics drive [16]

In general, the reduction ratio of harmonic gears is significantly high. For example, the harmonic gears with N_f = 200 and $N_c = N_o$ = 202 have reduction ratio = 100:1. The high reduction ratio not only provides high torque and prevents back-driving but also decreases effects of non-linearity. Thereby, the manipulator can be controlled easier and more precisely. However, the harmonic gears have some disadvantages which are high friction and the not smooth motion.

2.3.2 Zero backlash gear

Several methods are used on the conventional gear system to eliminate the gear backlash, such as antibacklash gears, adjustable gear centers, and gear preload. The details are described below.

2.3.2.1 Antibacklash gears

Each of these gears is a spring-loaded gear pair suitable for light-duty control gear trains (see Figure 2.12.). These gears eliminate all backlashes and allow liberal tolerance for gear manufacture and gear assembly.
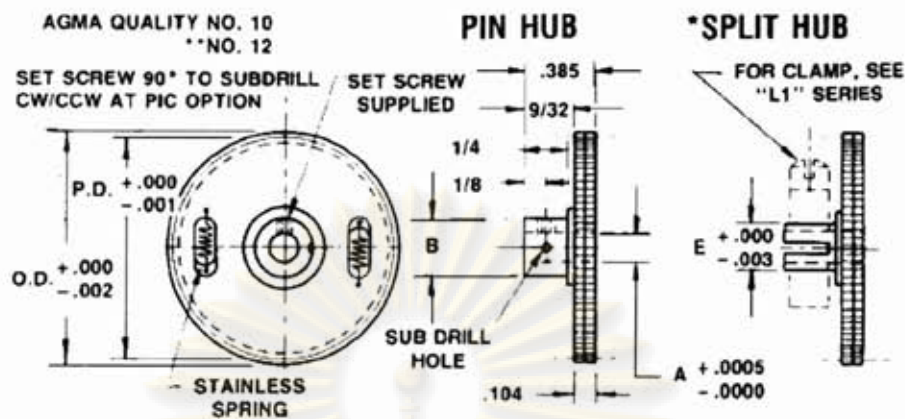
Figure 2.12: Antibacklash gear

2.3.2.2 Adjustable gear centers

This technique provides for no backlash only at the condition of tightest mesh. These gear trains can be used to transmit substantial torques. Because of the skill required for adjusting the gear centers, assembly and field replacement are difficult. The adjustable gear centers are shown in Figure 2.13.
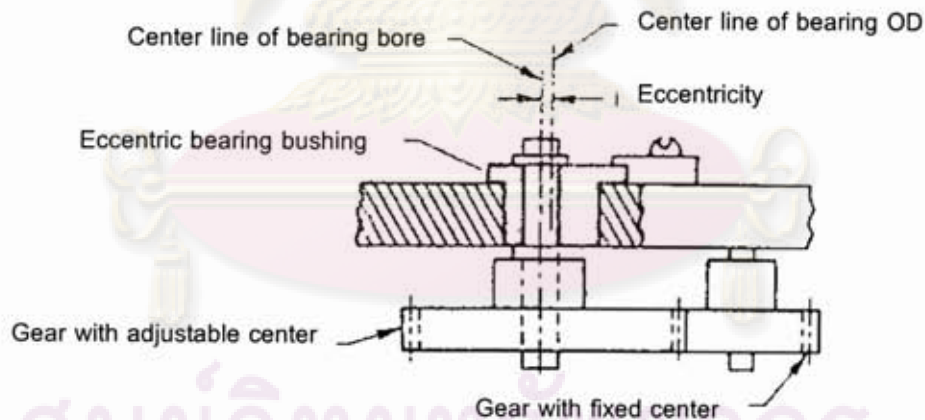
Figure 2.13: Adjustable gear centers

2.3.2.3 Gear preloads using an auxiliary motor

This technique uses an auxiliary torque motor to preload a gear train so that gears tend to favor one side of the gear tooth. If the loading on the gear train can be designed to always have one directional sense, then backlash will not be problem.
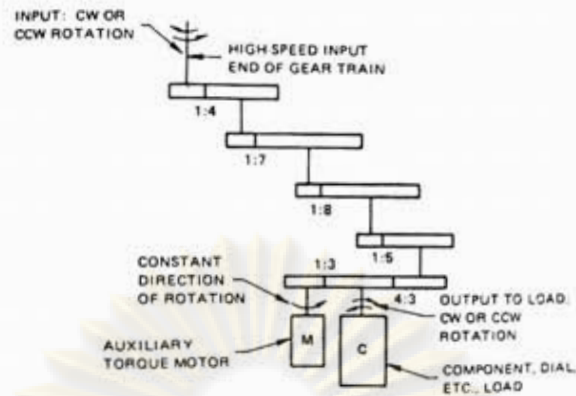
Figure 2.14: Gear preload using an auxiliary motor

2.3.2.4 Gear preloads using a dual-pass gear train

Dual-pass gear trains are installed pass the pinion (Figure 2.15). Due to the preload result in a slight reduction in overall efficiency and load capability, this technique suits low torque and high precision applications.
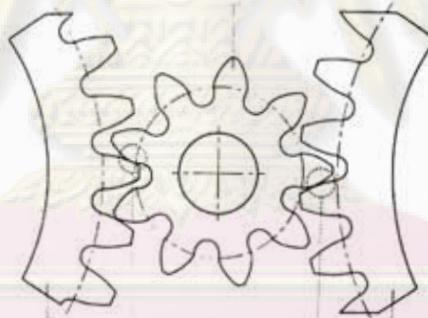
Figure 2.15: The gear preload using dual-pass gear train

(Picture from miniature drive systems catalogs, FAULHABER Group) [18]

2.3.3 Tendon-driven

Tendon-driven is a transmission system that typically used in light weight and high speed manipulators. "Tendon" is usually implied a belt or cable. Many outstanding benefits of tendon-driven are presented in mechanism of robot. First, all actuators can be located at the fix base so that the manipulator can be designed more compact and low inertia. Second, backlash is eliminated if extension tendon is prevented. The extension can be prevented by using appropriate material and tensioners. On the other hand, the serious problems are friction and undesirable vibration.

In brief, a tendon-driven can be categorized into two types which are a closed-loop tendon drive and an open-ended tendon drive.

2.3.3.1 Closed-loop tendon drives

The majority of tendon-drive used in common machines is the closed-loop type. Only one motor is needed for driving the tendon in both directions. Consequently, the number of actuators equals to DOF of the manipulator. Performance of this power transmission relies on the friction between pulleys and tendon. Hence pretension is necessary to enhance the efficiency. The closed-loop tendon drives can be connected in various arrangements. The examples are shown in Figure 2.16 and 2.17.
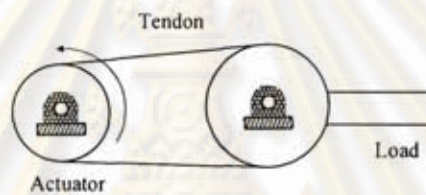
Figure 2.16: Closed-loop tendon drives (Single-stage)
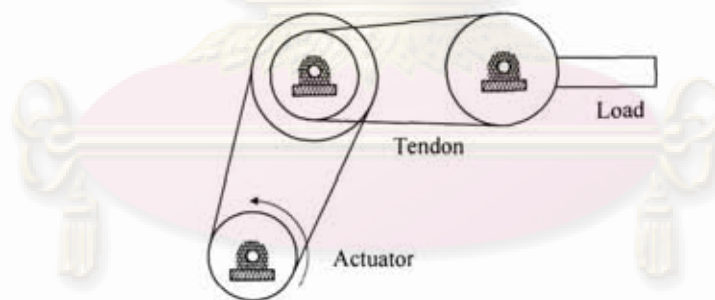
Figure 2.17: Closed-loop tendon drives (Double-stage)

2.3.3.2 Open-ended tendon drives

Performance of this type is depended on the force exertion to a moving link. One end of the tendon is attached to the moving link while another end is pulled by an actuator. Force is transmitted by pulling of the tendon. Because the tendon can exert only tension forces, the actuator must applies force in a unidirectional sense. Consequently, the number of actuators must be more than DOF of the manipulator. The

manipulator driven by this open-ended type is usually described with $n \times m$ (where n is the DOF and m is the number of control tendons). For example, a 2×3 tendon driven manipulator has 2 joints and 3 cables (see Figure 2.18).
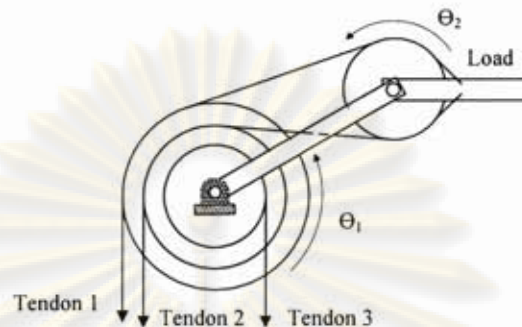
Figure 2.18: Open-ended tendon drives

2.4 Manipulator wrist

In practice, manipulators need at least 6 DOF to archive dexterous movement. The arm (the first 3-DOF) moves the wrist center in the primary workspace while the wrist (the last 3-DOF) controls the orientation of the end-effector. The wrist with 3-DOF can provide sufficient dexterity for basic industrial tasks, such as welding, spraying, part assembly etc.

2.4.1 Wrist design

The characteristics of a good manipulator wrist are

- At least 3 DOF
- Spherical wrist mechanism
- Large workspace and large angular orientation
- Compact size, light weight, and low inertia
- Remote drive capability
- High accuracy and repeatability
- High mechanical stiffness
- Reliable design
- Low manufacturing cost

In practice, the last three axes intentionally designed as a spherical wrist. These axes have to intersect at the common points, called "a wrist center" (see Figure 2.19). This configuration leads to a completely decoupling between position and orientation. Hence the closed-form solution of kinematics equation exists. In case of non-spherical wrist, the kinematics solution would be very complicated.
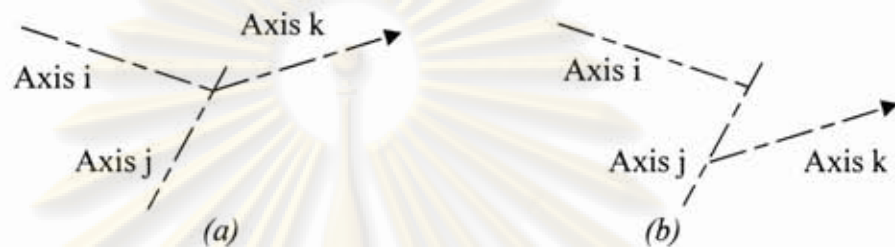
Figure 2.19: A spherical wrist (a) and non-spherical wrist (b)

As regard to the location of actuators, the actuators cannot be placed on each link directly because of too heavy weight and high inertia. The concept of an epicyclic gear train is generally applied in order to separate the actuators from the wrist. The actuators will completely control the links but some links are coupled. Therefore, additional computation is needed to control the wrist precisely.

A variety of the epicyclic gear train configurations are applied to the wrist; for example Cincinnati-Milacron (Stackhouse, 1979) [19] (see Figure 2.20) and Bendix Corporation (Anonymous, 1982) [19] (see Figure 2.21)
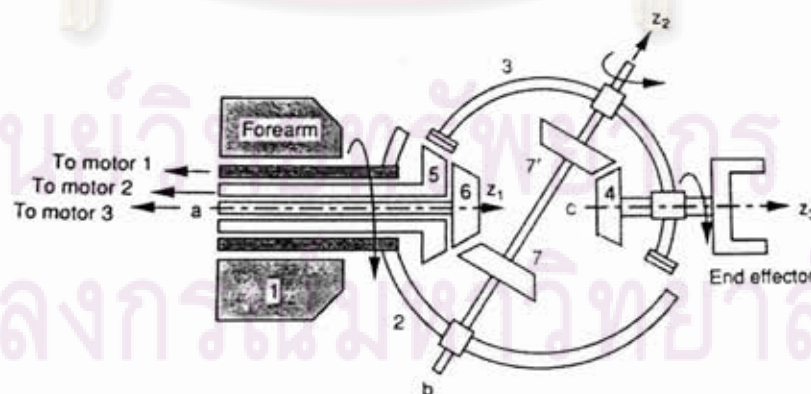
Figure 2.20: Epicyclic gear train developed by Cincinnati-Milacron consists of 7 links, 6 turning pair and 3 bevel gears [19]
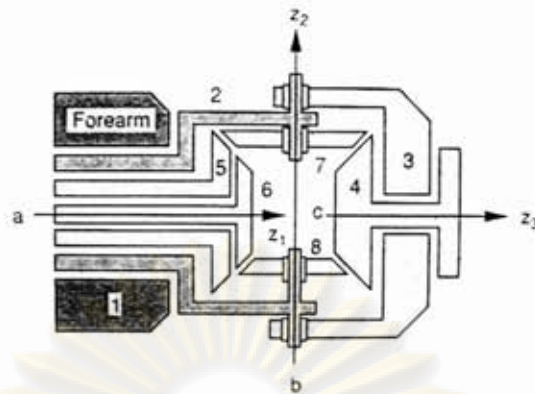
Figure 2.21: Epicyclic gear train developed by Bendix Corporation
consists of 8 links, 7 turning pair and 4 bevel gears [19]

2.4.2 Wrist type

Robot wrist is typically categorized into two types according to the orientation of axes: "a pitch-yaw-roll wrist" and "a roll-pitch-roll wrist". They are described as follows.

2.4.2.1 The pitch-yaw-roll wrists

The pitch-yaw-roll wrist is developed and designed based on the basic human wrist movement. The pitch and yaw movement equivalent to the radial/ulnar and flexion/extension deviation respectively. In general, the pitch-yaw-roll wrist has greater dexterity than the roll-pitch-roll wrists because of singularity–free and less workspace limitations. However, the pitch-yaw-roll wrists are not popular among the industrial robots according to the very complex mechanism. This complication leads to many problems with overall precision and high maintenance cost.
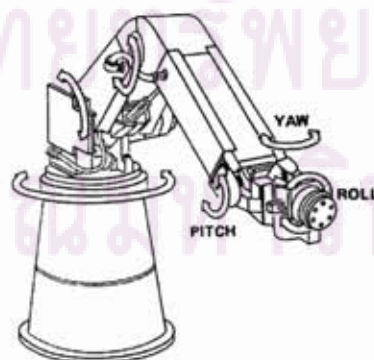
Figure 2.22: The pitch-yaw-roll wrist attached to a manipulator [20]

2.4.2.2 The Roll-pitch-roll wrist

The roll-pitch-yaw wrists are popular among robotics and teleoperation system due to its relatively simple design. However, the singularity formed when two axes are aligned is a major problem. The movement is smooth and uncontrollable when the singularity has been occurred. Hence, a critical workspace around the singularity area has to be avoided in order to maintain dexterity. However, this problem can be solved by programming.
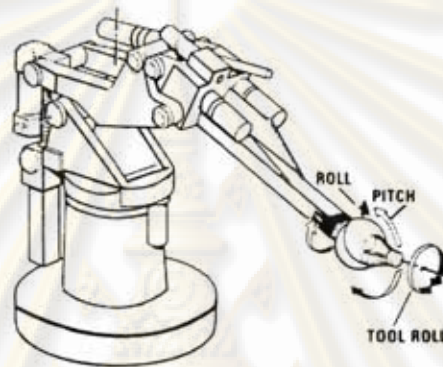
Figure 2.23: The roll-pitch-roll wrist attached to a manipulator [20]

2.5 Manipulator stiffness

Sufficient stiffness is necessary in order to maintain precision of manipulators. High stiffness prevents link from deformation and too much flexibility. Position and orientation error at the end-effector will be occurred if links are deflected and deformed. Moreover, resonance in structures can be occurred due to flexibility [21]. This unpredictable phenomenon decreases performance of the system.

The stiffness of connected elements depends on the methods of connection: series or parallel. It is computed from Equation (2.5.1) and (2.5.2) respectively.

$$\frac{1}{k_{series}} = \frac{1}{k_1} + \frac{1}{k_2} + \frac{1}{k_3} + ... + \frac{1}{k_i} \tag{2.5.1}$$

$$k_{parallel} = k_1 + k_2 + k_3 + ... + k_i \tag{2.5.2}$$

Where k = stiffness

2.6 Kinematics structure and manipulator resolution

Kinematics structure obviously affects the overall resolution of the manipulator. The length of each links and resolution of sensors significantly dominate the resolution and error of manipulators. In practice, the servo actuator cannot move smaller than 1 pulse of the encoder. Hence the resolution of the manipulators is computed from this value. From Figure 2.24, $\Delta\theta$ represents the smallest angle that the motor can move according to a single encoder pulse. Thereby, the actual position ($P^{\bullet}$) is deviated little from the desired position (P). The position error of the end of the link - the gap between both points - can be roughly computed from Equation (2.6.1)
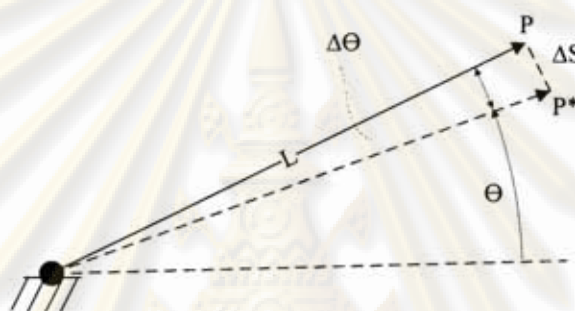
Figure 2.24: Resolution and position error of a link

Where

L = length of the link

P = desired end point

$P^{\bullet}$ = actual end point

$\Delta\theta$ = the smallest angle that can be move

ΔS = error occurred at the end of the link

$$\Delta S = L(\Delta\theta) = L\left(\frac{2\pi}{ppr}\right)$$ (2.6.1)

Where ppr = pulse per revolution

Please note that the reduction ratio of transmission system which is connected directly to the encoder have to be considered.

2.7 Orientations

An orientation of the end-effector can be described by many methods. The X-Y-Z fixed angle is one of the common conventions. The frame rotates about the fixed axes with the angles roll-pitch-yaw respectively.

In general, the rotational matrix $_B^A\mathbf{R}_{XYZ}(\gamma,\beta,\alpha)$ represents the rotation of frame {B} that firstly coincident with frame {A}. This frame is rotated about $\hat{X}_A$ by γ, $\hat{Y}_A$ by β, and $\hat{Z}_A$ by α. Subsequently, the $_B^A\mathbf{R}_{XYZ}(\gamma,\beta,\alpha)$ can be derived straightforward by the following equations.

$$_B^A\mathbf{R}_{XYZ}(\gamma,\beta,\alpha) = \mathbf{R}_z(\alpha)\mathbf{R}_Y(\beta)\mathbf{R}_X(\gamma) \tag{2.7.1}$$

$$_B^A\mathbf{R}_{XYZ}(\gamma,\beta,\alpha) = \begin{bmatrix} c\alpha c\beta & c\alpha s\beta s\gamma - s\alpha c\gamma & c\alpha s\beta c\gamma + s\alpha s\gamma \\ s\alpha c\beta & s\alpha s\beta s\gamma + c\alpha c\gamma & s\alpha s\beta c\gamma - c\alpha s\gamma \\ -s\beta & c\beta s\gamma & c\beta c\gamma \end{bmatrix} \tag{2.7.2}$$

Where

α = roll angle

β = pitch angle

γ = yaw angle
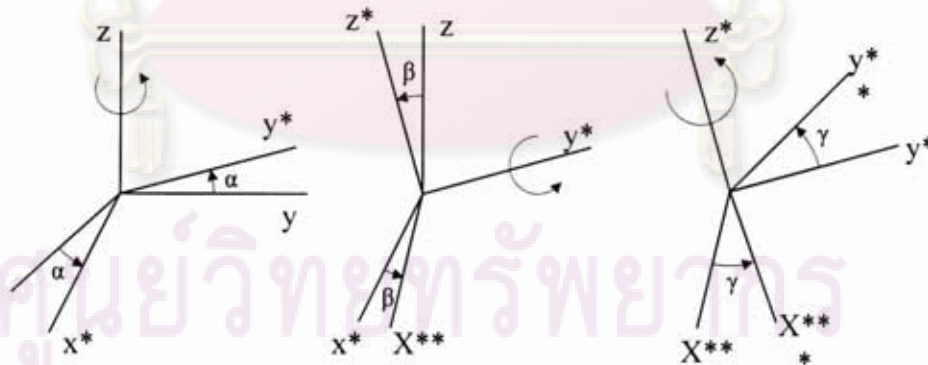
Figure 2.25: Description of the Euler rotation about Z-Y-X axis

The inverse problems are usually found in many general applications. For example the master slave system, the master device provides the rotation matrix (or the transformation matrix) and the roll-pitch-yaw angles have to be solved. The solution is derived from Equation (2.7.2). Hence the solutions are:

$$
{}^{A}_{B}\mathbf{R}_{XYZ}\left(\gamma,\beta,\alpha\right)=\begin{bmatrix} r_{11} & r_{12} & r_{13} \\ r_{21} & r_{22} & r_{23} \\ r_{31} & r_{32} & r_{33} \end{bmatrix} \tag{2.7.3}
$$

$$
\beta = A\tan 2\left(-r_{31},\sqrt{r_{11}^{2}+r_{21}^{2}}\right) \tag{2.7.4}
$$

$$
\alpha = A\tan 2\left(\frac{r_{21}}{\cos(\beta)},\frac{r_{11}}{\cos(\beta)}\right) \tag{2.7.5}
$$

$$
\gamma = A\tan 2\left(\frac{r_{32}}{\cos(\beta)},\frac{r_{33}}{\cos(\beta)}\right) \tag{2.7.6}
$$

CHAPTER III

DESIGN OF THE 6-DOF SLAVE MANIPULATOR FOR MINIATURE TASKS

The topics related to mechanism of the 6-DOF slave manipulator are explained in this chapter. The mechanical design specifications, constraints and prototypes of this manipulator are clearly explained. Nevertheless, selection of components and manufacturing process are described in detail. The 6-DOF manipulator for miniature task is hereinafter called "RCRT-1 Manipulator".

3.1 Desired characteristics

The main purpose of the RCRT-1 Manipulator is to work with common and sophisticated small tasks. It will be used as the slave manipulator in a master-slave system. Moreover, the objective of this manipulator is subject to more specific application such as the surgical assisted robotic systems (e.g. MIS). Consequently, ability to work in limited space and association with the master device must be considered. The desired characteristics of the RCRT-1 Manipulator are listed as follows.

- High accuracy
- High precision
- High resolution (better 0.1 mm)
- High stiffness
- Low inertia
- Large workspace
- Dexterous movement
- Able to work in limited space
- Well associated with the movement of master device.
- Carry extra light weight loads and low speed movement.
- Ease of maintenance and assembly.

The methods that make this manipulator meets these requirements are described in the following topics.

3.1.1 High resolution

Kinematics structures and sensor resolution must be focused intensively in order to obtain high resolution. The link should not be too long and resolution of the sensors should be high. The minimum length of the links is roughly constraint by other requirements, including the desired workspace and mechanism configurations etc. Hence, sensors that have sufficient resolution should be chosen. However, the high reduction ratio power transmission components (e.g. harmonic drive gears and ball screws) can increase the resolution.

The overall resolution can be roughly computed in as in Topic 2.6. The resolution at the end-effector is obtained form the resolution of joint given.

3.1.2 High precision

Precision and repeatability are based on amount of uncertainties in mechanism and control system. These uncertainties in mechanism comprise gear backlash, flexibility of coupling, loosen of components, gap in bearings, and frictions etc. These uncertainties can be eliminated by using appropriate components, for instance zero-backlash gears, harmonic drive gears, and standard bearings.

As regard to the control system, errors are occurred from inappropriate control scheme and parameters. Because some external uncertainties (e.g. friction and external loads) cannot be indicated exactly, the mathematics model of the manipulator is not accurate (detail in Chapter V).

3.1.3 High accuracy

The kinematics parameters must be accurate in order to obtain high accuracy. The parameters in the mathematics model should be equal to the parameters in the actual manipulator. In practice, the differences between the model and the actual system are always occurred. The accurate parameters cannot be specified exactly without calibration.

However, calibration process is not in the scope of this research. In order to minimize these undesirable differences, errors in dimension of parts must be limited. In general, CNC machining provides $\pm 5\ \mu m$ to $\pm 20\ \mu m$ tolerance and rapid-prototyping provides approximately $\pm 100\ \mu m$ tolerance. Moreover, the errors are occurred from

other factors, e.g. assembly, part deformation, axes misalignment, and home position return.

.

In conclusion, from Topics 3.1.1 - 3.1.3, specifications of the mechanical parts govern the overall resolution, precision, and accuracy of the manipulator. In brief, the roughly design policies are concluded in the list below.

- Use short links.
- Use high resolution sensors with high reduction ratio transmission components.
- Use zero backlash gears.
- Use flexible couplings.
- Use good quality standard components (e.g. bearing and coupling).
- Use exact kinematics parameters (appropriate manufacturing process).
- *Use PID-controller.
- *Use feed forward compensation (e.g. gravity and friction).
- *Use inverse dynamics control (e.g. robust control).
- *Calibration (not in the scope of this research).

Topics related to control system and programming, see Chapter VI.

3.1.4 High stiffness

High stiffness eliminates errors from deformation and deflection of each link. The overall stiffness typically depends on type of mechanical components, dimension, connection between elements, and material (see Topic 2.5). Moreover, parallel manipulators have higher stiffness than serial manipulators.

3.1.5 Low inertia

High inertia leads to complicated control problems, especially when manipulators perform high speed movement. Thereby, low inertia is preferred. The overall inertia relates to the weight, shape, and configuration of each link. One of the most effective solutions is to reduce the weight by placing actuators on the base.

However, because the RTRC-1 Manipulator was operated in low speed movement and handles light loads, the effect of inertia is insignificant.

3.1.6 Large workspace

The workspace must be large enough in order to support various purposes. Apparently, a serial mechanism was chosen.

3.17 Dexterous movement

The dexterous movement relies on the configuration and DOF of the wrist. In brief, the 3-DOF roll-pitch-roll wrist was preferred. The mechanism of roll-pitch-roll wrist can be simplified and the computation is not complicated. However, the major problem of singularities is presented.

3.1.8 Working in limited space

The wrist and arm have to be small enough in order to penetrate through incisions and work in a limited space. Moreover, the lower arm should be long and narrow.

3.1.9 Association with the master device

The Phantom® Omni™ Haptic Device [22] (see Chapter VI) was used as the master device. Even though the mechanical configuration of the slave manipulator and the master device are totally different, they can be connected together by the transformation matrix. The transformation matrix provides sufficient data to describe positions and orientations of the end-effector. According to master-slave operation, users observe movement of the slave manipulator while control the master device. For users' convenience, the orientation of the end-effector of both robots must be similar. Eventually, the roll-pitch-roll wrist was selected.

3.1.10 Conclusion of design plan

<u>3.1.10.1 Using serial or hybrid mechanism</u>

The parallel mechanism is not appropriate because of many disadvantages, including small workspace, very complicate structure, and complex kinematics. Moreover, benefits of the closed-loop structure (e.g. high stiffness and low inertia) are not necessary for performing miniature tasks.

On the other hand, a serial and a hybrid mechanism have large workspace, simple structures, and simple kinematics calculations. Even though low stiffness and high inertia are the major problems, they can be improved by the following techniques:

- Place most of actuators near the base of the manipulator.
- Choose configuration that compensate inertia (4-bars mechanism).
- Use high reduction ratio gears to reduce effects from inertia.
- Use light weight material.

<u>3.1.10.2 Providing high dexterity and effective work</u>

- A narrow and long lower arm (appropriate for working in limited space)
- A 6-DOF slave manipulator
- A 3-DOF wrist, the same type as the Phantom's wrist (roll-pitch-roll)

<u>3.1.10.3 Components selection and design constraints</u>

- Use short link.
- Use high resolution sensors with high reduction ratio transmission components.
- Use zero backlash gears.
- Use flexible couplings.
- Use good quality standard components (e.g. bearing and coupling).

3.2 Prototype design

3.2.1 Prototype No.1

This manipulator prototype is a novel structure designed in hybrid serial-parallel mechanism. The lower arm is very narrow and long. The desired working area is in front of the manipulator and below the base plane. The 1st and the 2nd actuators drive the four-bar linkage horizontally. Both of them control the horizontal position of the end-effector. At the same time, the 3rd and the 4th actuators drive the four-bar linkage vertically. Both of them control the vertical position. A four-bar linkage mechanism is shown in Figure 3.1. The 5th and the 6th actuators are located on the top of the lower arm. As regard to the orientation of the end-effector, it is controlled by all six actuators.

This mechanism provides high stiffness and low inertia according to the closed-loop structure. Furthermore, the lower arm is very small narrow due to tendon drives (see Figure 3.1). However, the major problems are about workspace and dexterity. The movement of the end-effector is limited due to the mechanical configuration. Nevertheless, a number passive joints lead to a lot of errors.

The CAD model and workspace of this prototype are shown in Figure 3.3. The advantages and disadvantages are concluded below.

3.2.1.1 Advantages

- A novel design
- High stiffness
- Low inertia
- An extra narrow lower arm design
- Effectively working in limited spaces

3.2.1.2 Disadvantages

- Somewhat complex structure and kinematics
- Lots of error due to the structure complexity
- Mechanical singularity (from five-bar linkages)
- Difficulty in assembly

- Difficulty in maintenance
- Small workspace
- Lack of dexterity
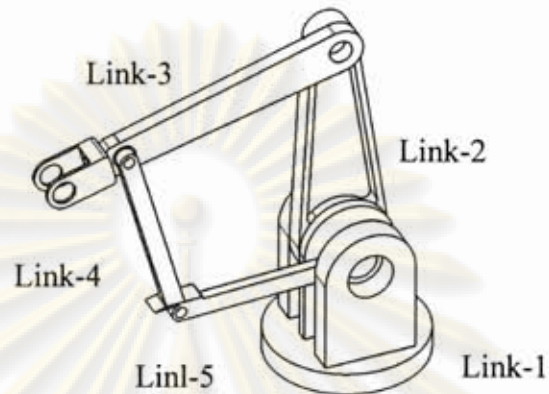
Figure 3.1: A four- bar linkage mechanism
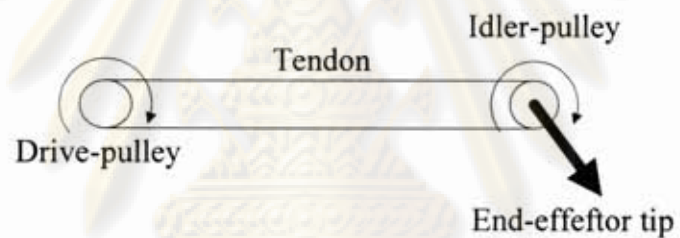
Figure 3.2: A simple arrangement of tendon driven mechanism
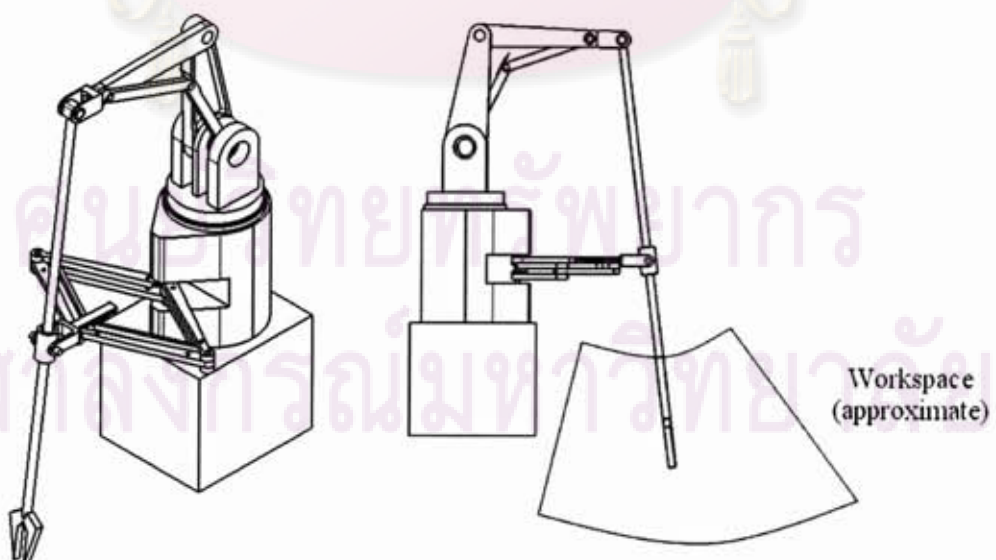
Figure 3.3: A CAD model of the Prototype No.1 with its workspace

3.2.2 Prototype No.2 (RCRT-1 Manipulator)

<u>3.2.2.1 Structure configuration of arm (1st- 3rd axis)</u>

This prototype is designed based on the serial mechanism due to the benefit of large workspace. In contrast, inertia and stiffness are minor concern due to low speed movement operation and light load carrying. As regard to the type of serial manipulator (see Table 3.1) [21], the spherical manipulator was selected due to the benefits of dexterity and object approach. The prismatic joint in the lower arm of the spherical manipulator allows effectively penetration approach. Moreover, the end-effector should be able to approach the object in any direction.

<u>3.2.2.2 Transmission of the 2nd joint (revolute joint)</u>

In practice, the offset between the 1st and the 2nd axis is presented in most of the industrial manipulators e.g. Stanford Arm [17]. This offset should be eliminated because it leads to complicated kinematics calculation. Moreover, the movement of the 3rd link of the slave manipulator is not properly associated with the master device. Hence, the mechanism of the 2nd joint has to be modified. Appropriate power transmission system can be applied in order to move the actuator to more suitable location. Tendon drives, gear trains, and four-bar linkage mechanism were concerned as the candidates. Specifications of the candidate are shown in Table 3.2.

Table 3.1: Specifications of the five general type of serial manipulator

Type	Configuration	Space required	Speed	Load carrying	Appropriate approach	Penetration
Cartesian	P-P-P			✓✓		✓
Articulated	R-R-R	✓			✓	
SCARA	R-R-P	✓	✓	✓		✓
Spherical	R-R-P	✓			✓	✓
Cylindrical	R-P-P	✓		✓		✓

✓ represents the advantage and ✓✓ represents the outstanding advantage

R represents revolute joint and P represents a prismatic joint

Table 3.2: Specifications of the transmissions for the 2nd joint

Type	Stiffness	Backlash	Friction & Inertia	Complicated in assembly and maintenance	Error due to assembly	Power-to-weight ratio	Durability	Compact structure
Cable – pulley		✓	✓	✓		✓		✓
Timing belt -sprocket	✓		✓	✓	✓	✓		✓
Anti backlash gear	✓✓	✓					✓	✓
four-bar linkages	✓✓	✓✓	✓				✓✓	

✓ represents the advantage and ✓✓ represents the outstanding advantage

From the qualifications in Table 3.2, obviously, the most appropriate transmission is the four-bar linkage mechanism. The advantage of very high stiffness allows this joint to deal with the weight of the 3rd to the 6th links effectively. Thereby, very little error might be occurred. Moreover, little backlash and low friction benefit to more precisely dynamic control because the nonlinearities are decreased. Furthermore, the links are more rigid and durable than the tendons or gears.

On the other hand, the undesirable offset at the base, due to the assembly process, may lead to some error at the end of linkages. One of the cases that error is occurred is illustrated in Figure 3.4 as an example. However, this offset can be adjusted and compensated by the calibration process. Finally, the complete structure of the four-bar linkage in of the prototype No.2 is illustrated in Figure 3.5.
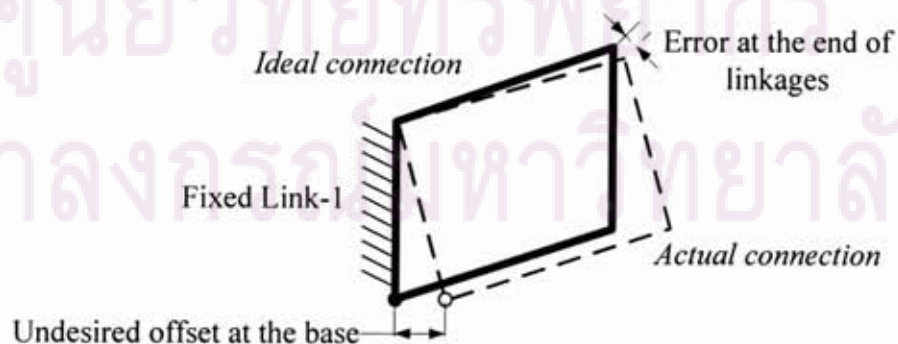
Figure 3.4: An example case of the error of the four-bar linkage
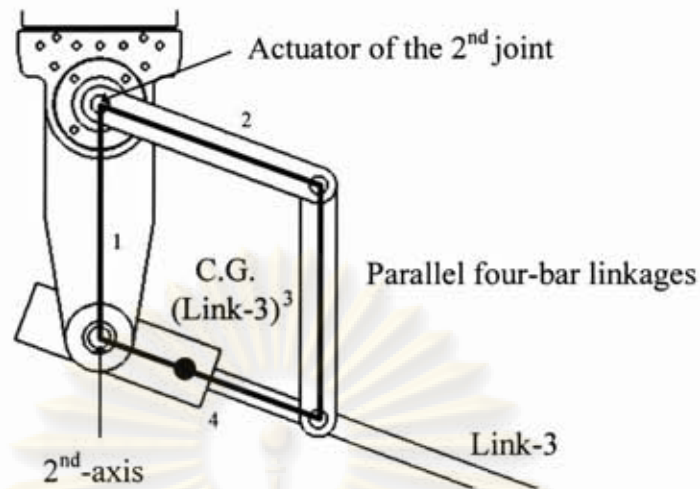
Figure 3.5: Structure of the four-bar linkage of the prototype No.2

3.2.2.3 Transmission of the 3rd joint (prismatic joint)

Many kinds of actuator can be used to drive the prismatic joint. Even though a linear motor can drive the joint directly, the major problems are the price and insufficient resolution. Therefore, a rotary motor mounted on the rotary-to-linear motion power transmission must be concerned. Ball-screws, tendon drives, and rack-pinions were concerned as the candidates. In summary, specifications of the candidate are clearly shown in Table 3.3.

In conclusion, from the specifications in Table 3.3, the most appropriate transmission is the ball-screw. High resolution and little backlash significantly increase precision manipulator. The high stiffness benefits to loads handling capability and accuracy. Moreover, due to the considerably high reduction ratio, motor can be suspended steadily without requirement of an exert torque. Nevertheless, nonlinearities are diminished.

Table 3.3: Specifications of the transmissions for the 3rd joint

	Resolution	Stiffness	Backlash	Friction & Inertia	Compact structure	Power transmission	Linear speed (relative to motor rotation speed)	Weight	Durability	Level suspension
Linear motor	✓	✓	✓✓	✓		✓				✓
Ball-screw	✓✓	✓✓	✓		✓✓	✓✓			✓	✓✓
Tendon drive			✓	✓	✓		✓	✓		
Rack-pinion		✓			✓	✓	✓		✓	

✓ represents the advantage and ✓✓ represents the outstanding advantage

3.2.2.2 Wrist design

The roll-pitch-roll configuration was used for the wrist mechanism due to two major advantages: proper association with the wrist of the Phantom and a simple mechanical design. As regard to the desired ability of working in limited space, the wrist must be small and compact enough. Therefore, the actuators which drive the 4th to the 6th joint must be located on the base of the 3rd link. This base is far away hence a proper transmission mechanism must be considered

Epicyclic gear trains are commonly used in the industrial robot in order to minimize the wrist size. Consequently, this concept was applied to this manipulator. However, the original epicyclic gear trains are too large and too heavy with respect to the size of this manipulator. Hence, three possible adapted mechanisms were designed and concerned as the candidates. However, in order to minimize complication of the mechanism, the common design strategies are listed as follows:

- The 4th link will be driven by motor directly.
- The 5th link may be driven through bevel gears pair or a tendon.
- The 6th link will be driven through a tendon.

The qualifications of the possible designs are conclude as follows.

3.2.2.2. All of the last 3 motors on the 3rd link & tendon drives (a)

- Very low inertia
- Compact wrist
- Cannot handling heavy loads due to low stiffness of the 5th joint
- Very complex structure
- Very difficult for assembly and maintenance
- Tendons can get damages easily
- A little backlash may be occurred by the tendon extension

3.2.2.2.2 The 5th & 6th motors on the 4th link & tendon drives (b)

- Moderate inertia
- Compact wrist
- Cannot handling heavy loads due to low stiffness of the 5th joint
- Moderately complex structure
- Easy for assembly and maintenance
- Tendons can get damages easily
- A little backlash may be occurred by the tendon extension

3.2.2.2.3 The 5th & 6th motors on the 4th link & bevel gear (c)

- High inertia
- High stiffness (especially the 5th joint)
- High durability (especially the 5th joint)
- Simple structure & Easy for assembly and maintenance
- Wrist is not compact
- Some backlash between bevel gear teeth (see Figure3.6)
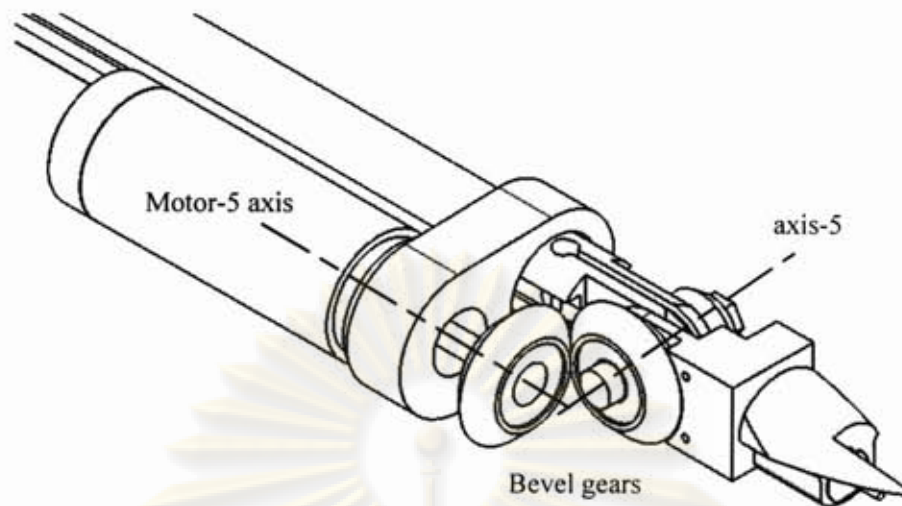
Figure 3.6: The 5th link driven by bevel gears (design c)

Table 3.4: Specifications of the wrist design

	Compact wrist	Backlash	Complex structure	Stiffness	Inertia	Durability
Design (a)	✓	✓			✓✓	
Design (b)	✓	✓	✓		✓	
Design (c)			✓✓	✓		✓

✓ represents the advantage and ✓✓ represents the outstanding advantage

The most complicated tendon arrangements are in the wrist box. Because the 5th axis is perpendicular to the 6th axis, some additional idler-pulleys are needed in order to achieve the tendon alignments. The first idler-pulley is located on the 5th link and the axis of this pulley and the 5th axis are concentric. However, this pulley can rotate freely and does not depend on the 5th axis. Subsequently, the tendon that controls the 6th axis passes through this pulley and goes around a pair of steel pins. This pair of steel pins, performing as the idler-pulleys, is also located on the 5th link. Two of them are parallel. Eventually, the tendon is passed through these pins and goes around the 6th axis. Therefore, the 6th axis can be driven. However, the coupling is occurred between the 5th and the 6th axis but can be corrected by programming. The arrangement of the tendon in the wrist box is clearly illustrated in Figure 3.7 to 3.9.
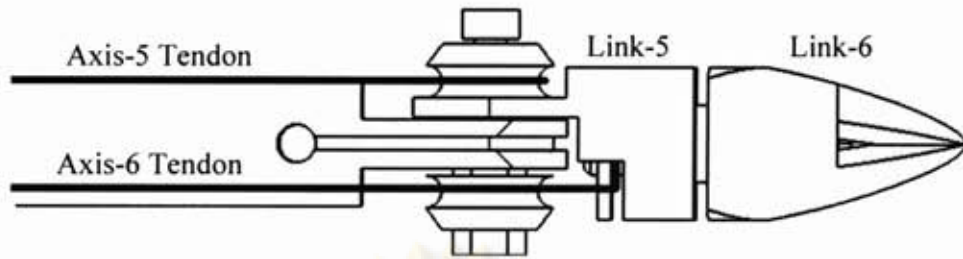
Figure 3.7: Tendon-pulley arrangements in the wrist box
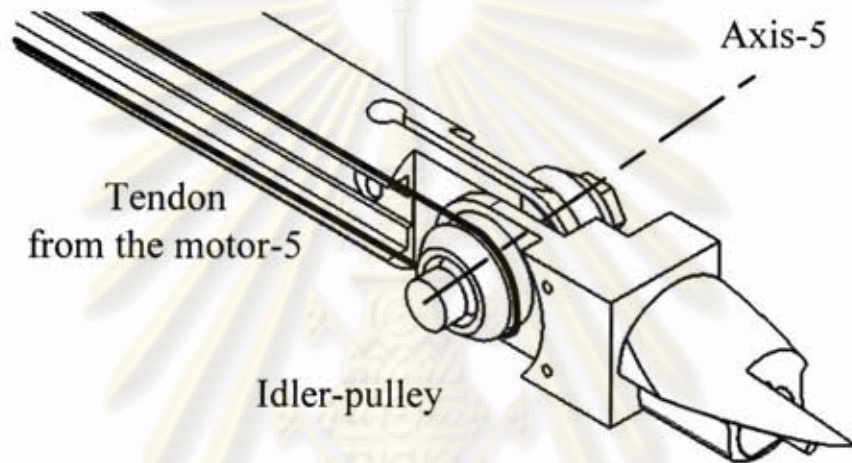
Figure 3.8: The 5th link driven by tendon
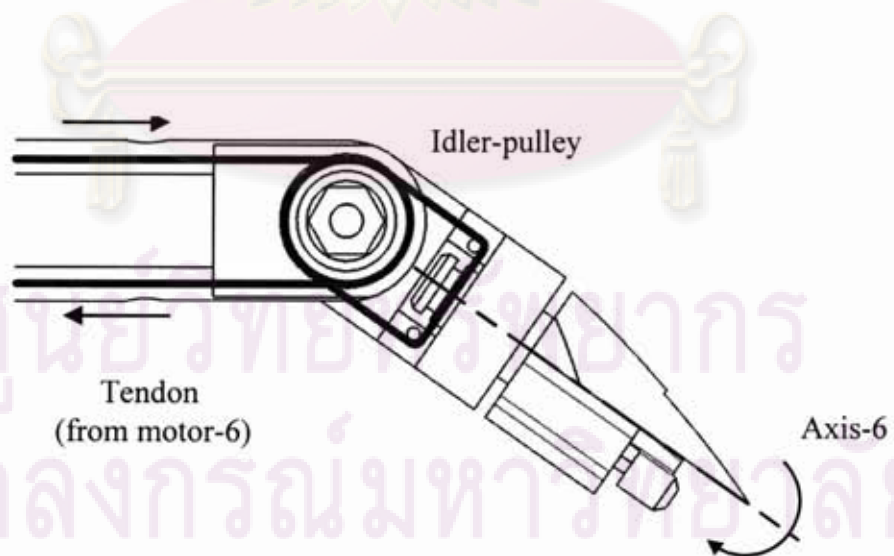
Figure 3.9: The 5th link driven by tendon

As regard to the design (a), even though this design is the most compact wrist, the major problem is too complicated structure. It leads to significant problems in assembly and kinematics computation. For the design (c), although the bevel gear can drive the 5th link very precisely, this additional gear is too large and makes the wrist too awkward. For the design (b), the tendon is able to control the 5th link precisely. Moreover, the wrist and the end-effector are very compact. In conclusion, the design (b) is the most appropriate.

In this research, 0.1 mm nylon strips have been used as the tendons. It is flexible and can be assembled to the wrist easily. On the other hand, the major problem is the extension that acts as the gear backlash. This leads to some error in joint angle. However, the tensioners are used in order to prevent the tendons from extension.

NOTE: Other material including 0.3 mm copper wires were attempted to use as the tendons. The major problem of the copper wire is unreliability. It was always deformed and broken down during the test.

3.2.2.3 Design conclusion

This prototype is designed based on the spherical serial manipulator. The typical benefits are large workspace and effective object approach. Moreover, a four-bar linkage mechanism is used as the power transmission for some axis.

One of the most useful features of the spherical manipulator is object approach. The long and narrow lower arm of this manipulator is able to penetrate to the limited working area. In brief, the typical configuration of this prototype is R-R-P-R-R-R, five revolute joints and one prismatic joint. The 1st and the 2nd axis influence an overall movement of the whole arm. Consequently, these first two actuators are mounted with harmonic drive gears in order to acquire the higher torques. Moreover, a four-bar linkage mechanism is adapted to the 2nd joint as the power transmission. Furthermore, the prismatic joint (the 3rd axis) is driven by a motor mounted with a ball-screw.

As regard to the wrist, it is designed based on a roll-pith-roll wrist structure. This wrist is located at the end of the long and narrow lower arm. Consequently, tendon-drive is used to transmit the power from the actuators on the 3rd link. Advantages and disadvantages are concluded in the following list.

3.2.2.3.1 Advantage

- Large workspace
- Moderate stiffness
- Moderate inertia
- A narrow lower arm design
- Effectively working in limited spaces
- Simple structure and kinematics
- Little error caused by assembly
- Ease of maintenance
- More dexterous
-

3.2.2.3.2 Disadvantage

- Some complex structure at the wrist
- Some backlash from tendon extension
- Mechanical singularity of four-bar linkages
- Computation singularity of and roll-pitch-roll wrist

A CAD model of this prototype is illustrated in Figure 3.10 and 3.11.

3.2.3 A Comparison between the prototype No.1 and No.2

As regard to Table 3.5, the prototype No.2 has more suitable qualifications than the prototype No.1 has. Therefore the second prototype has been selected. The details based on the prototype No.2 are explained in the next topic.
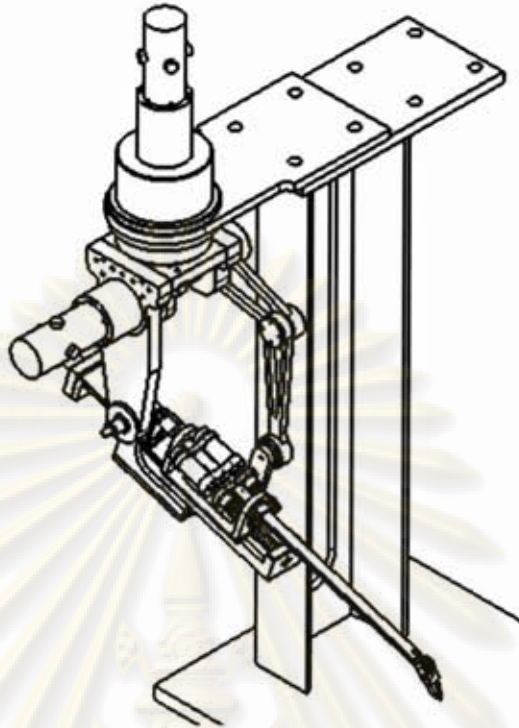
Figure 3.10: A CAD model of the Prototype No.2

Workspace
(approximate)
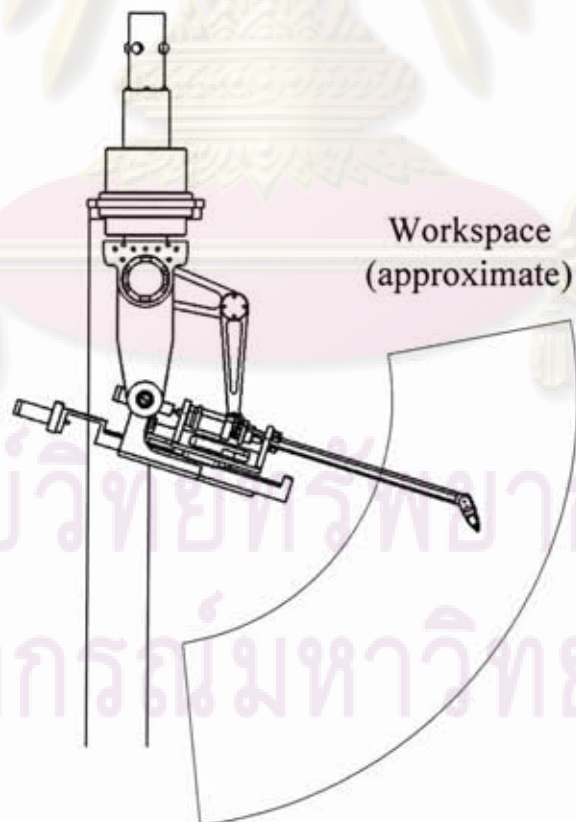
Figure 3.11: A workspace of the Prototype No.2

Table 3.5: A comparison between the prototype No.1 and No.2

	Prototype No.1	Prototype No.2
Accuracy, precision, resolution		✓
Stiffness	✓	
Inertia	✓	
Workspace and Dexterity		✓
Limited space working	✓	✓
Structure complexity		✓
Kinematics complexity		✓
Ease of maintenance and assembly		✓
The master device association		✓

3.3 Detail design

This topic describes the detail design of main parts of the prototype No.2 manipulator, hereinafter called "RCRT-1 Manipulator". The main parts comprise the arm and the wrist. Moreover, selections of standard components and parts manufacturing are clearly explained.

3.3.1 Components selection

3.3.1.1 Actuator

There are six actuators in this manipulator. The actuators are categorized into two sets according to their size – a high power motor and a low power motor. The high power motors are used in the 1st and the 2nd axis while the low power motors are used in the other axes.

3.3.1.2 Encoder

There are two types of encoder used in this manipulator, an incremental encoder and an absolute encoder. The incremental encoders are used for the motion feedback control while the absolute encoders are used for setting home positions.

Moreover, the encoders can be categorized by their sensing methods, consisted of an optical encoder and a magnetic encoder.

3.3.1.2.1 Incremental Encoder (quadrature encoder)

The medium resolution incremental encoders (500 - 1000 ppr) are used in the RCRT-1 Manipulator. In practice, gear boxes with high reduction-ratio are mounted on the front side of motors meanwhile the incremental encoders are on the rear side. This arrangement definitely increases resolution of each joint. Moreover, the signal from this encoder is interpreted by the clock multiplier in order to obtain 4 times higher resolution (X4).

Resolution of the revolute joint and the prismatic joint can be computed from Equation (3.1) and (3.2) respectively. For example, a 1,000 ppr incremental encoder mounted with an 87:1 harmonic drive gears and using (X4) clock multiplier has 1.034×10^{-3} degree angular resolution.

$$resolution_{axis} = \frac{360^\circ}{reduction\ ratio \times ppr \times 4} \tag{3.1}$$

$$resolution_{ball\text{-}screw} = \frac{pitch}{(reduction\ ratio)_{motor} \times ppr \times 4} \tag{3.2}$$

3.3.1.2.2 Absolute encoder

The 10-Bits (1024 ppr) absolute encoders are used in order to roughly set the home position. They are mounted on the front side of the motors. However, the resolution can not be increased by any methods.

3.3.1.3 Gear trains

The harmonic drives are applied to the first two motors while the zero backlash gears are applied with the others. The gears in the RCRT-1 Manipulator (except for the 3rd axis) are preferred having high reduction ratio, approximately 70:1 to 150:1. The higher torque can be produced and higher joint resolution can be obtained. However, there is a trade-off between torque and motor speed.

As regard to the 3rd axis, the high rotating speed is more important than the high torque in order to drive a ball-screw. Hence, the gear reduction ratio of the motor should be low.

3.3.1.4 Ball screw

The prismatic joint in the 3rd axis is driven through a ball-screw. A 1mm pitch ball- screw has been selected in order to obtain high resolution. Overall, resolution of this prismatic joint is 13.161 μm.

Table 3.6 shows the specifications of each axis. Typically, specification of motors, gear reduction ratios, and joint resolutions are presented.

Table 3.6: Joint specifications

Axis (motor)	Power (W)	Torque (N·m)	Speed (rpm)	Encoder (ppr)	Gear Reduction Ratio	Joint resolution (degree)
1(RH-14D)	18.50	5.9000	30.000	1000	90:1	1.0×10^{-3}
2(RH-14D)	18.50	5.9000	30.000	1000	90:1	1.0×10^{-3}
3(1624E012SR)	1.44	0.0056	3719.677	512	3.71:1	4.738×10^{-3}
(prismatic joint)					1 mm/pitch	13.161 μm
4(1524E012SR)	1.75	0.3525	70.213	512	141:1	1.247×10^{-3}
5(1524E012SR)	1.75	0.1900	130.263	512	76:1	2.313×10^{-3}
6(1524E012SR)	1.75	0.1900	130.263	512	76:1	2.313×10^{-3}

3.3.2 Part design

3.3.2.1 Arm

Since the first two axes are intersection and no-offset, only the length of the prismatic link is presented in the kinematics equation. Consequently, an overall resolution of the RCRT-1 Manipulator is significantly affected by this prismatic link.

Hence the proper length of the link must be concerned in order to obtain satisfied resolution. The resolution can be estimated as follows. Please note that the effect from the last three joints is insignificant and can be ignored.

This following procedure concerns the worst case of the overall resolution of this manipulator. First, let the 4th axis and the 6th axis superimposes (the 4th and the 6th link are inline). Subsequently, let the prismatic link move to its longest-reach position in order to provide the lower-bound of the overall resolution. Consequently, the poorest resolution can be computed from this prismatic link length and resolution of each encoder. The resolution of each axis can be computed from Equation (3.3). Nevertheless, the norm or overall resolution can be computed from Equation (3.4). .

Because the prismatic link is very long, the displacement caused by a change of a small joint angle (Figure 3.12) can be computed from the following equations. The resolution of the first two joints is computed from Equation (3.3). The resolution of the prismatic joint is equal to the resolution of a ball-screw; hence it is computed from Equation (3.2). Eventually, the overall resolution is computed from Equation (3.4).

$$resolution_{axis} = \left(\frac{2\pi}{reduction\ ratio \times ppr \times 4} \right) \cdot Length_{prismatic\ link} \qquad (3.3)$$

$$resolution_{overall\ manipulator} = \sqrt{\sum_{axis=1}^{3} \left(resolution_{axis}^{2} \right)} \qquad (3.4)$$

In this case, let the length of the prismatic link (including the length of tip) is 460 mm. Other information is from Table 3.6, the lower bound of overall resolution of this manipulator is approximately 11.355 μm (see Appendix A.4)
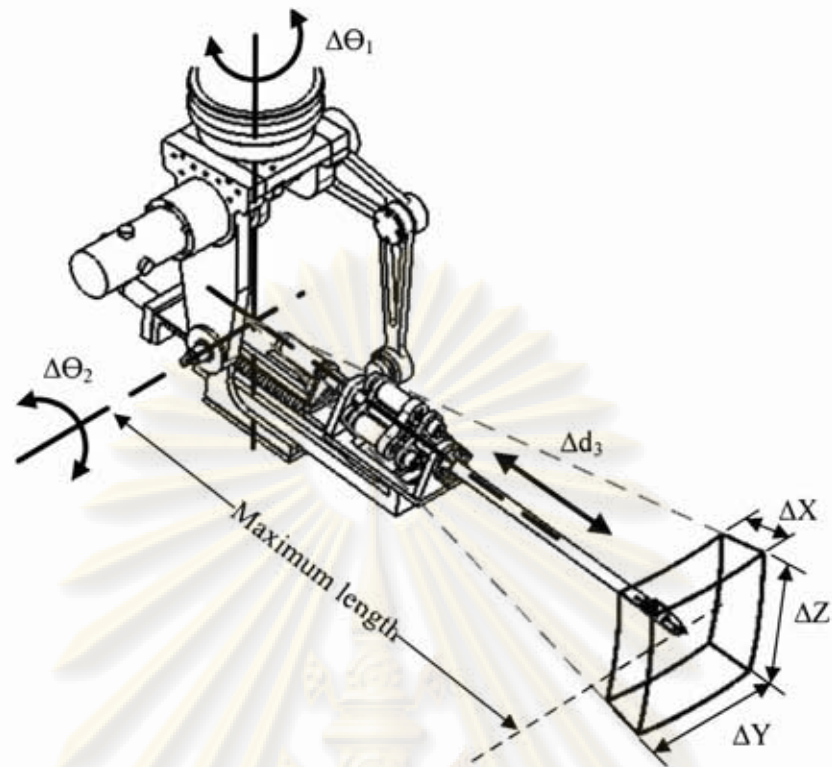
Figure 3.12: Approximate resolution of the overall manipulator

3.3.2.2 Wrist

The intersection of the last three axes at a common point (see Figure 3.13) is preferred in order to obtain the closed-form solution of an inverse kinematics. Hence the concept of an epicyclic gear train has been applied. However, the couple between the 5th and the 6th axis is occurred.
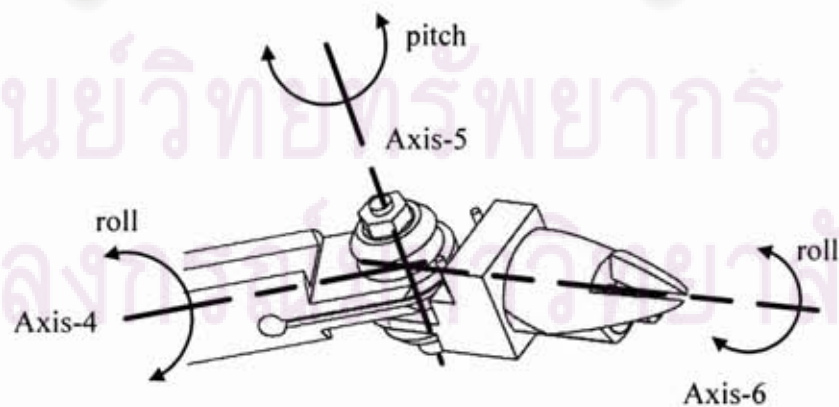
Figure 3.13: A roll-pitch-roll wrist with the intersection of three axes
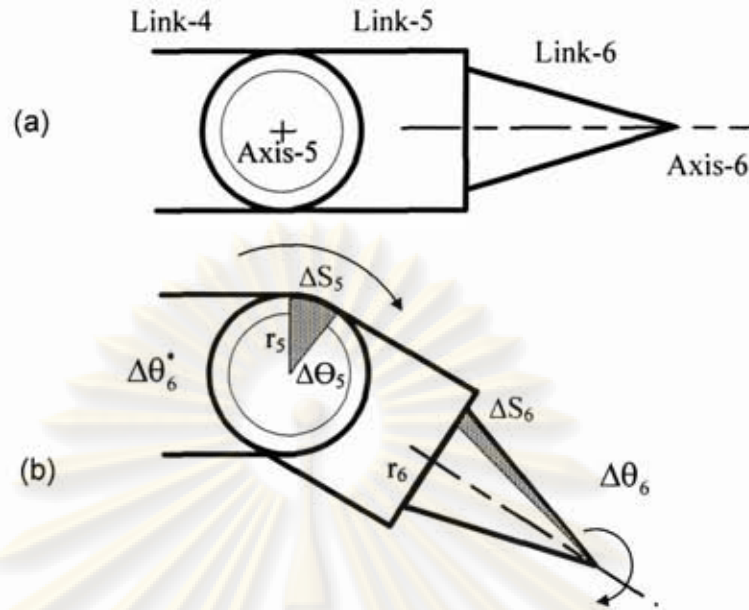
Figure 3.14: Coupled between the 5th and the 6th axis

According to Figure 3.14, the 5th and the 6th axis are obviously coupled, the actual angle of the tip (θ_6) is not equal to the angle measured at the motor ($\theta_6^{\bullet}$), especially when the angle of the 5th axis is not zero (Figure 3.14(b)). Consequently, the compensation is needed in order to obtain the accurate orientation of the tip.

As regard to the displacement of the tendon (ΔS_i) at each axis, the displacement at both sides must be equal (see Equation (3.5)). Thereby the relation of the both angles can be computed from the radius of pulleys. The angle of the tip, which is changed ($\Delta\theta_6^{\bullet}$) with respect to the angle of the 5th axis, can be computed from Equation (3.6). This angle must be add to the desired angle of the tip (θ_6) in order to find the angle of the motor (θ_6). This compensation should be done as in Equation (3.7).

$$\Delta S_5 = \Delta S_6 \tag{3.5}$$

$$r_6 = r_5 \left(\frac{\Delta\theta_5}{\Delta\theta_6^{\bullet}} \right) \tag{3.6}$$

$$\theta_6^{\bullet} = \theta_6 + \left(\frac{r_5}{r_6} \right) \Delta\theta_5 \tag{3.7}$$

Where

θ_i = an actual angle of the axis-i

$\dot{\theta_i}$ = an angle of the axis-i measured at the motor

$\Delta\theta_i$ = an angle changed of the axis-i

r_i = a radius of the pulley on the axis-i

ΔS_i = a displacement of the tendon relates to the pulley-i

3.4 The real parts and assembly

The parts manufactured with CNC-machining and rapid prototyping (RP) are shown in this section. Moreover, the completed assembly of the RCRT-1 Manipulator is presented.

3.4.1 Parts

Most parts of the RCRT-1 Manipulator were manufactured from CNC milling machine. With respect to the requirements of high strength and stiffness, iron, aluminum, and stainless steel were used. CNC is able to manufacture accurate mechanical parts with ±20 μm tolerance. Some of the small machined parts are shown in Figure 3.15.
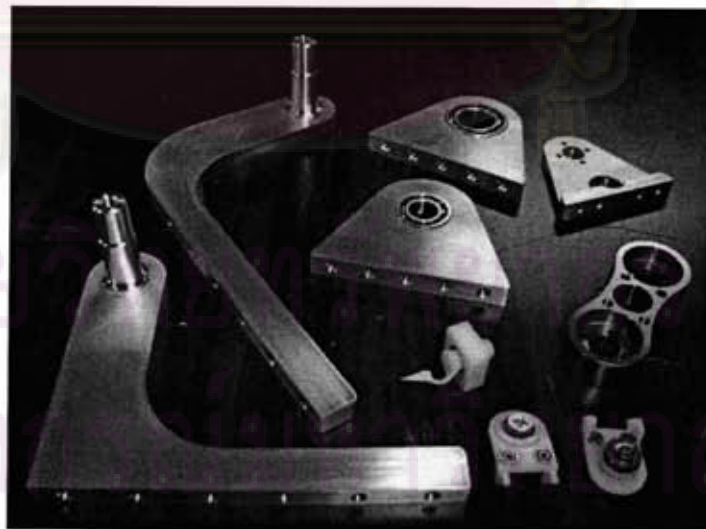
Figure 3.15: Miniature machined parts

As regard to very small parts, these tiny components cannot be manufactured with CNC because of many technical problems, including difficulties in handling and fixtures, requirement of special tools, and limitation of spindle speed. Therefore, the rapid prototyping was preferred to be used to build these small parts. However, the resin and polymer are the main material. Hence, their flexibility reduces the stiffness and strength of these parts. Moreover, accuracy of these parts is lower than that in of the machined parts (±100 μm tolerance). These parts are used as miniature pulleys, the 6th link, and the gripper.
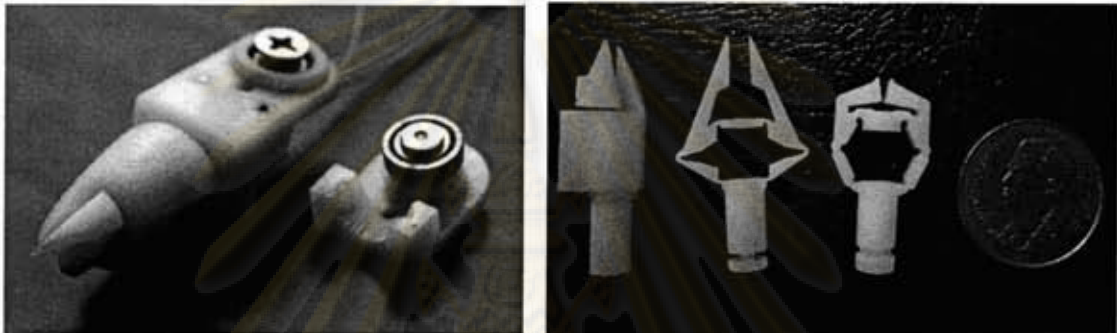
Figure 3.16: The prototype wrists and grippers (fabricated from RP)

3.4.2 The completed assembly of the RCRT-1 Manipulator
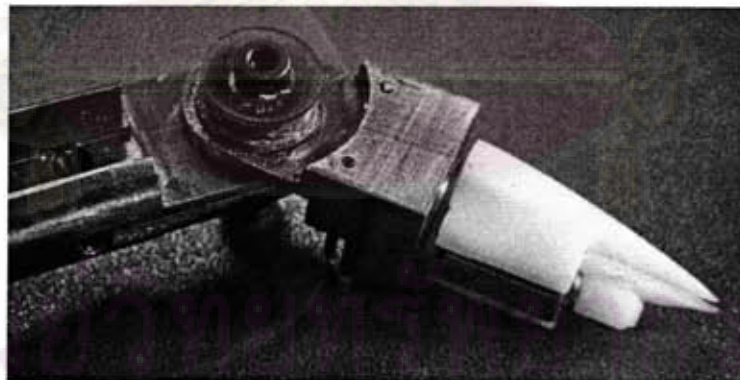
Figure 3.17: The wrist and gripper

The mechanism that merges between machined parts and rapid-prototyping parts are obviously presented in the 5th and the 6th links. In Figure 3.17, a plastic pulley is mounted on the iron link. Moreover, the plastic link (6th) and the gripper are mounted with a tiny motor driving the gripper.
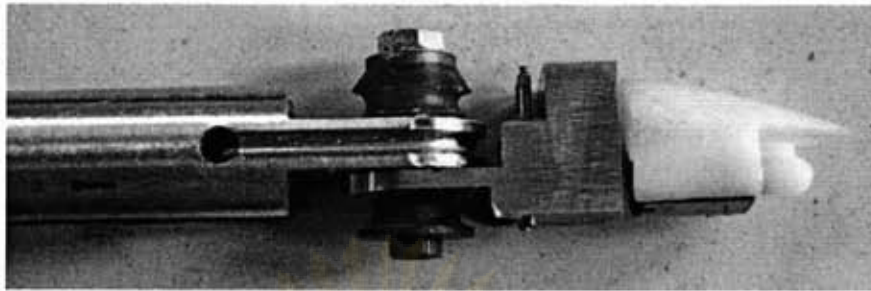
Figure 3.18: The wrist and gripper (top view)
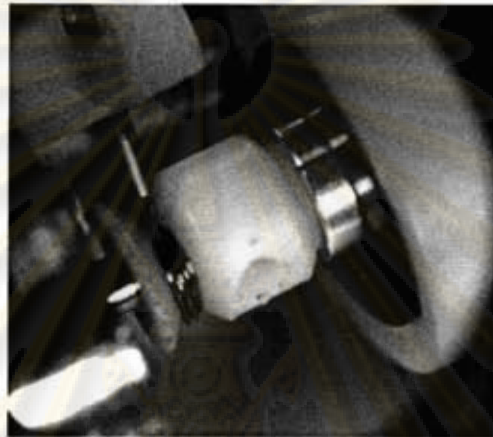
(a)

(b)

Figure 3.19: The pulley of the 5th-axis with a copper wire tendon

(a) The drive - pulley at the actuator

(b) The idler - pulley at the wrist
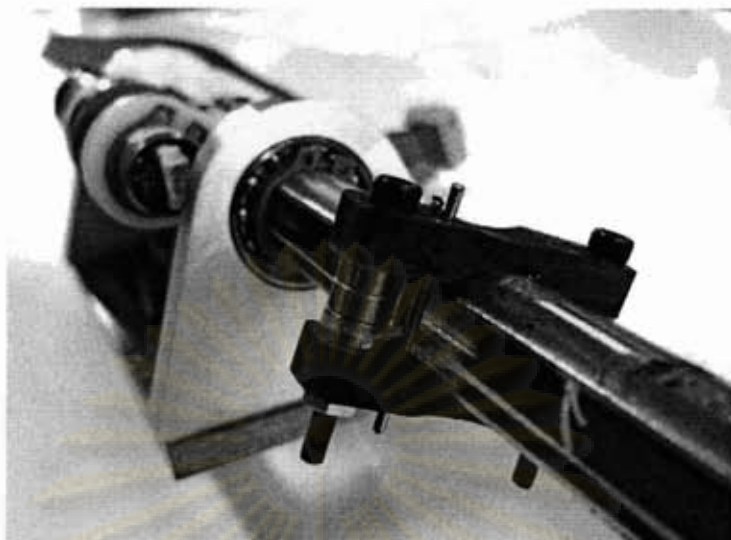
Figure 3.20: Tensioner of the tendon transmission for the 5th and the 6th axis

Figure 3.21: The 5th and 6th actuators with absolute encoders
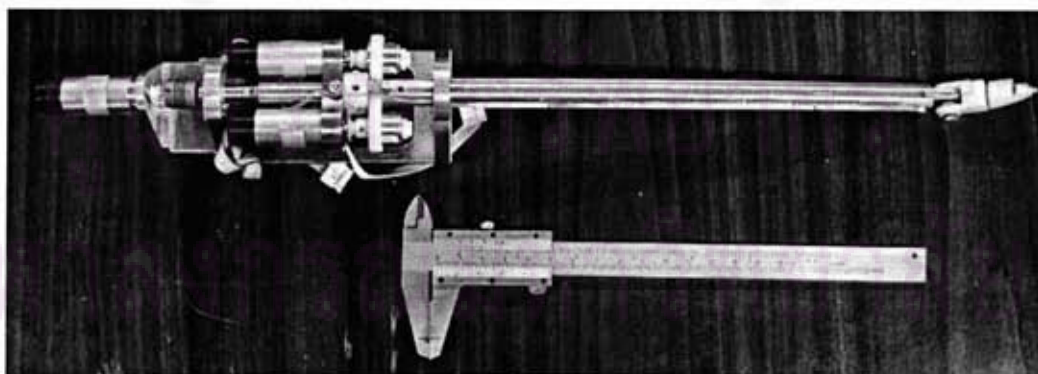
Figure 3.22: The lower arm of the RCRT-1 Manipulator
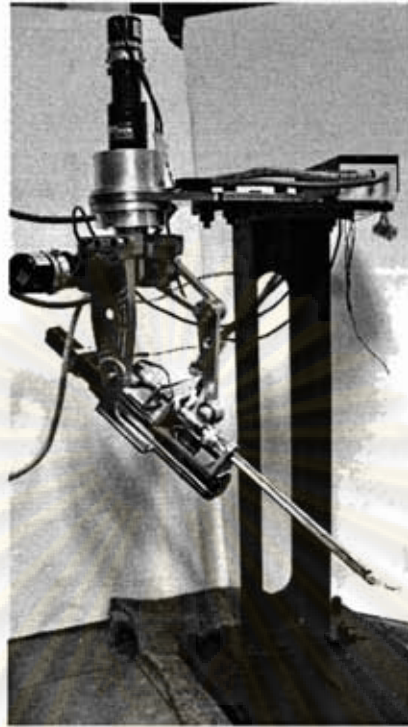
Figure 3.23: The completed assembly of the RCRT-1 Manipulator with its platform

Figure 3.24: The RCRT-1 Manipulator with the human figure

CHAPTER IV

THE SLAVE MANIPULATOR KINEMATICS AND DYNAMICS MODEL

This chapter describes the mathematics model and parameters of the RCRT-1 Manipulator. The physical information, such as link dimension and mass of each link, is clearly presented. Moreover, the related equations, including kinematics and dynamics model, are presented.

4.1 Workspace

The workspace of the RCRT-1 Manipulator is a sphere with respect to the structure of spherical robot. However, the workspace is not a complete sphere (Figure 4.1) because of some mechanical limitations. The vertical movement is apparently limited by singularities of the four-bar linkage and the mechanical obstacle. Meanwhile, the horizontal movement is limited by the robot base platform (not shown in Figure 4.1). However, the limitations in software are constructed in order to prevent undesirable collisions.
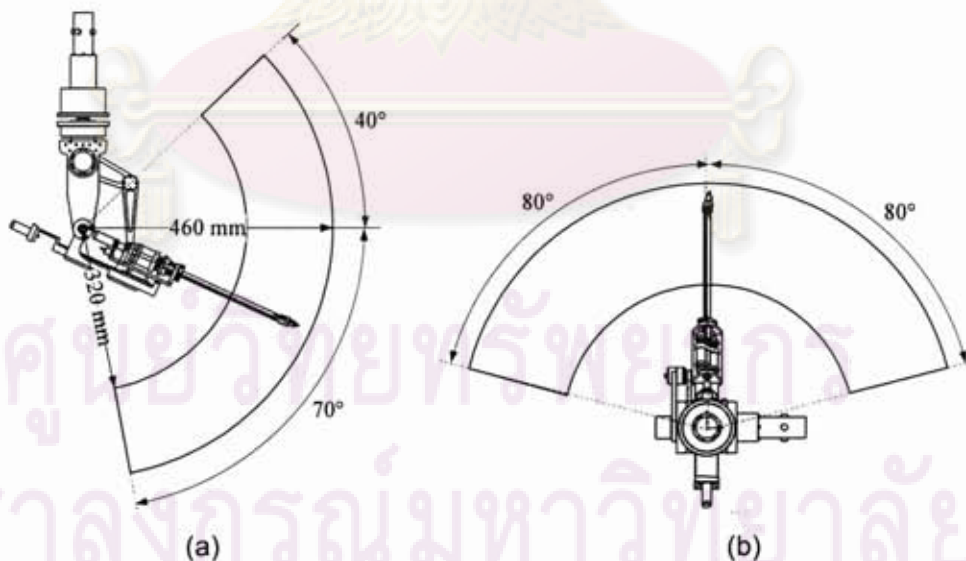
Figure 4.1 The slave manipulator's workspace

(a) side view workspace (b) top view workspace
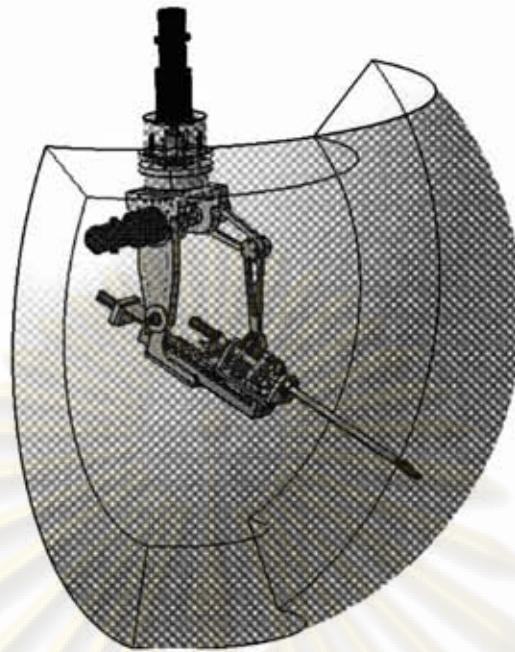
(a) Isometric view with workspace
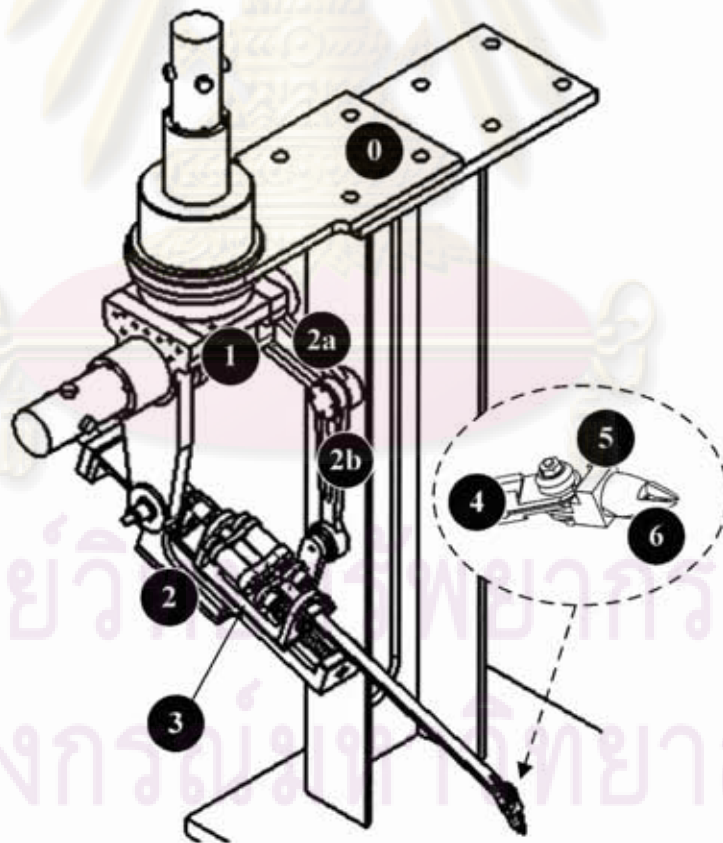
(b) Isometric view with links description

Figure 4.2: Isometric of this manipulator

4.2 Link specifications

Table 4.1 Mass of each link

Link No.	Mass (kg)
1	1.6
2	1.1
2a	0.4
2b	0.2
3	0.5
4	0.2
5	0.01
6	0.002

Because link No.2 and 3 are auxiliary links, they neither present in the Denavit-Hartenberg parameters nor kinematics computation. Moreover, because of the parallel four-bar linkage mechanism, link No.2 and No.4 are always parallel. Consequently, both of them rotate synchronously with the same angle.

4.3 Link-frame attachment

These Denavit-Hartenberg parameters, shown in Table 4.2, describe the links (not include two passive links) configuration of this manipulator.

Table 4.2 Denavit–Hartenberg parameters of this manipulator

i	$a_{i-1}\,(mm)$	α_{i-1}	$d_i\,(mm)$	θ_i
1	$L_1 = 0$	$-90°$	0	θ_1
2	0	$90°$	0	θ_2
3	0	0	d_3	0
4	0	$-90°$	0	θ_4
5	0	$90°$	0	θ_5
6	0	0	$L_6 = 37$	θ_6
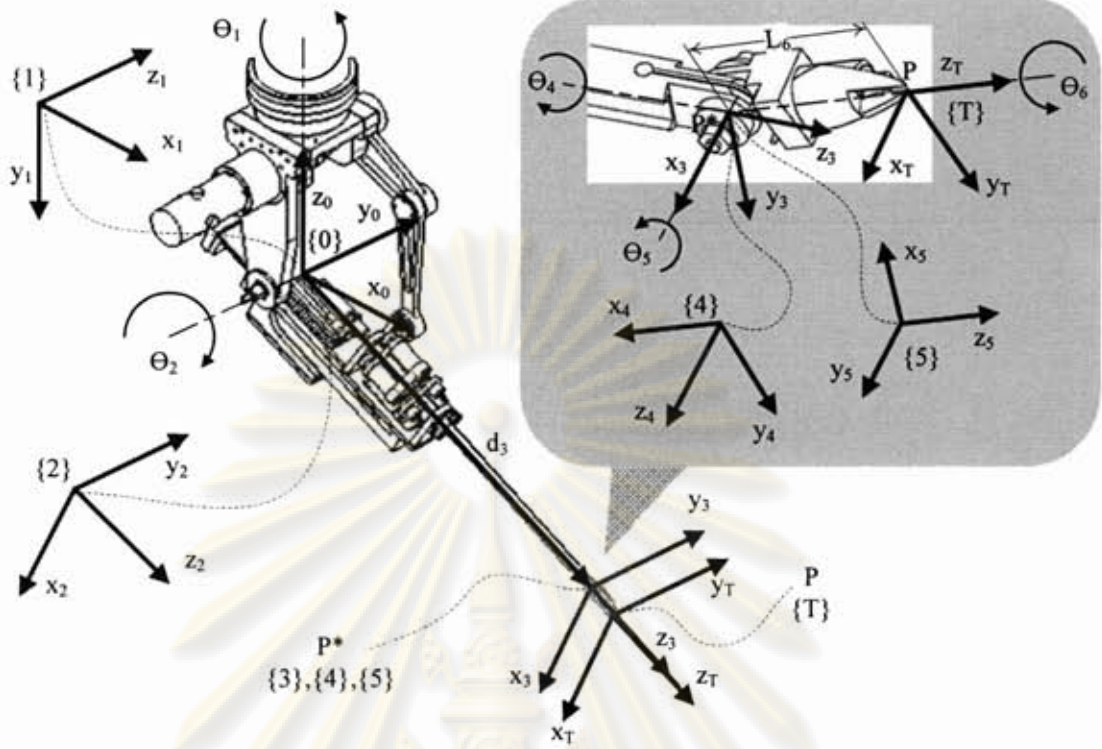
Figure 4.3 Frames attachment
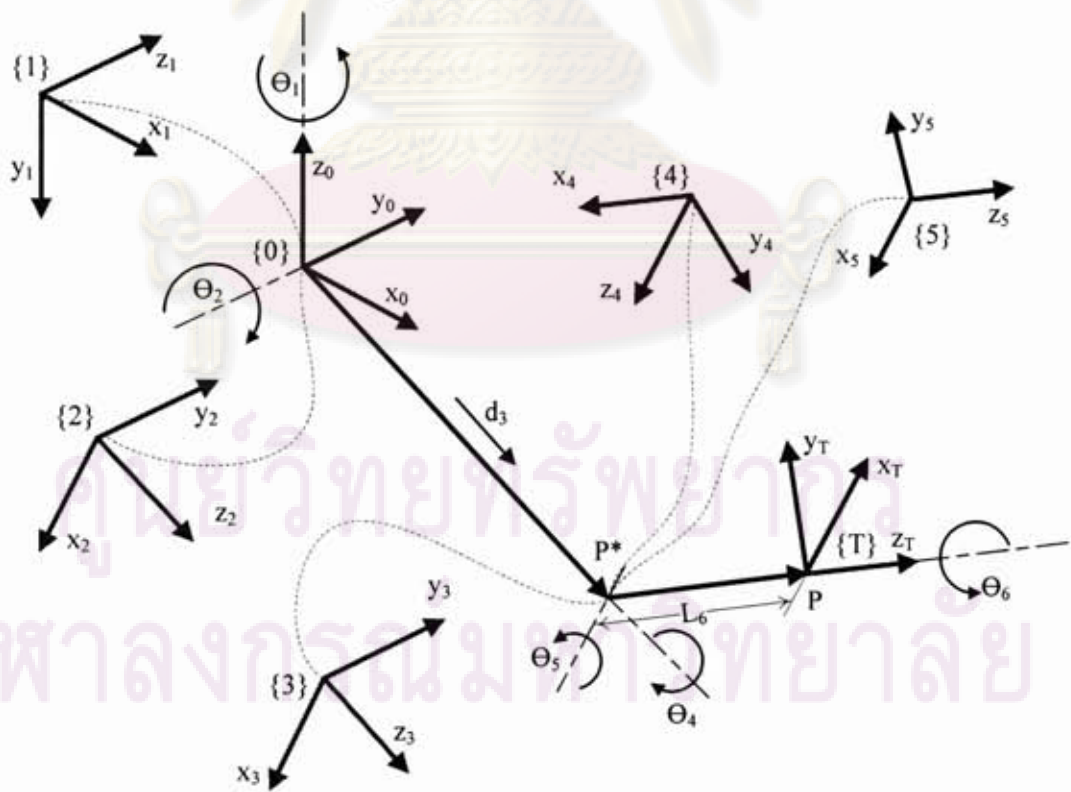
Figure 4.4: Structure schematic diagram

4.4 Forward kinematics

Forward kinematics is used for computing positions and orientations of the end-effector in the operational space from a set of joint variables in a joint space. The forward kinematics equations are usually represented as the transformation matrix. The transformation matrix for the RCRT-1 Manipulator is shown in equation (4.4.1)

$$
^{0}T_{6} = \begin{bmatrix} n_x & o_x & a_x & p_x \\ n_y & o_y & a_y & p_y \\ n_z & o_z & a_z & p_z \\ 0 & 0 & 0 & 1 \end{bmatrix}
$$

(4.4.1)

Where

$$n_x = c_1 \left[c_2 \left(c_4 c_5 c_6 - s_4 s_6 \right) - s_2 s_5 s_6 \right] - s_1 \left(s_4 c_5 c_6 + c_4 c_6 \right)$$

$$n_y = s_1 \left[c_2 \left(c_4 c_5 c_6 - s_4 s_6 \right) - s_2 s_5 s_6 \right] + c_1 \left(s_4 c_5 c_6 + c_4 c_6 \right)$$

$$n_z = -s_2 \left(c_4 c_5 c_6 - s_4 s_6 \right) - c_2 s_5 c_6 s$$

$$o_x = c_1 \left[-c_2 \left(c_4 c_5 s_6 + s_4 c_6 \right) + s_2 s_5 s_6 \right] - s_1 \left(-s_4 c_5 s_6 + c_4 c_6 \right)$$

$$o_y = s_1 \left[-c_2 \left(c_4 c_5 s_6 + s_4 c_6 \right) + s_2 s_5 s_6 \right] + c_1 \left(-s_4 c_5 s_6 + c_4 c_6 \right)$$

$$o_z = s_2 \left(c_4 c_5 s_6 + s_4 c_6 \right) + c_2 s_5 s_6$$

$$a_x = c_1 \left(c_2 c_4 s_5 + s_2 c_5 \right) - s_1 s_4 s_5$$

$$a_y = s_1 \left(c_2 c_4 s_5 + s_2 c_5 \right) + c_1 s_4 s_5$$

$$a_z = -s_2 c_4 s_5 + c_2 c_5$$

$$p_x = \left(c_1 s_2 d_3 - s_1 d_2 \right) + d_6 a_x$$

$$p_y = \left(s_1 s_2 d_3 + c_1 d_2 \right) + d_6 a_y$$

$$p_z = \left(c_2 d_3 \right) + d_6 a_x$$

Where

p_x, p_y, p_z = position of the end-effector relative to frame {0}

$s_i = \sin\left(\theta_i \right)$ and $c_i = \cos\left(\theta_i \right)$

$s_{ij} = \sin\left(\theta_i + \theta_j \right)$ and $c_{ij} = \cos\left(\theta_i + \theta_j \right)$

4.5 Inverse kinematics

Inverse kinematics is used for computing joint variables related to positions and orientations of the end-effector in the operational space. For this manipulator, the closed-form solutions of inverse kinematics can be obtained because of the spherical wrist structure. The solutions are shown in equation (4.5.1) to (4.5.6)

$$p_x = p_x^\bullet + d_6 a_x \tag{4.5.1}$$

$$p_y = p_y^\bullet + d_6 a_y \tag{4.5.2}$$

$$p_z = p_z^\bullet + d_6 a_z \tag{4.5.3}$$

$$\theta_1 = \tan^{-1}\left(\frac{p_y^\bullet}{p_x^\bullet}\right) - \tan^{-1}\left(\frac{d_2}{\pm\sqrt{\left(p_x^\bullet\right)^2 + \left(p_y^\bullet\right)^2 - d_2^2}}\right) \tag{4.5.4}$$

$$\theta_2 = \tan^{-1}\left(\frac{c_1 p_x^\bullet + s_1 p_y^\bullet}{p_z^\bullet}\right) \tag{4.5.5}$$

$$d_3 = s_2\left(c_1 p_x^\bullet + s_1 p_y^\bullet\right) + c_2 p_z^\bullet \tag{4.5.6}$$

$$\theta_4 = \tan^{-1}\left(\frac{-s_1 a_x + c_1 a_y}{c_2\left(c_1 a_x + s_1 a_y\right) - s_2 a_z}\right) \quad ; \theta_4 \neq 0 \tag{4.5.7}$$

A Singularity is occurred when $\theta_5 = 0$ because the 4th and the 6th axis are superimposed. In order to solve this problem, one of them has to be stopped immediately while another one is rotating. In this case, let θ_4 stops.

$$\theta_5 = \tan^{-1}\left(\frac{c_4\left(c_2\left(c_1 a_x + s_1 a_y\right) - s_2 a_z\right) + s_4\left(-s_1 a_x + c_1 a_y\right)}{s_2\left(c_1 a_x + s_1 a_y\right) + c_2 a_z}\right) \tag{4.5.8}$$

$$\theta_6 = \tan^{-1}\left(\frac{s_6}{c_6}\right) \tag{4.5.9}$$

Where

$$s_6 = -c_5 \left(c_4 \left(c_2 \left(c_1 o_x + s_1 o_y \right) - s_2 o_z \right) + s_4 \left(-s_1 o_x + c_1 o_y \right) \right)$$
$$+ s_5 \left(s_2 \left(c_1 o_x + s_1 o_y \right) + c_2 o_z \right)$$
$$c_6 = -s_4 \left(c_2 \left(c_1 o_x + s_1 o_y \right) - s_2 o_z \right) + c_4 \left(-s_1 o_x + c_1 o_y \right)$$

As regard to the θ_5 and θ_6, their joints are driven through the pulleys. Hence, the reduction ratio of the pulleys must be concerned as Equation (4.5.7) and Equation (3.7).

$$\theta_5^\bullet = \left(\frac{r_5}{r_5^\bullet} \right) \Delta \theta_5 \qquad (4.5.10)$$

$$\theta_6^\bullet = \theta_6 + \left(\frac{r_5}{r_6} \right) \Delta \theta_5 \qquad (3.7)$$

Where

$\theta_i^\bullet$ = angle at the motor-i

θ_i = angle of the pulley at the link-i

$r_i^\bullet$ = radius of the driving pulley at the motor-i

r_i = radius of the idler pulley at the link-i

r_5 = 3.5 mm

$r_5^\bullet$ = 2.5 mm

r_6 = 1.8 mm

$r_6^\bullet$ = 2.5 mm

4.6 Dynamics model

The dynamics model of this manipulator is intentionally computed for using in more advanced control, e.g. inverse dynamics and robust control, which may be studied further. However, the gravity term is used in the gravity compensation method (see Chapter VI). As regard to the overall structure, the inertia of last three axes is insignificantly relative to their actuators and the other parts of the manipulator. Consequently, only the first three axes are concerned and presented in the dynamics model.

The "Lagrange-Euler" method [27] was used to find the dynamics model. The general parameters, e.g. the center of gravity coordinate and the moment of inertia, were estimated from the CAD models. Moreover, the gear reduction ratio and the inertia of motor were specified from product catalogs. However, the friction force terms are not considered in this research. The general form of dynamics model is represented as Equation (4.6.1).

$$\tau = \mathbf{D}(q)\ddot{q} + \mathbf{h}(q,\dot{q}) + \mathbf{c}(q) + \mathbf{f}(\dot{q}) \qquad (4.6.1)$$

$$\mathbf{f}(\dot{q}) = \mathbf{F_v}\dot{q} + \mathbf{F_s}\,\mathrm{sgn}(\dot{q}) \qquad (4.6.2)$$

Where

τ	= computed torque (or force)
$\mathbf{D}(q)$	= inertia term
$\mathbf{h}(q,\dot{q})$	= centrifugal force and Coriolis force term
$\mathbf{c}(q)$	= gravity term
$\mathbf{f}(\dot{q})$	= friction force term
$\mathbf{F_v}$	= viscous friction coefficients
$\mathbf{F_s}$	= static friction coefficients
q	= joint variable

Since the friction forces are neglected ($\mathbf{f}(\dot{q}) = 0$), the dynamics model equation was reduced to the following form.

$$\tau = \mathbf{D}(q)\ddot{q} + \mathbf{h}(q,\dot{q}) + \mathbf{c}(q) \qquad (4.6.3)$$

The joint variable q_i represents a joint angle and a joint displacement for the revolute joint and the prismatic joint respectively. These joint variables are represented as $q_1 = \theta_1, q_2 = \theta_2$, and $q_3 = d_3$. Each term is shown in Equation (4.6.4) to (4.6.6).

$$\mathbf{D}(q) = \begin{bmatrix} d_{11} & d_{12} & d_{13} \\ d_{21} & d_{22} & d_{23} \\ d_{31} & d_{32} & d_{33} \end{bmatrix} \qquad (4.6.4)$$

Where

$$d_{11} = -\left[I_{3xx} + I_{2xx} - I_{2zz} + 2d_3 m_3 G_{3z} + d_3^2 m_3 \right] c_2^2 + \left[d_3 m_3 G_{3x} + I_{2xz} \right] s_{22}$$
$$\qquad + 2d_3 m_3 G_{3z} + d_3^2 m_3 + I_{3xx} + I_{1yy} + I_{2xx} + k_{r1}^2 I_{1m}$$
$$d_{12} = d_{21} = -\left[2d_3 m_3 G_{3z} + d_3^2 m_3 + I_{3xx} \right] c_2^2 + d_3 m_3 G_{3x} s_{22} + 2d_3 m_3 G_{3z} + d_3^2 m_3 + I_{3xx}$$
$$d_{13} = d_{31} = 0$$
$$d_{22} = 2d_3 m_3 G_{3z} + d_3^2 m_3 + I_{3yy} + I_{2yy} + k_{r2}^2 I_{2m}$$
$$d_{23} = d_{32} = -m_3 G_{3x}$$
$$d_{33} = m_3$$

$$\mathbf{h}(q,\dot{q}) = \begin{bmatrix} h_1 \\ h_2 \\ h_3 \end{bmatrix} \qquad (4.6.5)$$

Where

$$h_1 = \left[\left(m_3 d_3^2 + 2m_3 d_3 G_{3z} + I_{2xx} - I_{2zz} + I_{3xx} \right) s_{22} + \left(2d_3 m_3 G_{3x} + 2I_{2xz} \right) c_{22} \right] \dot{\theta}_1 \dot{\theta}_2$$
$$\qquad + m_3 \left[G_{3x} s_{22} + (d_3 + G_{3z})(1 - c_{22}) \right] \left(\dot{\theta}_1 \dot{d}_3 + \tfrac{1}{2} \dot{\theta}_2 \dot{\theta}_3 \right)$$
$$h_2 = 2m_3 \left[G_{3z} + d_3 \right] \dot{\theta}_2 \dot{d}_3 - \left[\tfrac{1}{2} \left(d_3^2 m_3 + 2d_3 m_3 G_{3z} I_{xx3} - I_{zz2} + I_{xx2} \right) s_{22} + \left(d_3 m_3 G_{3x} + I_{xz2} \right) c_{22} \right] \dot{\theta}_1^2$$
$$h_3 = m_3 \left[(G_{3z} + d_3) c_{22} + \tfrac{1}{2} G_{3x} s_{22} \right] \dot{\theta}_1^2 - m_3 \left[G_{3z} + d_3 \right] \dot{\theta}_2^2$$

$$\mathbf{c}(q) = \begin{bmatrix} C_1 \\ C_2 \\ C_3 \end{bmatrix} \qquad (4.6.6)$$

Where

$$C_1 = 0$$
$$C_2 = -g\left(\left(m_2 G_{2z} + m_3 G_{3z} + m_3 d_3 + m_{2b} L_{0b}\right)s_2 + \left(m_2 G_{2x} + m_3 G_{3x}\right)c_2\right)$$
$$C_3 = m_3 g c_2$$

Where

m_i = mass of link-i

G_{ij} = location of center of gravity of link-i along j-axis

I_{ijk} = moment of inertia of link-i about axis-jk

I_{mi} = moment of inertia of the motor-I (without harmonic gear)

k_{ri} = gear reduction ratio of motor-i

L_{0b} = distance between origin of {0} and point-b

From Equation (4.6.3) – (4.6.6), the dynamics model is:

$$\begin{bmatrix} \tau_1 \\ \tau_2 \\ F_3 \end{bmatrix} = \begin{bmatrix} d_{11} & d_{12} & d_{13} \\ d_{21} & d_{22} & d_{23} \\ d_{31} & d_{32} & d_{33} \end{bmatrix} \begin{bmatrix} \ddot{\theta}_1 \\ \ddot{\theta}_2 \\ \ddot{d}_3 \end{bmatrix} + \begin{bmatrix} h_1 \\ h_2 \\ h_3 \end{bmatrix} + \begin{bmatrix} C_1 \\ C_2 \\ C_3 \end{bmatrix} \qquad (4.6.7)$$

Since the actuator of the 3rd axis is not a prismatic actuator, the computed force F_3 has to be transformed to the computed torque τ_3 for the motor. The relation between the torque and force in a ball-screw is in Equation (4.6.8).

$$\tau_i = \frac{F_i D_p}{2}\left[\frac{L_d + \mu \pi D_p}{\pi D_p - \mu L_d}\right] + \left(J_{motor} + J_{screw}\right)\left(\frac{2\pi \ddot{d}_i}{L_d}\right) \pm \tau_{friction} \qquad (4.6.8)$$

Where

D_p = pitch diameter of ball screw

L_d = lead of the screw in mm per revolution

μ = coefficient of friction for rolling contact

$J_{motor} + J_{screw}$ = Inertia of motor and ball screw

$\tau_{friction}$ = overall resistance torque ($\pm$ depends on the moving direction)

CHAPTER V

THE MASTER DEVICE: PHANTOM OMNI® HAPTIC DEVICE

This chapter gives information of the Phantom Omni Haptic Device, which is used as the master device in this research. Typically, the information is divided into 2 main topics: general specifications and programming.

5.1 Specifications of the master device

The master device must have sufficient dexterity in order to use in the teleoperation. In general, a 6-DOF master device is able to provide sufficient reference command for positions and orientations of the slave end-effector. Moreover, back-drivability and force interaction are the other important characteristics of the master device. The back-drivability allows users to move the master device comfortably without getting stuck. Meanwhile the force interaction is used for the force feedback control, called "the haptic system". Furthermore, high resolution and accuracy are important requirements.

"The PHANTOM Omni® Haptic device" [22] (see Figure 5.1) meets all requirements for the good master device. Consequently, it has been chosen for using in this research.

5.2 Overview

The Phantom is a product of the SensAble Technologies Inc. It is one of the most popular and cost-effective haptic devices at present. It provides effective sense of touch which makes the user can touch and manipulate virtual objects. A lot of commercial software that manipulate with virtual objects – e.g. FreeForm™ and ClayTools™ – is compatible for using with this haptic device. Moreover, this device is usually found in many haptic projects. Other qualifications, including portable design, compact size, easy installation, and ease-of-use, make this haptic device very useful in various kinds of application. The highlighted features of this device are listed as follow [22]:

- 6-DOF positional sensing
- Portable design and compact footprint (base) for workspace flexibility
- Comfortable and removable stylus
- Two integrated switches on the stylus for user customization
- Compact workspace
- Wrist rest to maximize user comfort
- Automatic workspace calibration
- Well manufactured and robustness structure with CE certified

Figure 5.1 PHANTOM Omni® Haptic Device

5.3 Technical specifications

The typical features, such as the physical information, resolution, and force feedback, are presented in the user manual. The official technical features are presented in Table 5.1.

Table 5.1: The Phantom's official technical specifications [22]

Force feedback workspace	~6.4 W x 4.8 H x 2.8 D in. > 160 W x 120 H x 70 D mm.
Footprint (Physical area device base occupies on desk)	6 5/8 W x 8 D in. ~168 W x 203 D mm.
Weight (device only)	3 lbs. 15 oz.
Range of motion	Hand movement pivoting at wrist
Nominal position resolution	> 450 dpi.(~ 0.055 mm.)
Backdrive friction	<1 oz (0.26 N)
Maximum exertable force at nominal (orthogonal arms)position	0.75 lbf. (3.3 N)
Continuous exertable force (24 hrs.)	> 0.2 lbf. (0.88 N)
Stiffness	X axis > 7.3 lbs/ in (1.26 N / mm.) Y axis > 13.4 lbs/ in (2.31 N / mm.) Z axis > 5.9 lbs/ in (1.02 N / mm.)
Inertia (apparent mass at tip)	~0.101 lbm. (45 g)
Force feedback	x, y, z
Position sensing [Stylus gimbal]	x, y, z (digital encoders) [Pitch, roll, yaw ($\pm$ 5% linearity potentiometers)]
Interface	IEEE-1394 FireWire® port
Supported platforms	Intel or AMD-based PCs
OpenHaptics™ SDK compatibility	Yes

5.4 Configurations and structures

Configuration of the first three axes of the Phantom is similar to an articulated manipulator. Three actuators that generate interacting force are located on the base of the Phantom. The force can be produced in three orthogonal directions, X-Y-Z. The 1st and the 2nd axis are driven by the actuators directly, while the 3rd is actuated through a tendon drive (see Figure 5.2). However, interacting torques can not be generated by the Phantom because none of the actuators are presented for driving the wrist. Overall, the Phantom can completely sense positions and orientations (6-DOF), but only 3 directional forces can be generated.

Because the exact kinematics parameters, e.g. link lengths and axes attachments, are not revealed by the manufacturer. The possible kinematic configuration (see Figure 5.3) has been assumed approximately for further understanding. As regard to the output transformation matrix sent from the Phantom, only information of base frame {B} and tool frame {T} can be determined.

However, the complete set of information can be obtained from its specific software, named "The OpenHaptics toolkit". The details are described in the following topics.
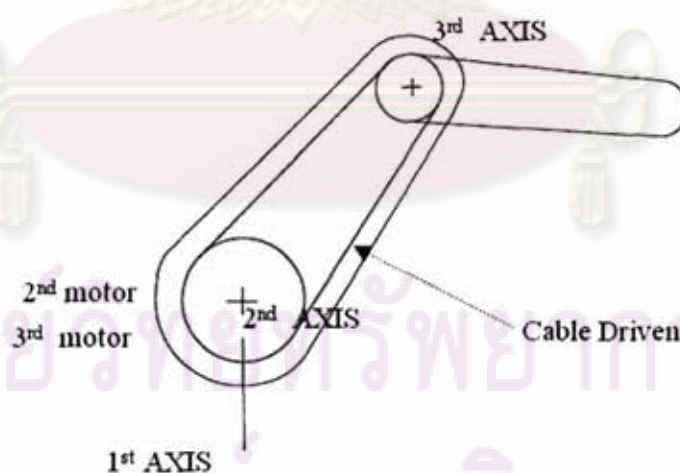
Figure 5.2: The 2nd axis and the 3rd axis power transmissions
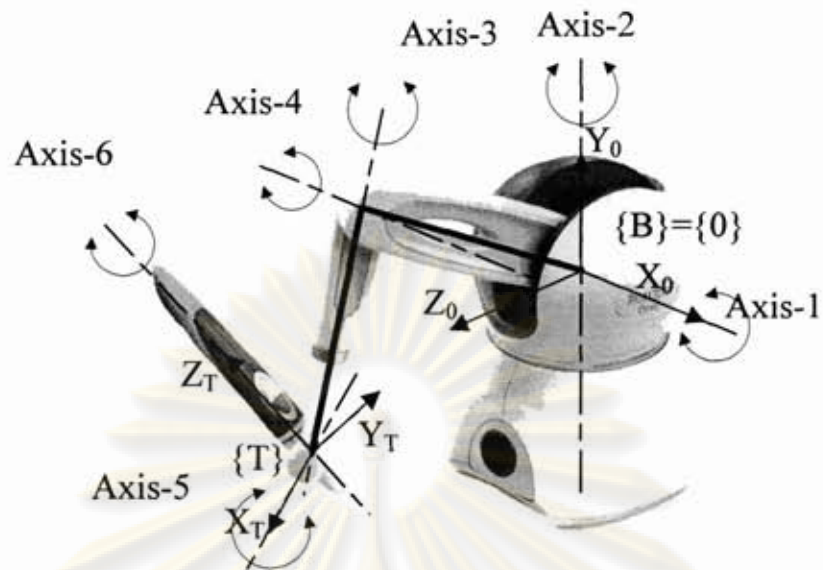
Figure 5.3: Configuration of The PHANTOM Omni® (assumed)

5.5 Programming

5.5.1 OpenHaptics toolkit overview

The Phantom can be effectively communicated with the users and computers via the specific software named "the OpenHaptics toolkit". This software includes many necessary files covering a lot of major applications. The files are listed as follows:

- Haptic Device API (HDAPI)
- Haptic Library API (HLAPI)
- Phantom Device Drivers (PDD)
- Utilities
- Source Code Examples
- Programmer's Guide
- API Reference

The HDAPI enables haptics programmers to render forces directly. It offers control over configuring the runtime behavior of the drivers, and provides convenient utility features and debugging aids. The HLAPI provides high-level haptic rendering and is designed to be familiar to OpenGL® API programmers. It allows significant reuse of

existing OpenGL code and greatly simplifies synchronization of the haptics and graphics threads. The Phantom Device Drivers support all currently Phantom devices. The utilities provide some useful accessories for users [24].

In this research, only the HDAPI features are used because they can provide all necessary functions for accessing the low-level control of the Phantom (see Appendix C). However, only some functions have been used, such as:

- Get device state: position, orientation, and velocity
- Asynchronous scheduler
- Device calibration
- Force output in Cartesian space

5.5.2 Programming for the general servo-loop control

The servo-loop is definitely needed for the feedback control. The clock generator featured in the Phantom provides the interrupt signal through HDAPI. The signal is generated in every 0.001 seconds (1,000 Hz sampling). The five main steps of servo-loop operation are concluded as follows:

1) Initialize the device
2) Create a scheduler callback to take care of the positions and forces
3) Enable device forces
4) Start the scheduler
5) Clean up the device and scheduler when the application is ended

This procedure is associated with four groups of function, including initialization, scheduler callbacks, getting information, and generating output force. They are explained in the following sections.

5.5.2.1 Initialization

The initialization process is required prior to other operations. This process consists of identifying the device, connecting, enabling output force, and starting scheduler.

5.5.2.2 Scheduler callbacks

The scheduler callback can be operated in two modes, "a synchronous call" or "an asynchronous call". The synchronous call is primarily used for acquiring a snapshot of the device states. Meanwhile the asynchronous call is the best mechanism for managing the haptics loop (servo-loop). In this research, the device is totally operated with the asynchronous call at 1,000 Hz sampling rate. This sampling rate is fast enough for implementing the common feedback control. The scheduler callback function is called in every servo-loop. Therefore, the functions related to the control Phantom and RCRT-1 Manipulator must be contained in this callback function. The flowchart in Figure 5.4 shows the typical procedure in the asynchronous scheduler.

5.5.2.3 Getting information

States and other information of the master device can be retrieved through the *hdGet* family. However, the most important information needed for control is information of the state, including positions, velocities, orientations etc. In this research, only the transformation matrix is needed in order to provide the reference commands for the RCRT-1 Manipulator.

5.5.2.4 Generating output force

The force module must be enabled in the initialization process. The commands of interacting force are sent to directly to actuators through the *hdSet* family.
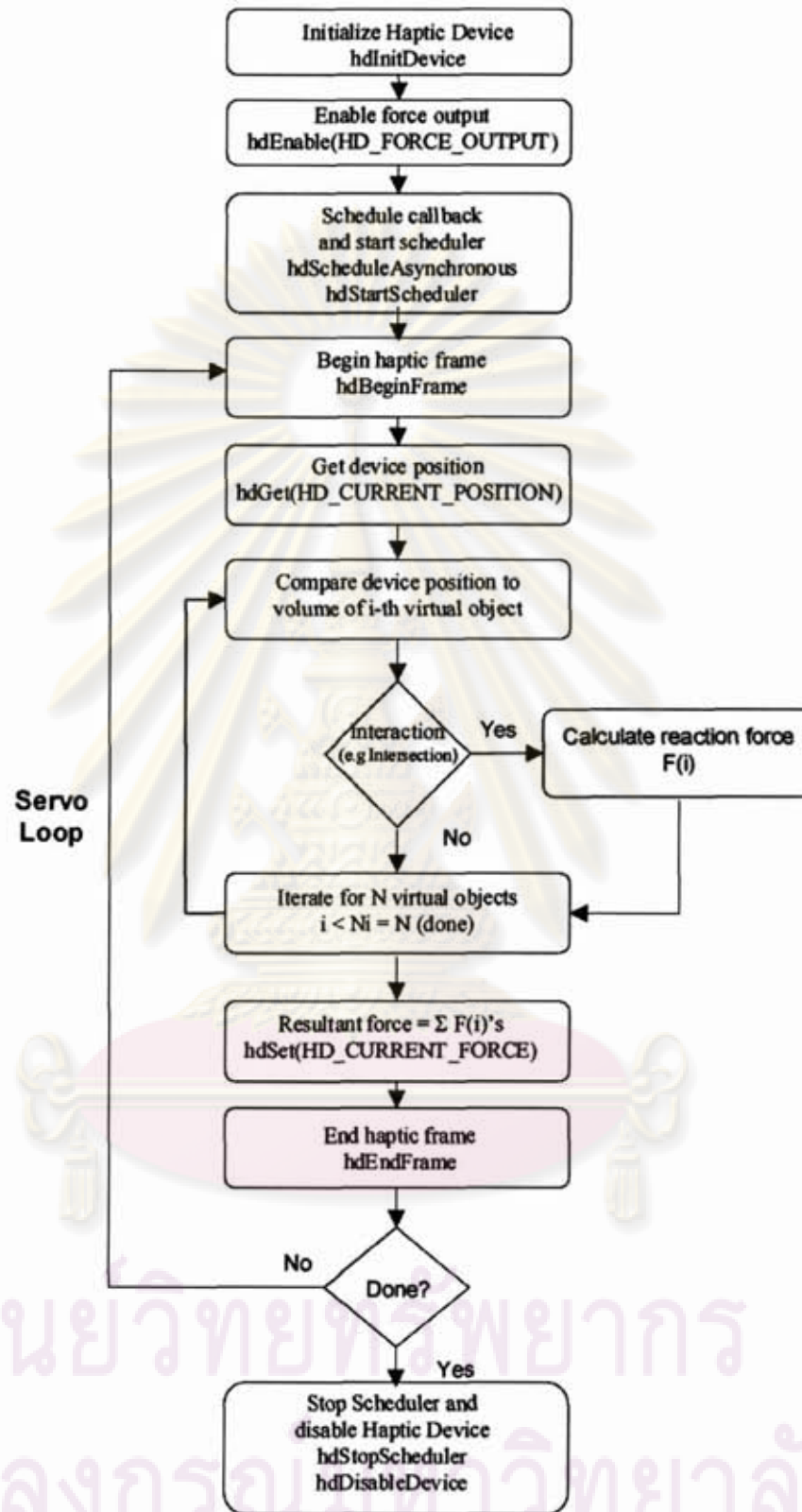
Figure 5.4: Typical flowchart of an HDAPI program (Asynchronous) [24]

CHAPER VI

CONTROL

This chapter describes specifications and designs of control system used in the RCRT-1 Manipulator. Typically, the desired specifications of the motion control and the PID-controller with gravity compensation are clearly explained in the first section. Moreover, a connection between the master device and the slave manipulator is explained in the second part. Moreover, the additional components that increase the teleoperation performance are also described in the third section. Finally, some user interface software are described in brief.

6.1 The slave manipulator motion control

6.1.1 Task requirements

The control schemes are designed based on the task requirements of the RCRT-1 Manipulator with respect to application of teleoperation and miniature tasks. The typical requirements are:

- Accurate static and dynamic positioning
- Rapid coarse motions
- Low speed and smooth fine motions
- Stability
- No overshoot

6.1.1.1 Accurate static and dynamic positioning

In case of the completely automatic operations (without master devices), the accuracy in static positioning is more necessary. On the contrary, the accuracy in dynamic positioning is more important for teleoperation. In addition to mechanical errors, the position error is typically caused by the effects of external factors, e.g.

friction force and gravity. These errors can be eliminated by a proper control scheme, such as I-controller.

6.1.1.2 Rapid coarse motions

The coarse motions are used to roughly approach the working area rapidly. High precision and high accuracy are not required. Moreover, overshooting can be occurred easily because of high speed movements. This overshooting can be reduced by trajectory control that regulates positions and velocities to change gradually. However, the trajectory control is neglected in the master-slave operation because the users can automatically control their hand to move smoothly.

6.1.1.3 Low speed and smooth fine motions

The motion mode is switched to the fine motion when the end-effector of the RCRT-1 Manipulator has approached the desired working area. Higher accuracy and higher precision than that in the coarse motion mode is needed. Moreover, the trajectory control can be totally ignored because the slave manipulator moves very slowly. Consequently, positions and velocities are slightly changed. This movement is regulated by "the position amplifier gain". The movement of the slave manipulator can be lengthened or shortened relative to the Phantom. In practice, the amplifier gain = 0.1 is typically used in the fine motion mode (see Topic 6.2).

6.1.1.4 Stability

Rapidly unpredicted movements and violent oscillation are occurred in case of instability [17]. These uncontrollable movements lead to critical damages of the manipulator. Consequently, the manipulator must be stable in order to avoid these problems. In general, design of stability can be realized from a lot of methods, for instance Routh's stability criterion, Nyquist criterion [25], or Lyapunov direct method [30].

6.1.1.5 No overshoot

Occurring of overshooting while operating in limited space can lead to undesirable collision. Hence, it must be totally prevented. The overshooting can be eliminated by carefully regulating movement of each joint. The motion controller must be designed based on a critical-damp situation in order to obtain the best response. Moreover, the trajectory may be used in addition.

6.1.2 Control schemes

The proper control schemes have to be considered with respect to the dynamics model of the RCRT-1Manipulator. The general form of the dynamics model is shown in Equation (6.1) (see Topic 4.6 for more detail).

$$\tau = \mathbf{D}(q)\ddot{q} + \mathbf{h}(q,\dot{q}) + \mathbf{c}(q) + \mathbf{F}_v\dot{q} + \mathbf{F}_s\,\text{sgn}(\dot{q}) \tag{6.1}$$

Where

τ	= computed torque (or force)
$\mathbf{D}(q)$	= inertia term
$\mathbf{h}(q,\dot{q})$	= centrifugal force and Coriolis force term
$\mathbf{c}(q)$	= gravity term
$\mathbf{f}(\dot{q})$	= friction force term
$\mathbf{F}_v$	= viscous friction coefficients
$\mathbf{F}_s$	= static friction coefficients
q	= joint variable
	- Joint angle (θ) for a revolute joint
	- Displacement (d) for a prismatic joint

As regard to Equation (6.1), nonlinearities are apparently presented in the model because of many factors, including friction force, inertia, gravity, and centrifugal force and Coriolis force. These terms obviously depend on joint angles and joint velocities. However, the proper mechanism design can reduce some of these nonlinearities and limited their undesirable effects (see Chapter III). Each term is considered separately.

First, high torque actuators can overcome the effects from variation of inertia that occurred while the manipulator moves. Second, these high toque actuators can partially overcome fiction force and gravity effects. Third, the centrifugal force and Coriolis force are marginally produced because of slow movements. Consequently, they have little effect.

However, all of these errors can be regulated by the proper controller with feed-forward compensators.

6.1.2.1 PID-Control

The PID-Controller is very simple control system, regardless of complex dynamics model. As the nonlinear terms in the model are ignored, the model becomes decentralize. Therefore, the controller is implemented on each axis individually. However, the control scheme is operated on the digital computer. Hence, the control software is developed based on a discrete time system. In this research, typical sampling rate is 1,000 Hz which is fast enough to maintain performance and stability of this servo system.
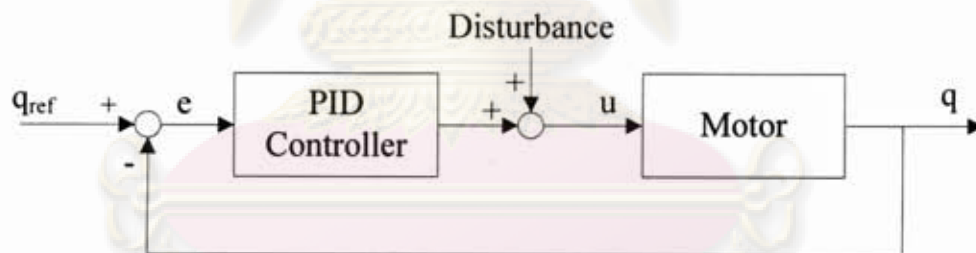
Figure 6.1: A feedback control scheme using PID-controller

A PID-Control scheme, shown in Figure 6.1, can be implemented on either continuous or discrete control system. According to the diagram, the error signal (e) is the different between the reference signal (q_{ref}) and the output sensing signal (q). Subsequently, the torque (u) is computed from the error signal and sent to the amplifier for driving the motor. The disturbances represent undesirable factors, for example frictions, gravity, external loads, and signal noise. Even though the exact parameters of these disturbances cannot be known, I-Controller can partially bound their undesired effects. This diagram can be written as transfer functions for continuous and discrete time system. They are shown in Equation (6.1.2) and (6.1.3) respectively.

Continuous time system	$u(s) = \left(K_P + \dfrac{K_I}{s} + K_D s \right) e(s)$	(6.1.2)

Discrete time system	$u(k) = u_P(k) + u_I(k) + u_D(k)$	(6.1.3)

Proportion controller:	$u_P(k) = K_P e(k)$	(6.1.4)

Integration controller:	$u_I(k) = u(k-1) + K_I T e(k)$	(6.1.5)

Differentiation controller	$u_D(k) = \dfrac{K_D}{T}\left[e(k) - e(k-1) \right]$	(6.1.6)

Where

u = a computed torque

e = an error signal:

$$e(k) = q_{ref}(k) - q(k-1) \qquad (6.1.7)$$

K_P = a proportion control gain

K_I = an integration control gain

K_D = a differentiation control gain

T = sampling period (second)

6.1.2.2 PID-Control with gravity compensation

The gravity has significant effects on the precision, especially for the 2nd axis. The high power motor, relative to the weight of the manipulator, can minimize this effect. However, this high power motor makes the manipulator large and awkward. The other effective method is adjusting the suitable integral gain (K_I). The steady state error can be decreased but the tracking error still presents. Consequently, the gravity compensator should be considered in order to improve tracking ability.

The gravity compensator is added in addition to the PID-control. The additional computed torque from gravity compensator $g(q)$ is the function of the joint

positions only. However, the calculation is not as complex as the inverse dynamics. The diagram of control scheme is shown in Figure 6.2.

In this research, the gravity effects with respect to the last three axes are neglected because of their tiny size. Consequently, the gravity compensation will be implemented only on the 2nd axis.
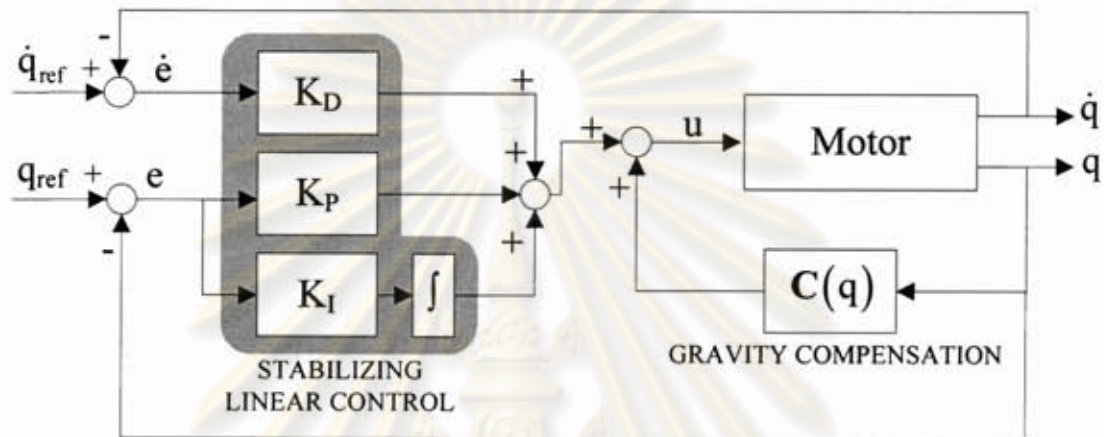
Figure 6.2: A PID-Control with gravity compensation
(Implemented on the 2nd axis only)

6.2 Connection between the master device and the slave manipulator

The transformation matrix from the Phantom is sent to the control system in order to command the movement of the RCRT-1 Manipulator. The transformation matrix is obtained through HDAPI library (see Topic 5.5.2). Next, the reference movement may be amplified or diminished with respect to the motion amplifier gain (see Topic 6.2.2.3). Afterwards, it will be computed by inverse kinematics equations (see Topic 4.5). Subsequently, the reference joint angles are obtained. These reference angles are sent through the controller for computing the torques. Finally, this torque signals (voltage reference signal) are amplified by the power amplifier and sent to each motor of the RCRT-1 Manipulator.

Overall, this typical process is represented as a diagram in Figure 6.3. The other details of the program are described in the following sections.
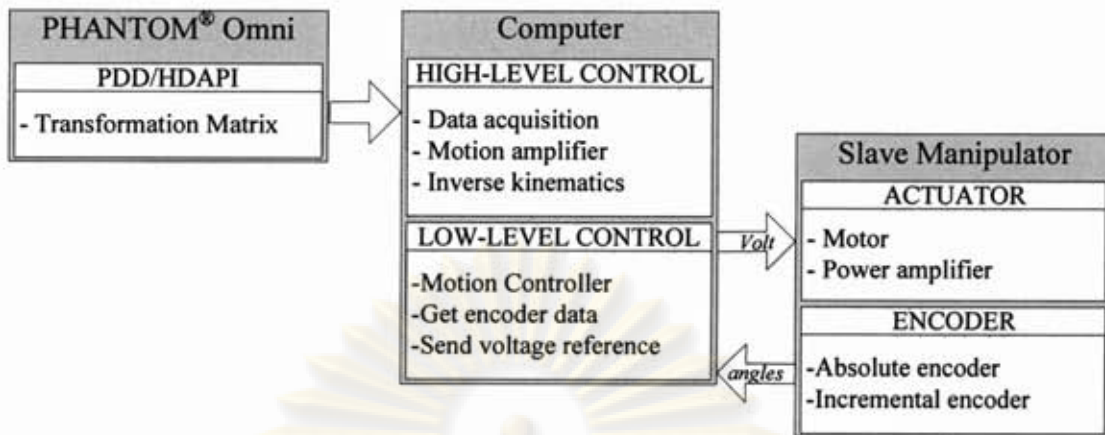
Figure 6.3: The diagram of overall system operation

6.2.1 Level of control

AS regard to the slave manipulator, the control schemes can be separated into two levels: "high-level control" and "low-level control". The high-level control deals with the path reference that is interpreted from the master device. Afterwards, the reference joint angles for the slave manipulator are obtained. This high-level control is described in detail and clearly illustrated as a flowchart in Figure 6.4. On the other hand, the low-level control deals with the motors driving. The PID-controller with gravity compensation is implemented on the low-level control.
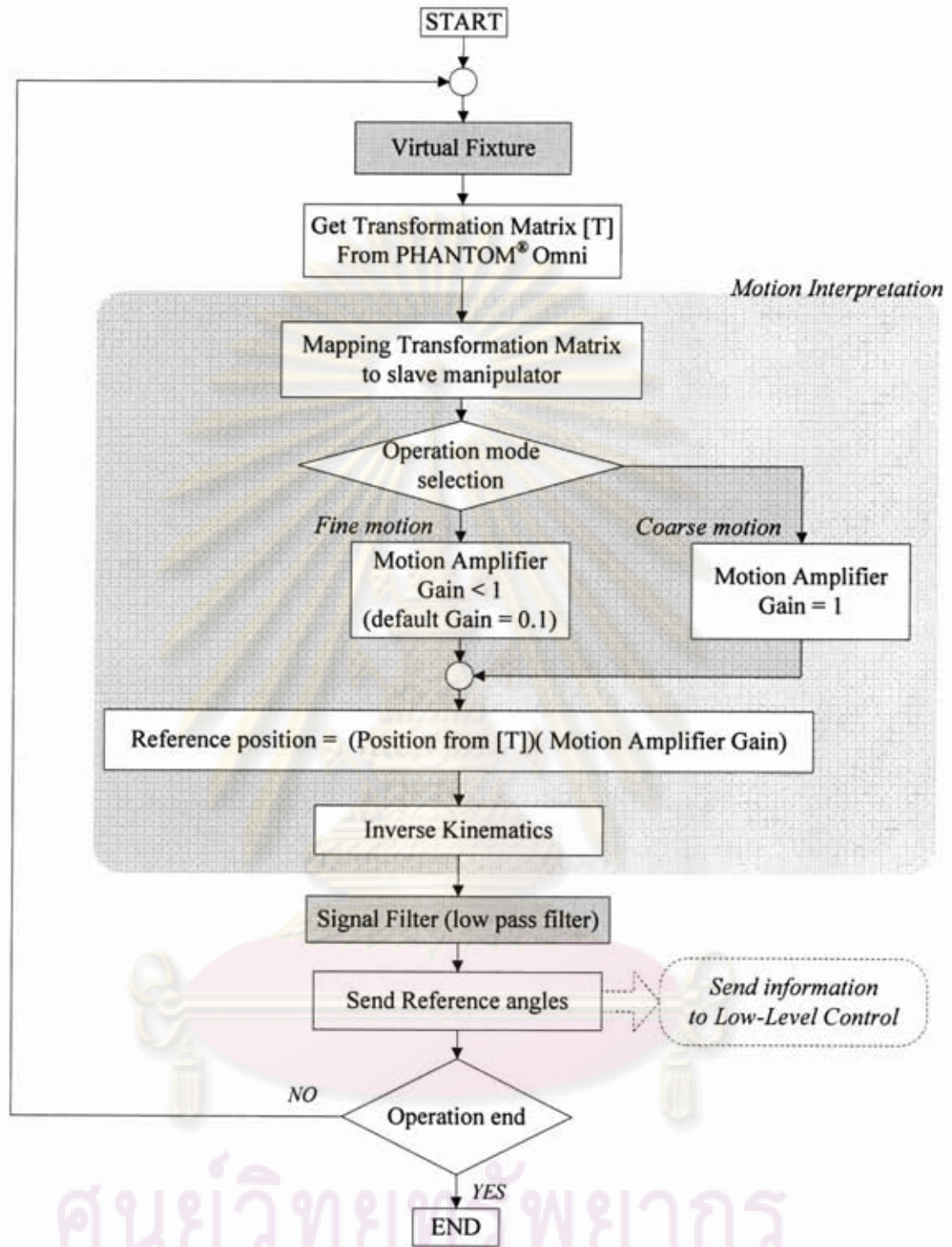
Figure 6.4: The flowchart for the high-level control of the slave manipulator

6.2.2 Movement interpretation

6.2.2.1 Transformation matrix mapping

According to the difference of the frame configurations between the Phantom and the RCRT-1 Manipulator (see Figure 6.5), the transformation matrix from the master device cannot be used straightforwardly. Consequently, this transformation matrix must be mapped to the matrix which is related to the slave manipulator. Mapping can be done by the following Equation (6.2.1).

$$ {}_{ST}^{SB}\mathbf{T} = {}_{PB}^{SB}\mathbf{T}\, {}_{PT}^{PB}\mathbf{T}\, {}_{ST}^{PT}\mathbf{T} \qquad (6.2.1) $$

Where

SB	= the base frame of the slave manipulator
ST	= the tool frame of the slave manipulator
PB	= the base frame of the Phantom® Omni
PT	= the tool frame of the Phantom® Omni
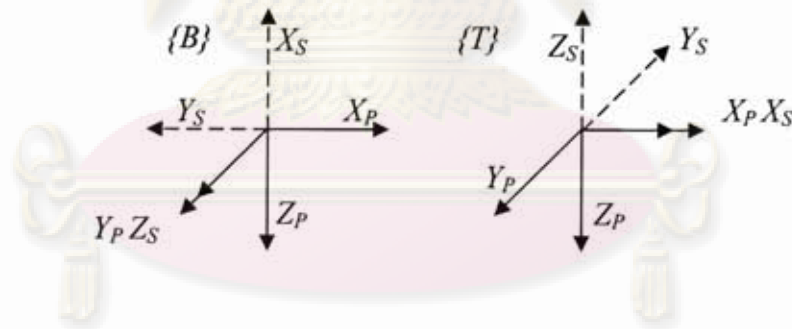
Figure 6.5: {B} and {T} frame attachment

The frame arrangements presented in Figure 6.5 are occurred when the base and the end-effector of both robots point to the same direction. As regard to this Figure, ${}_{PB}^{SB}\mathbf{T}$ describes the frame {B} of the Phantom relative to the frame {B} of the slave manipulator and ${}_{ST}^{PT}\mathbf{T}$ describes the frame {T} of the slave manipulator relative to the frame {T} of the Phantom.

Substitute the value of ${}_{PB}^{SB}\mathbf{T}$ and ${}_{ST}^{PT}\mathbf{T}$ of into Equation (6.2.1). Consequently, the reference transformation matrix ${}_{ST}^{SB}\mathbf{T}$ for the slave manipulator is obtained. Finally, the

reference transformation matrix with respect to the RCRT-1 Manipulator is shown in Equation (6.2.3).

$$
{}^{SB}_{ST}\mathbf{T} =
\begin{bmatrix}
0 & 0 & -1 & 0 \\
-1 & 0 & 0 & 0 \\
0 & 1 & 0 & 0 \\
0 & 0 & 0 & 1
\end{bmatrix}
\begin{bmatrix}
n_x & o_x & a_x & p_x \\
n_y & o_y & a_y & p_y \\
n_z & o_z & a_z & p_z \\
0 & 0 & 0 & 1
\end{bmatrix}
\begin{bmatrix}
1 & 0 & 0 & 0 \\
0 & -1 & 0 & 0 \\
0 & 0 & -1 & 0 \\
0 & 0 & 0 & 1
\end{bmatrix}
\tag{6.2.2}
$$

$$
{}^{SB}_{ST}\mathbf{T} =
\begin{bmatrix}
-n_z & o_z & a_z & -p_z \\
-n_x & o_x & a_x & -p_x \\
n_y & -o_y & -a_y & p_y \\
0 & 0 & 0 & 1
\end{bmatrix}
\tag{6.2.3}
$$

6.2.2.2 Home position

Both robots are at their home positions when the operation is started. The end-effector of the Phantom is located at the inkwell. At this location, the stylus is 23.4° inclined. Consequently, the end-effector of the RCRT-1 Manipulator has to be set to the same orientation as the stylus of the Phantom. Moreover, the home position of the end-effector of the slave manipulator can be set to any location. Thereby, the location that makes the slave manipulator provides large working area is preferred.

The 2nd joint is set to be 113.4°, which is associated with the orientation of the stylus. Furthermore, the home position of the 3rd axis (prismatic joint) is at the end of the slider slot. This location provides the largest working range in Y-Direction of the slave manipulator. Both of the end-effectors are at their farthest position.

The transformation matrix from the Phantom has to be offset with respect to the slave manipulator. In general, the default position of the end-effector at the inkwell is $[p_x, p_y, p_z] = [0.0, 65.511, 88.114]\ mm$, while the desired position of the end-effector of the Phantom is $[p_x', p_y', p_z'] = [0.000, -194.414, -416.901]\ mm$. Consequently, the proper offsets must be added to each direction. The information of the home positions of each robot are shown in Table 6.1 and 6.2. Nevertheless, the posture of each robot at the home position is clearly illustrated in Figure 6.6.

Table 6.1: Home position of the Phantom and slave manipulator (Approximated values)

	Phantom (no offset)	Slave manipulator
x	0 mm	−416.901 mm
y	−65.511 mm	0 mm
z	−88.114 mm	−194.414 mm
roll	23.40°	23.40°
pitch	0°	0°
yaw	0°	0°

Table 6.2: Joints position at the home position of the slave manipulator

Joint	Joint Range (limited by Physical & program)
$\theta_1 = 0°$	$\theta_1 = (-80°, 80°)$
$\theta_2 = 113.4°$	$\theta_2 = (50°, 160°)$
$d_3 = 421\ mm$	$d_3 = (0, 421)\ mm$
$\theta_4 = 0°$	$\theta_4 = (-170°, 170°)$
$\theta_5 = 0°$	$\theta_5 = (-80°, 80°)$
$\theta_6 = 0°$	$\theta_6 = (-170°, 170°)$
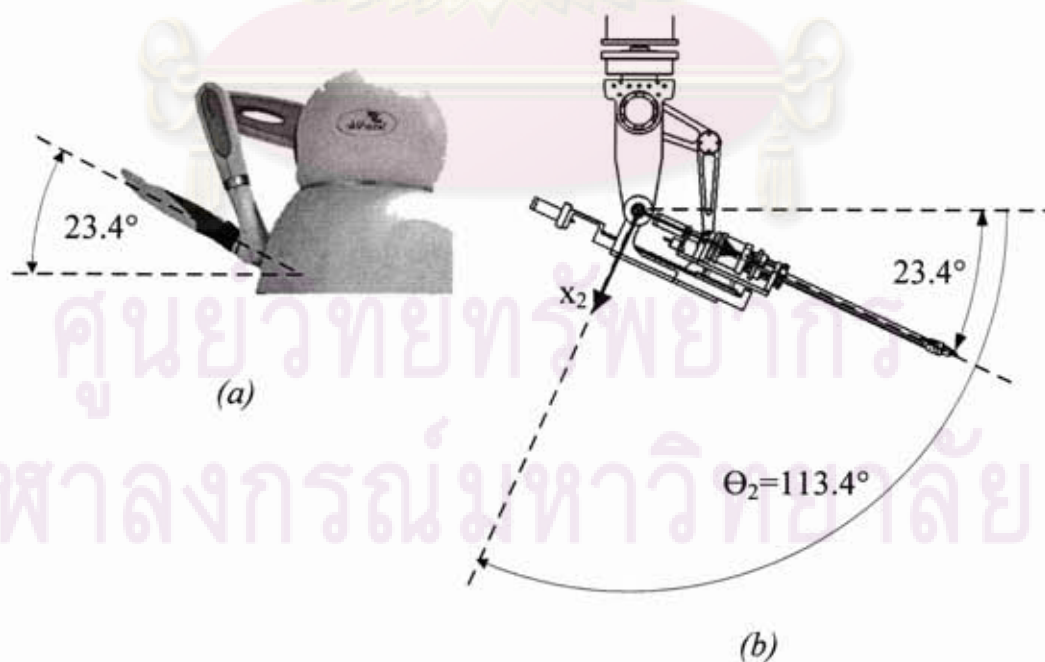
Figure 6.6: Configuration at home positions of the Phantom (a)

and the RCRT-1 Manipulator (b)

Figure 6.7: The RCRT-1 Manipulator at home position (real operation)

6.2.2.3 Switching between coarse and fine mode

The slave manipulator can be operated in two modes, which are "coarse motion" and "fine motion". The orientations of the master device and the slave manipulator are similar during operations. This similarity provides appropriate sense of control for the users. On the contrary, their positions can be different with respect to the position amplifier gain. The movement can be amplified or diminished according to the specific tasks. Moreover, as regard to the effective working, the motion mode must be able be switched anytime. Furthermore, the slave must be able to work smoothly while switch the mode.

Figure 6.8 describes the relation of the movement of both end-effectors. The upper path line is respect to the end-effector of the Phantom, while the lower path line is respect to the end-effector of slave manipulator. As the motion mode may be changed anytime, positions have to be captured at every sampling loop (every 0.001 second for 1000 Hz sampling rate) in order to maintain smooth movement
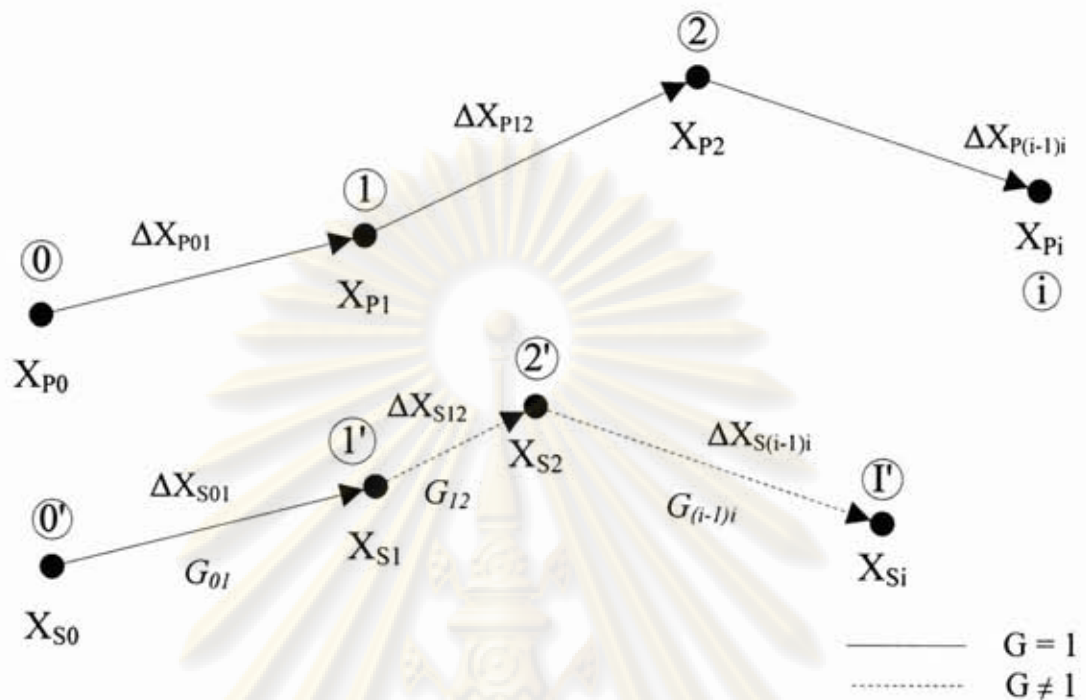
Figure 6.8: Movement path of the end-effector positions
the Phantom (upper) and the slave manipulator (lower)

Where

X_{P0} = home position of the end-effector of the Phantom

X_{Pi} = the end-effector of the Phantom at the position-i

ΔX_{Pij} = distance between the position i and j

X_{S0} = home position of the end-effector of the slave manipulator

X_{Si} = the end-effector of the slave manipulator at the position-i

ΔX_{Sij} = distance between the position i and j

G_{ij} = motion amplifier gain between position i and j

Note: "X" refers to the position vector; $\bar{X} = \begin{bmatrix} P_x & P_y & P_z \end{bmatrix}^T$

The recent position of the RCRT-1 Manipulator ($\mathbf{X}_{Si}$) can be computed from the information of the movement of the Phantom, the previous slave position, and motion-amplified gain at that time. The $\mathbf{X}_{Si}$ can be obtained from Equation (6.2.4) to (6.27).

$$\Delta\mathbf{X}_{P(i-1)i} = \mathbf{X}_{Pi} - \mathbf{X}_{P(i-1)} \tag{6.2.4}$$

$$\Delta\mathbf{X}_{S(i-1)i} = G_{(i-1)i}\left(\Delta\mathbf{X}_{P(i-1)i}\right) \tag{6.2.5}$$

$$\mathbf{X}_{Si} = \mathbf{X}_{S(i-1)} + \Delta\mathbf{X}_{S(i-1)i} \tag{6.2.6}$$

Substitute (6.10) and (6.11) into (6.12), then

$$\mathbf{X}_{Si} = \mathbf{X}_{S(i-1)} + G_{(i-1)i}\left(\mathbf{X}_{Pi} - \mathbf{X}_{P(i-1)}\right) \tag{6.2.7}$$

In each sampling loop, this end-effector position $\mathbf{X}_{Si}$ is computed and used to find the transformation matrix for the slave manipulator ($^{PB}_{PT}\mathbf{T}'_i$). This matrix can be obtained by replacing $\mathbf{X}_{Pi}$ in the matrix $^{PB}_{PT}\mathbf{T_i}$ with $\left(\mathbf{X}_{Pi} - \mathbf{X}_{P(i-1)}\right)G_{(i-1)i} + \mathbf{X}_{S(i-1)}$. This procedure is clearly described in the flowchart of Figure 6.9.

START

Assign initial value of $X_{P(i-1)}$ and $X_{S(i-1)}$
Equal to the position offsets of the both robots
$k = 0$

Get transformation matrix from Phantom

$$_{PT}^{PB}T_i = \left[\begin{array}{c|c} _{PT}^{PB}R_i & X_{Pi} \\ \hline 0 & 1 \end{array} \right]$$

Compute the corrected transformation matrix
for the slave manipulator

$$_{PT}^{PB}T_i' = \left[\begin{array}{c|c} _{PT}^{PB}R_i & \left(X_{Pi} - X_{P(i-1)} \right) G_{(i-1)i} + X_{S(i-1)} \\ \hline 0 & 1 \end{array} \right]$$

Transformation matrix mapping

$$_{ST}^{SB}T_i = {}_{PB}^{SB}T \left[{}_{PT}^{PB}T_i' \right] {}_{ST}^{PT}T$$

$k \leftarrow k + 1$

Inverse kinematics of $_{ST}^{SB}T_i$

Send reference angles to
the low-level control

Store the previous values for the
next sampling loop
$X_{S(i-1)} \leftarrow X_{Si}$
$X_{P(i-1)} \leftarrow X_{Pi}$

Operation end

END

Figure 6.9: The flowchart of the motion interpretation procedure

6.3 Additional components

This section describes the additional components in the controller software that enhance the capability of this master-slave system. However, if these components had been removed, the system would have worked properly but marginally decreased in overall performance. These components are presented in the flowchart in Figure 6.4.

6.3.1 Signal filter

Because the last three joint angles of the Phantom are sensed by linear potentiometers, some noises from these analog sensors are presented in the signal. This noise leads to the inaccurate motion of the RCRT-1 Manipulator. Therefore, vibration and jittering are occurred and obviously notified.

In this research, the low-pass filter is implemented to the reference angle in the high-level control. Afterwards, the filtered reference signal is sent to each motor in the slave manipulator (see Figure 6.5). The low pass filter design is based on phase lag compensation. The transfer function is shown in Equation (6.2.8) and the block diagram is shown in Figure 6.10.

$$G_{filter}(s) = K_0 \left(\frac{s+a}{s+b} \right) \quad ; a > b \qquad (6.2.8)$$
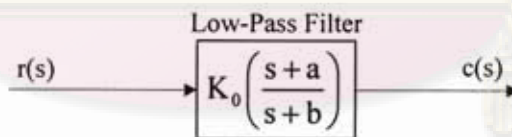
Figure 6.10: A block diagram of the low-pass filter

This transfer function must be transformed in order to use in the discrete time system. After estimating by the Euler equation, the transfer function is expressed in Equation (6.2.9).

$$c(k) = (1+bT)c(k-1) + K_0(aT-1)r(k-1) + K_0 r(k) \qquad (6.2.9)$$

Where

c = filtered reference signal

r = reference signal from the Phantom

T = sampling period = 1 ms (1000 Hz)

After adjusting the parameters based on the response of the reference signal, the appropriate parameters used in this research are a =100, b = 10, and K_0 = 0.1. Comparing between two signals from the simulation, the raw signal fluctuates within $\pm 2 \times 10^{-3}$ rad range, while the range of fluctuation of the filtered signal is reduced to $\pm 5 \times 10^{-4}$ rad. A comparison between raw and filtered signal is illustrate in Figure 6.11.
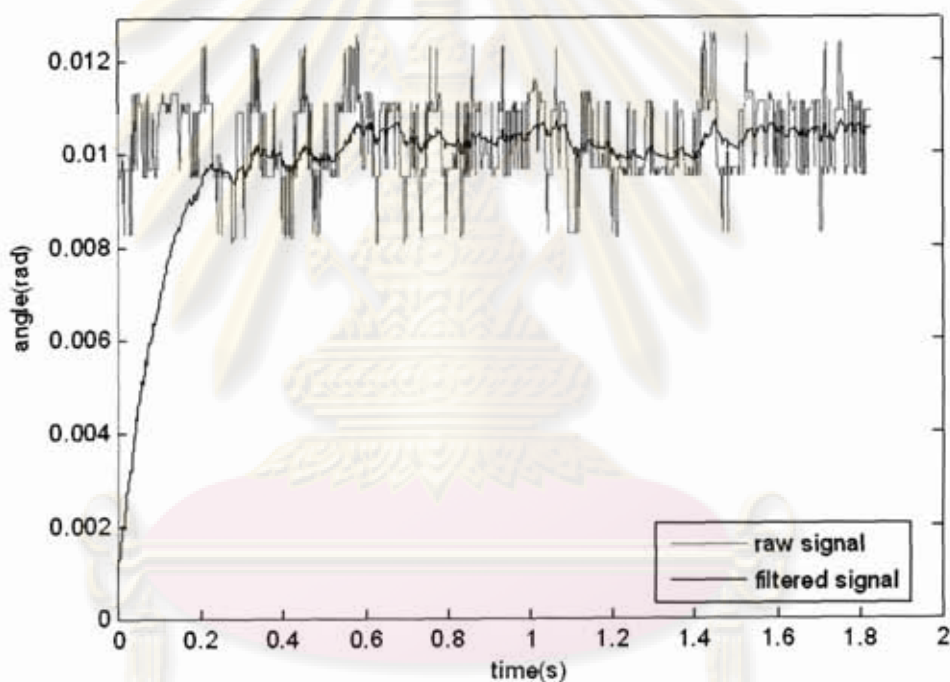
Figure 6.11: A comparison between reference signals
before and after using low-pass filter

6.3.2 Virtual fixture

In the fact that the slave manipulator is difficult to control by common users, who lack of practice and not accustom to the system. Consequently, the virtual fixture is constructed in order to provide more comfortable and effective control. The virtual fixture can limit the movement within the desired working area. The virtual fixture can be constructed in various shapes, for example a square box, a cylinder, or a sphere.

As the virtual fixture is enabled, the movement of the master device is limited by forces produced by the Phantom. These interacting forces are generated in three directions (X, Y, and Z) and can be commanded straightforwardly through the HDAPI library (see Topic 5.5.2.4).

In this research, the shape of the virtual fixture was set to be a cube. Because a cube is bounded by walls, the "virtual wall" may be called in this case. The equations related to a volume control of cubes are very simple. Moreover, each edge of the cube can be used as a straight line guiding path. Furthermore, the size of the walls relates to the movement of the Phantom. Therefore, as regard to the slave manipulator, the size of the walls is adapted with respect to the position amplifier gain (see Figure 6.12).

Master Device side
Virtual Fixture

Slave manipulator side
Virtual Fixture

Gain = 1

Gain = 0.1

Forbidden area

Forbidden area
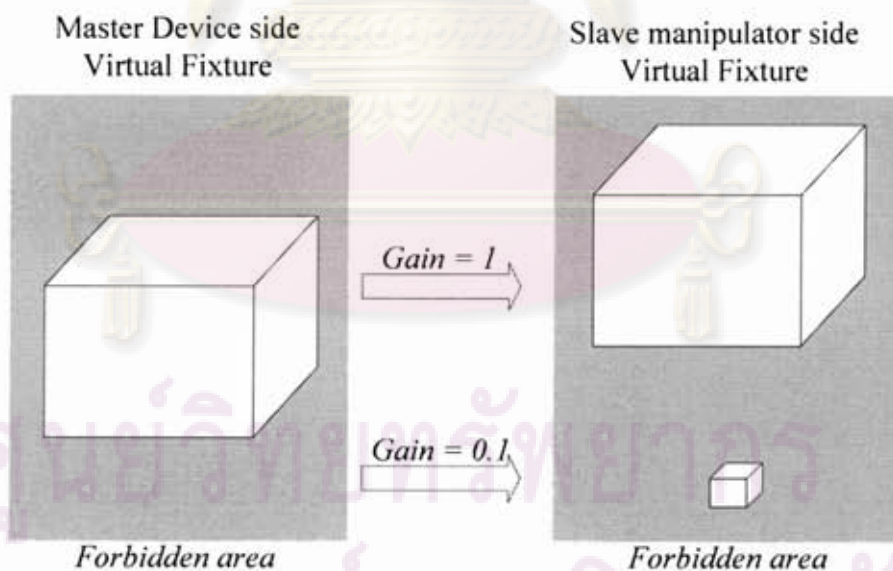
Figure 6.12: The box-shape virtual fixtures relate to the amplified gain

During the operation, the virtual fixture can be enabled or disabled by the users anytime. The status can be changed by pressing the 2nd button on the stylus without losing movement smoothness. As the button has been pushed, the position of the end-

effector of the Phantom is saved as the "enable position". Afterwards, the wall boundaries are immediately computed and created. The users can move the end-effector of the Phantom freely inside this cube only. If the end-effector approaches the forbidden area outside the cube, the pushing force will be produced in the opposite direction perpendicular to the wall. Moreover, to assume that these virtual walls act as the spring-mass system, there are two boundaries: "hard wall" and "soft wall" (see Figure 6.12). The pushing force gradually rises during the end-effecter penetrate deeper in the soft wall zone. Moreover, the maximum force is produced while the end-effecter enters the hard wall zone. However, the size of maximum force is limited by the Phantom specification (3.3 N).

This virtual fixture can be terminated (disabled) by pushing this button again. The overall procedure related to the virtual fixture is described in the flowchart in Figure 6.14
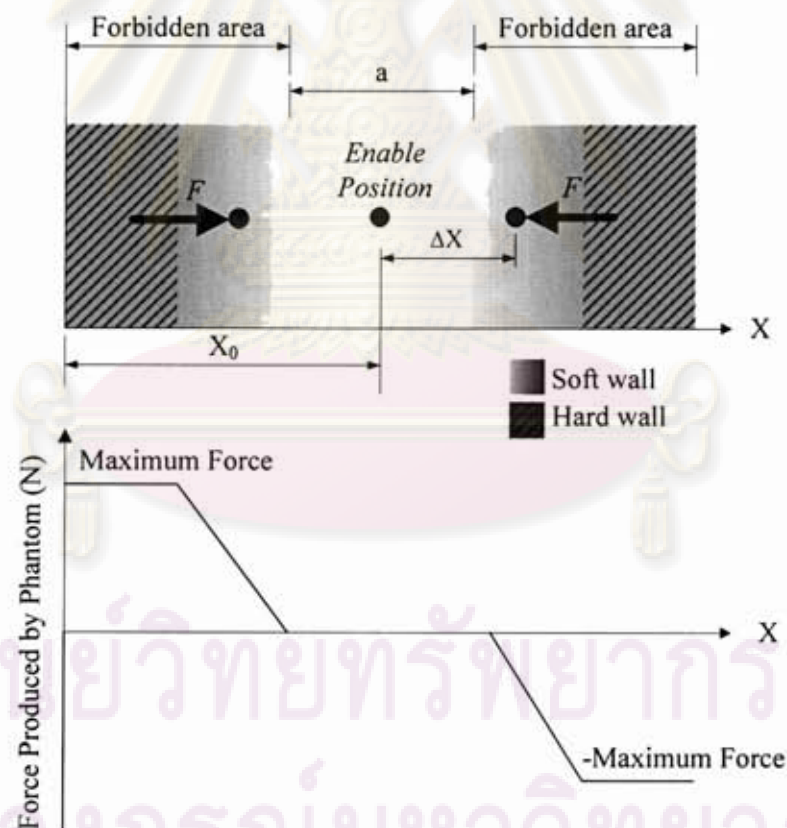
Figure 6.13: Force produced in the forbidden area of the virtual fixture

The pushing force in the soft wall zone relates to the displacement ΔX that the tip penetrates into the wall (see Equation (6.3.1)). The size of this force can be

calculated from Equation (6.3.2). However, it is limited by the maximum force F_{max} of the Phantom which is shown in Figure 6.13.

$$\Delta X = \begin{cases} X - X_0 + a/2 & : \quad X < X_0 - a/2 \\ X - X_0 - a/2 & : \quad X > X_0 + a/2 \end{cases} \quad (6.3.1)$$

$$F = \begin{cases} k(\Delta X) & : \quad X \in \left[X_0 - a/2, X_0 + a/2 \right] \\ F_{max} & : \quad X > \left(X_0 + a/2 + \dfrac{F_{max}}{k} \right) \\ -F_{max} & : \quad X < \left(X_0 - a/2 - \dfrac{F_{max}}{k} \right) \end{cases} \quad (6.3.2)$$

Where

X	= tip coordinate in Cartesian space of the Phantom
X_0	= coordinate of the enable position
ΔX	= displacement of the tip that penetrate into the wall
a	= width of the virtual fixture (distance between 2 walls)
k	= spring constant
F_{max}	= maximum force produced by the Phantom

Please note that these equations are implemented on all three axes (X, Y, and Z). Hence the virtual square box is constructed. In brief, although this shape is easy to constructed, the major weakness point of this shape is singularities that are occurred at the corner of the hard wall. However, it is not a major problem because the preferred movement is only inside the soft wall zone.
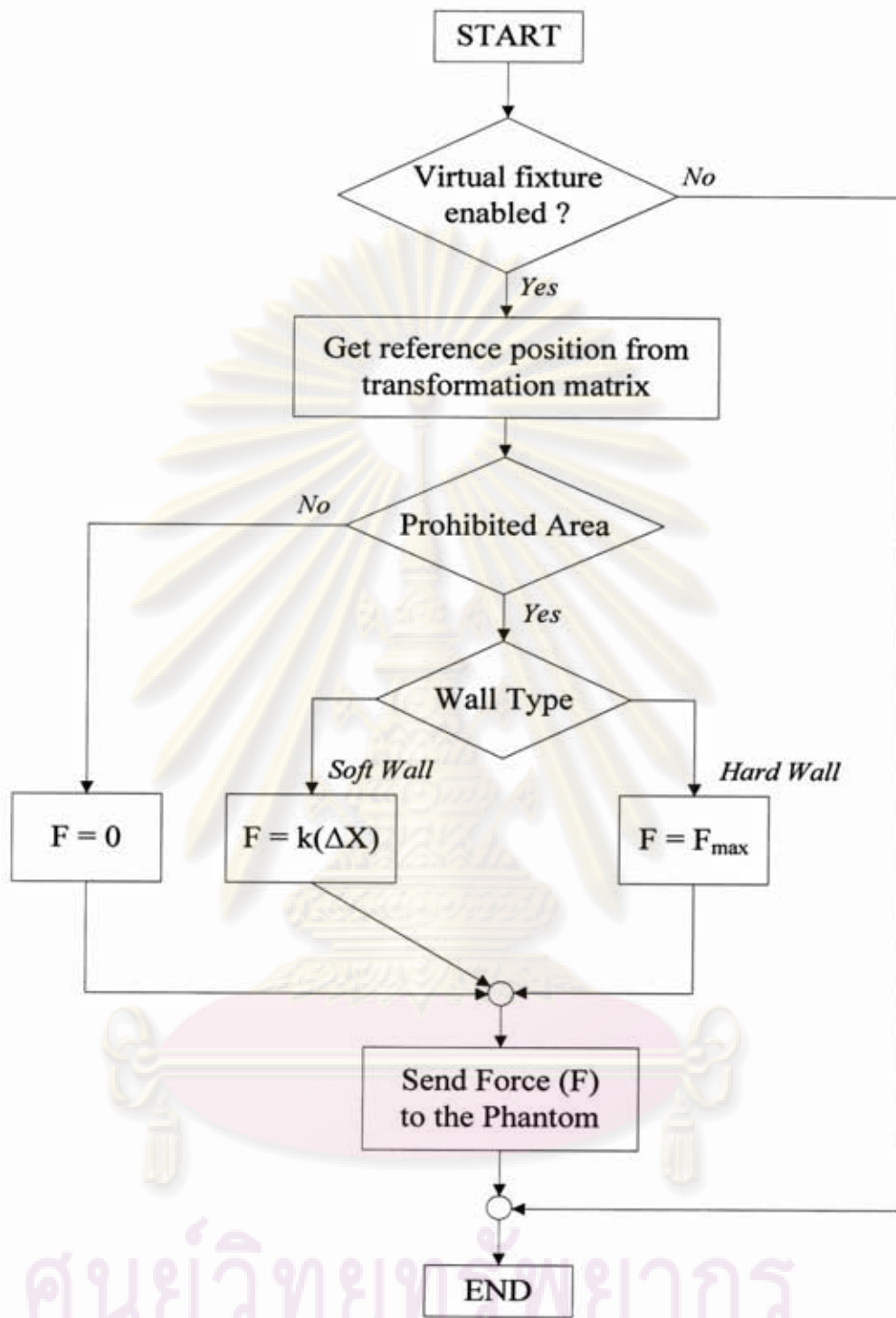
Figure 6.14: A procedure of using a virtual fixture flowchart

6.4 User interface software

The typical user interface software consists of two individual parts, including the master-slave control console and the Real-time image console.

6.4.1 The master-slave control console

Control buttons and the useful information about the states of both the Phantom and the RCRT-1 Manipulator are shown in this console (see Figure 6.15). This information is very useful in order to interpret an overall operation of the system.
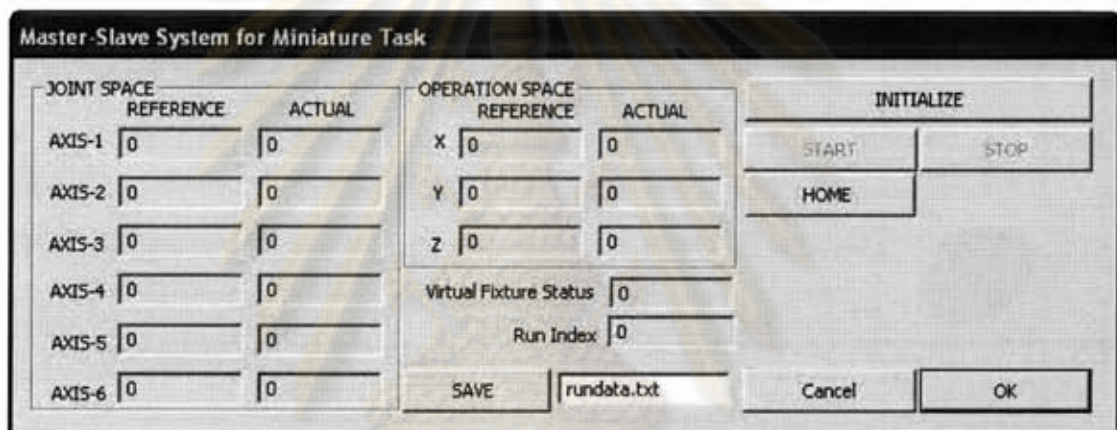
Figure 6.15: The master-slave control console

1) The slave manipulator reference & actual angles (joint space)

2) The slave manipulator reference & actual positions (Cartesian space)

3) Virtual fixture status (enable/disable)

4) Time index (duration since the operation has been start)

5) Initialize (connect to the interface cards and the Phantom)

6) Start & stop operation button

7) Set home button (move the slave manipulator to home position)

8) Save data

9) OK & Cancel button (terminate this console window)

6.4.2 Real-time image console

This console shows the real-time movie captured from a digital microscope that is attached on the s platform of the RCRT-1 Manipulator. The Dino-Lite Digital Microscope [26] has been selected for this experiment because of its high magnification (20X – 230X) and convenience computer interface. This camera connects to a computer via USB. The console displays real time image from the "DinoCapture", the original software of Dino Lite. Moreover, measurement module is available in this software. The size of the measured objects can be computed from the magnification at that time

(a)   (b)
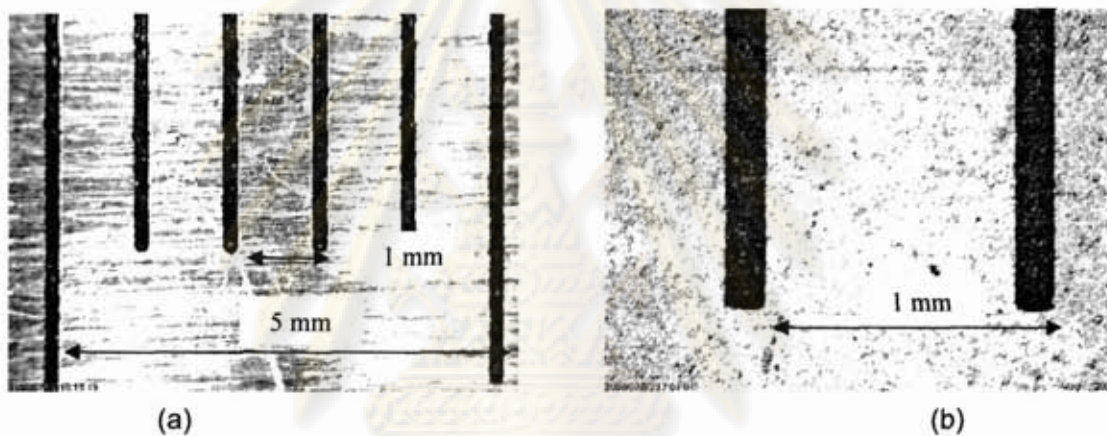
Figure 6.16: Images of a standard ruler captured by the Dino Lite Plus
at different magnification: 61.2X (left) 200.0X (right)

CHAPTER VII

EXPERIMENTS AND DISCUSSIONS

This chapter describes the testing methods and results of this robotic system. The experiment can be categorized into four sections, including *accuracy test, precision test, master-slave operation test,* and *real tasks operation test*. Moreover, the results of each experiment is discussed and concluded.

7.1 Data acquisition and average error

The experiments of this robotic system are designed based on two major operation modes, consisted of "a slave independent operation mode" and "a master-slave mode". The actual and the reference data, position and orientation of both robots in Cartesian space, are compared in each experiment. Consequently, the errors between actual data and reference data will be considered in order to determine performance of this system.

The raw data that typically required from in these experiments are reference and actual joint angles. The reference joint angles are created with respect to the desired movements of each experiment, while the actual joint angles are obtained from the encoder. The details of the data acquisition are described in the following topic.

7.1.1 Data acquisition of both robots

The data acquired in each servo-loop are from both robots. The Phantom transmits the data through the HDAPI. Meanwhile, the RCRT-1 Manipulator sends the data through the I/O card in the PC. Overall, the raw data that are acquired from this robotic system are listed as follows:

- Joint angles (from incremental encoder)
- Reference voltage signal (for calculating the computed torque)
- Phantom's positions and orientations (in Cartesian space)

7.1.1.1 Actual position and orientation

As regard to the slave manipulator, the actual position and orientation of the end-effector can be obtained from the forward kinematics equations. Data of joint angles are required in order to obtain states of the end-effector in the Cartesian space.

Data of joint angles are acquired from the encoders and I/O cards in the computer. Meanwhile, the joint angular velocities are calculated from the joint angles by differentiation.

7.1.1.2 The computed torque

Even though the computed torque cannot be measured straightforwardly from the system, reference voltage signal is used to calculate the value of this torque. The reference voltage signal is sent to the power amplifier. Afterwards, the amplifier produces the current linearly related to this reference signal in order to drive the motor. Next, the torque produced by the motor is also linearly related to the current. In conclusion, this process shows that the torque and the reference signal are linearly related. The procedure is clearly shown as a diagram in Figure 7.1.
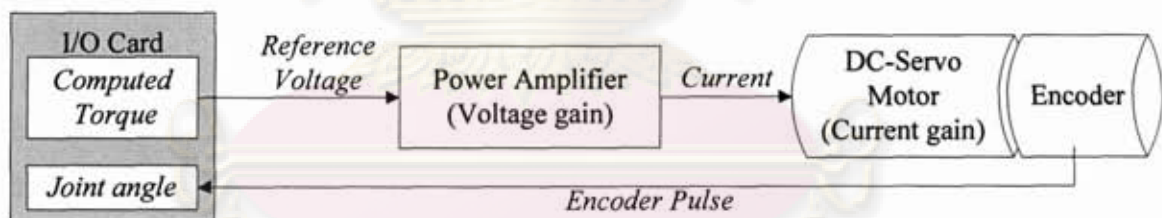
Figure 7.1: Data acquisition from the I/O Card and signal transfer

7.1.1.3 Information from the Phantom

The Phantom provides the positions and orientations of its end-effector in the Cartesian space. These data is in the form of the transformation matrix, which is obtained from the HDAPI. Moreover, the Phantom also provides other usefully data, including velocity of the end-effector and output forces.

7.1.2 Average error

The position error in this test is determined from the absolute distance between the actual position and the reference position (see Figure 7.2). This absolute error is calculated from Equation (7.1). Moreover, the *quadratic mean (RMS)* is used in order to determine the average errors, for position error and orientation error. Consequently, the average error clearly represents the performance of the controller in order to control the motion of the RCRT-1 Manipulator. Moreover, other statistic data, including standard deviation (S.D.), maximum error, and minimum error, are presented in each experiment.
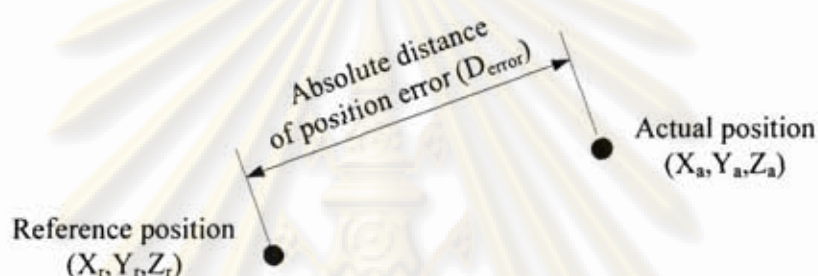
Figure 7.2: Absolute distance of position error

$$D_{error} = \sqrt{\left(X_a - X_r\right)^2 + \left(Y_a - Y_r\right)^2 + \left(Z_a - Z_r\right)^2} \qquad (7.1)$$

Where

D_{error} = absolute distance between the actual and reference position

$\left(X_a, Y_a, Z_a\right)$ = coordinate of actual position in Cartesian space

$\left(X_r, Y_r, Z_r\right)$ = coordinate of reference position in Cartesian space

7.2 Accuracy test

Because the RCRT-1 Manipulator is designed to be typically used in the master-slave operation, the users can compensate the error automatically by their hand. Thereby, the importance of accuracy for this master-slave system is not much. However, the maximum position error with respect to the test was less than 2.0 mm. Detail of the accuracy test is clearly explained in Appendix E.

7.3 Precision test (the slave independent operation test)

The test was done by moving the end-effector of the slave manipulator from the initial point (at the home position) to the reference final points with trajectory control (see Appendix A). The reference final points are selected with respect to the major working area. The main purposes are to determine *precision* and *repeatability* of the slave manipulator. Precision and repeatability are determined from the position error in the Cartesian space at steady state. The position errors are computed from joint angles and forward kinematics.

Moreover the PID controller with gravity compensation was implemented. In conclusion, the errors notified in this section are occurred due to the controller. The typical procedure of the test is:

1) Determine the reference final point in Cartesian space.
2) Compute the reference joint angles from inverse kinematics.
3) Compute trajectory of the reference path for each joint.
4) Move the manipulator from the initial position to this location for 10 times.
5) Collect data of the joint angles during the movement.
6) Move back to the initial position.
7) Compute the position from the collected joint angles by the forward kinematics.
8) Compare the actual motion trajectories to the desired ones and calculate errors.
9) Repeat the test for other reference points.

Six reference final points were selected in this test. Because the tracking-ability and steady state error are on focused, the trajectories are designed with respect to the joint space. The trajectory partially improves the overall error because the joint angle and position changes gradually.

Each movement path typically represented ability of the manipulator to move up and down. The massive errors were occurred typically in vertical movement. Moreover, the reference final points are selected based on the in the typical working area which is below an XY-plane. These six reference points represented in Figure 7.3. All of the six joints were moved synchronously along the movement path. These points can be

represented as the transformation matrices. They are shown in Equation (7.3.1) to (7.3.6)

$$
{}_{T}^{0}\mathbf{T}_{1} = \begin{bmatrix} -0.497 & 0.686 & -0.532 & 210.932 \\ -0.220 & 0.493 & 0.842 & 261.747 \\ 0.840 & 0.535 & -0.094 & 123.561 \\ 0 & 0 & 0 & 1 \end{bmatrix} \tag{7.3.1}
$$

$$
{}_{T}^{0}\mathbf{T}_{2} = \begin{bmatrix} -0.257 & 0.783 & -0.567 & 244.205 \\ 0.020 & 0.590 & 0.807 & 295.019 \\ 0.966 & 0.196 & -0.167 & -6.197 \\ 0 & 0 & 0 & 1 \end{bmatrix} \tag{7.3.2}
$$

$$
{}_{T}^{0}\mathbf{T}_{3} = \begin{bmatrix} 0.063 & 0.733 & 0.677 & 350.581 \\ 0.949 & -0.254 & 0.186 & -181.046 \\ 0.309 & 0.631 & -0.712 & -163.141 \\ 0 & 0 & 0 & 1 \end{bmatrix} \tag{7.3.3}
$$

$$
{}_{T}^{0}\mathbf{T}_{4} = \begin{bmatrix} 0.177 & 0.880 & 0.441 & 248.503 \\ 0.884 & -0.340 & 0.323 & -122.112 \\ 0.434 & 0.332 & -0.838 & -255.965 \\ 0 & 0 & 0 & 1 \end{bmatrix} \tag{7.3.4}
$$

$$
{}_{T}^{0}\mathbf{T}_{5} = \begin{bmatrix} 0.619 & 0.422 & 0.662 & 181.432 \\ -0.342 & -0.614 & 0.711 & -130.617 \\ 0.707 & -0.667 & -0.236 & -311.018 \\ 0 & 0 & 0 & 1 \end{bmatrix} \tag{7.3.5}
$$

$$
{}_{T}^{0}\mathbf{T}_{6} = \begin{bmatrix} -0.677 & 0.734 & -0.059 & 263.174 \\ 0.595 & 0.593 & 0.543 & 173.306 \\ 0.434 & 0.332 & -0.838 & -388.104 \\ 0 & 0 & 0 & 1 \end{bmatrix} \tag{7.3.6}
$$

Note: the last axis angle is represented by θ_6 which is coupled with θ_5. For convenience, $\theta_6^{\cdot}$ that is obtained directly from the motor is presented in the test results.

The selected final points for precision test
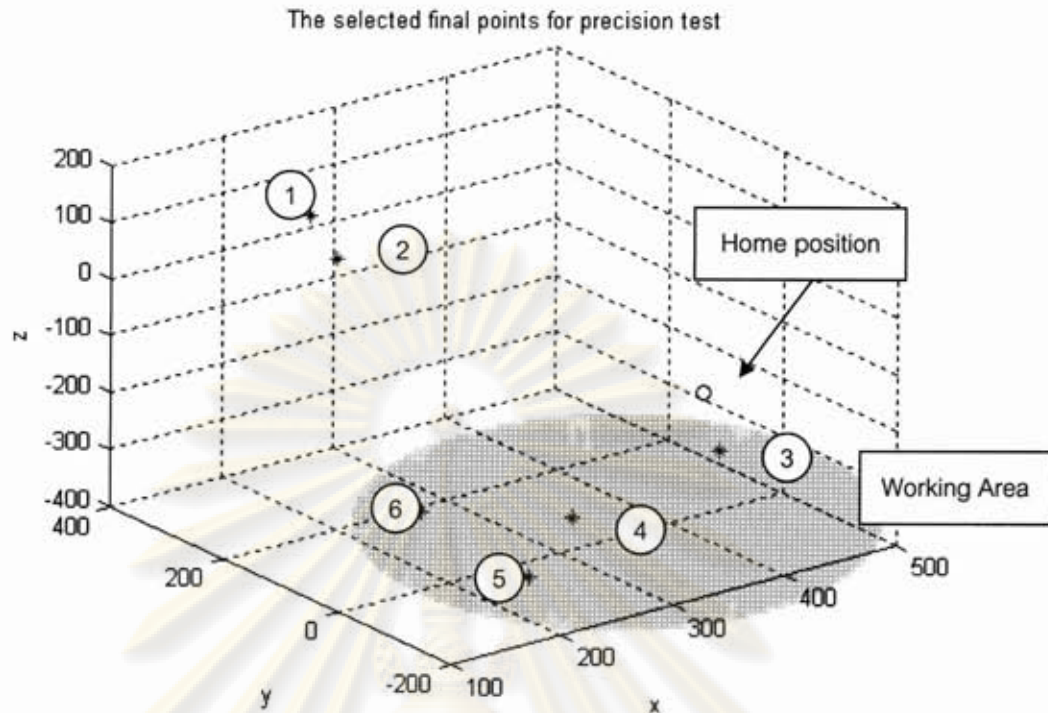
Figure 7.3: Reference points including the initial and
the final points for the precision test

The reference joint angles, with respect to position of the reference final points,
are shown in Equation (7.3.7) to (7.3.13)

$$\boldsymbol{\theta}_{final} = \begin{bmatrix} \theta_1 & \theta_2 & d_3 & \theta_4 & \theta_5 & \theta_6^{\bullet} \end{bmatrix} \qquad (7.3.7)$$

$$\boldsymbol{\theta}_{final1} = \begin{bmatrix} 45.000° & 68.715° & 350\text{mm} & 85.944° & 88.868° & 80.214° \end{bmatrix} \qquad (7.3.8)$$

$$\boldsymbol{\theta}_{final2} = \begin{bmatrix} 45.000° & 90.000° & 375\text{mm} & 85.944° & 88.868° & 80.214° \end{bmatrix} \qquad (7.3.9)$$

$$\boldsymbol{\theta}_{final3} = \begin{bmatrix} -30.000° & 110.000° & 400\text{mm} & 45.000° & 45.000° & 45.000° \end{bmatrix} (7.3.10)$$

$$\boldsymbol{\theta}_{final4} = \begin{bmatrix} -30.000° & 130° & 350\text{mm} & 45.000° & 45.000° & 45.000° \end{bmatrix} \qquad (7.3.11)$$

$$\boldsymbol{\theta}_{final5} = \begin{bmatrix} -45.000° & 143.715° & 375\text{mm} & 85.944° & 88.868° & 80.214° \end{bmatrix} (7.3.12)$$

$$\boldsymbol{\theta}_{final6} = \begin{bmatrix} 30.000° & 130° & 400\text{mm} & 45.000° & 45.000° & 45.000° \end{bmatrix} \qquad (7.3.13)$$

7.3.1 Test result of point No.1

Table 7.1: Position errors of point No.1

No.	Joint angle (rad)						Position Error (mm)
	θ_1	θ_2	d_3 (mm)	θ_4	θ_5	$\theta_6^{\bullet}$	
1	0.78529	1.19911	350.00022	1.39945	1.40044	1.40020	0.090
2	0.78528	1.19890	350.00072	1.39914	1.40040	1.40036	0.152
3	0.78522	1.19895	350.00022	1.39938	1.39996	1.40044	0.151
4	0.78536	1.19916	349.99972	1.39938	1.40040	1.40040	0.065
5	0.78533	1.19918	349.99922	1.39919	1.40040	1.40056	0.056
6	0.78529	1.19925	349.99922	1.39960	1.40028	1.40012	0.053
7	0.78529	1.19923	349.99972	1.39966	1.40036	1.40044	0.060
8	0.78536	1.19906	349.99972	1.39890	1.40024	1.40028	0.083
9	0.78533	1.19913	349.99922	1.39893	1.39992	1.40032	0.065
10	0.78526	1.19901	349.99872	1.39962	1.40036	1.40020	0.132
average	0.78530	1.19910	349.99967	1.39933	1.40028	1.40033	(RMS) 0.098
S.D.	0.00004	0.00012	0.00060	0.00028	0.00019	0.00013	0.039

Table 7.1 shows the data of joint angles and the position errors in the steady state (time = 0.15 second) at the final reference point No.1. The test of this final reference point was repeated for 10 times. Consequently, each position error was computed from the forward kinematics. In summary, the position error was in the range of 0.053 mm to 0.132 mm. The rms was 0.098 mm and S.D was 0.039 mm. The slave manipulator was controlled to move up according to the desired trajectory and path.

Figure 7.4(a) illustrates the movement paths of both end-effectors in the Cartesian space. They moved from the initial position (point-i) to the final position (point-f). According to Figure 7.4(b), the overall error reached the peak at about 0.08 seconds after the manipulator started moving. Then it dramatically decreased to 0.091 mm at the steady state. However the error in X-direction had the greatest effect to the overall error.

Figure 7.4: (a) Movement paths and (b) error in Cartesian space
of the end-effector in Cartesian space (point No.1)

The displacement of the end-effectors in each direction is clearly shown in Figure 7.5. Small gap between the reference and actual paths in the X and Y direction can be notified. Moreover, only little error in the Z-direction was occurred. It can be concluded that the gravity compensator was able to reduce the gravity effect excellently.

Figure 7.5: Displacement of the end-effector in each direction (point No.1)

7.32 Test result of point No.2

Table 7.2: Position errors of point No.2

No.	Joint angle (rad)						Position error (mm)
	θ_1	θ_2	d_3 (mm)	θ_4	θ_5	$\theta_6^{\cdot}$	
1	0.78531	1.57176	400.00115	1.39919	1.40020	1.40032	0.421
2	0.78519	1.57184	399.99965	1.39927	1.40036	1.40036	0.458
3	0.78533	1.57181	400.00065	1.39925	1.40028	1.40036	0.439
4	0.78540	1.57186	399.99965	1.39945	1.40032	1.40024	0.451
5	0.78528	1.57183	400.00015	1.39951	1.40020	1.40040	0.439
6	0.78522	1.57163	400.00165	1.39923	1.40022	1.40036	0.373
7	0.78533	1.57179	400.00065	1.39943	1.40012	1.40040	0.424
8	0.78536	1.57179	400.00165	1.39925	1.40044	1.40040	0.430
9	0.78526	1.57181	400.00015	1.39879	1.40040	1.39992	0.459
10	0.78533	1.57174	399.99965	1.39906	1.40036	1.40036	0.418
average	0.78530	1.57179	400.00050	1.39924	1.40029	1.40031	(RMS)0.432
S.D.	0.00006	0.00007	0.00078	0.00021	0.00010	0.00015	0.025

Table 7.2 shows the data of joint angles and the position errors in the steady state (time = 0.15 second) at the final reference point No.2. The test of this final reference point was repeated for 10 times. Consequently, each position error was computed from the forward kinematics. In summary, the position error was in the range of 0.373 mm to 0.458 mm. The rms was 0.431 mm and S.D was 0.025 mm. The slave manipulator was controlled to move up according to the desired trajectory and path.

Figure 7.6(a) illustrates the movement paths of both end-effectors in the Cartesian space. They moved from the initial position (point-i) to the final position (point-f). According to Figure 7.6(b), the overall error was 1.521 mm at the beginning and converged to just under 0.432 mm in about 0.12 seconds. It stood at this value at the steady state. However the error in Z-direction had the greatest effect to the overall error.

The path of end-effector in Cartesian space(mm)

Error in Cartesian space

Figure 7.6: (a) Movement paths and (b) error in Cartesian space
of the end-effector in Cartesian space (final point No.2)

The displacement of the end-effectors in each direction is shown in Figure 7.7.
The very small errors can be notified in each direction. In summary, these graphs show
that the slave manipulator was able to track the reference paths effectively.

Displacement in each direction
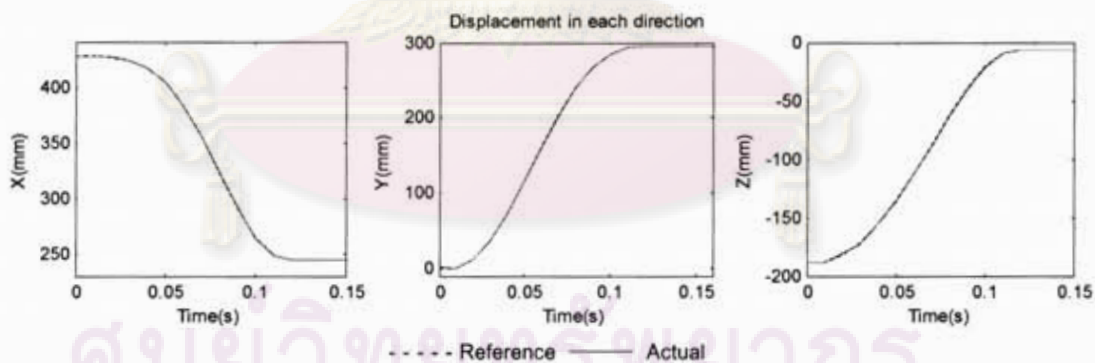
Figure 7.7: Displacement of the end-effector in each direction (point No.2)

7.3.3 Test result of point No.3

Table 7.3: Position errors of point No.3

No.	Joint angle (rad)						Position error (mm)
	θ_1	θ_2	d_3 (mm)	θ_4	θ_5	$\theta_6^{\cdot}$	
1	-0.52308	1.92094	399.99965	0.78490	0.78544	0.78568	0.514
2	-0.52328	1.92056	399.99965	0.78485	0.78576	0.78540	0.341
3	-0.52334	1.92058	400.00015	0.78455	0.78568	0.78548	0.343
4	-0.52323	1.92058	399.99965	0.78420	0.78568	0.78556	0.361
5	-0.52328	1.92067	399.99965	0.78446	0.78531	0.78564	0.379
6	-0.52332	1.92063	400.00015	0.78468	0.78525	0.78580	0.354
7	-0.52321	1.92068	399.99965	0.78481	0.78568	0.78532	0.398
8	-0.52328	1.92061	400.00015	0.78468	0.78552	0.78532	0.357
9	-0.5233	1.92073	399.99965	0.78459	0.78532	0.78568	0.400
10	-0.52328	1.92068	399.99965	0.78483	0.78570	0.78512	0.388
average	-0.52326	1.92067	399.99980	0.78466	0.78553	0.78550	(RMS) 0.387
S.D.	0.00007	0.00011	0.00024	0.00021	0.00019	0.00021	0.051

Table 7.3 shows the data of joint angles and the position errors in the steady state (time = 0.15 second) at the final reference point No.3. The test of this final reference point was repeated for 10 times. Consequently, each position error was computed from the forward kinematics. In summary, the position error was in the range of 0.341 mm to 0.514 mm. The rms was about 0.384 mm and S.D was 0.051 mm. The slave manipulator was controlled to move down according to the desired trajectory and path.

Figure 7.8(a) illustrates the movement paths of both end-effectors in the Cartesian space. They moved from the initial position (point-i) to the final position (point-f). According to Figure 7.8(b), the overall error was 1.524 mm at the beginning and converged to 0.432 mm in about 0.12 seconds. It stood at this value at the steady state. However the error in Z-direction had the greatest effect to the overall error.

The path of end-effector in Cartesian space(mm)
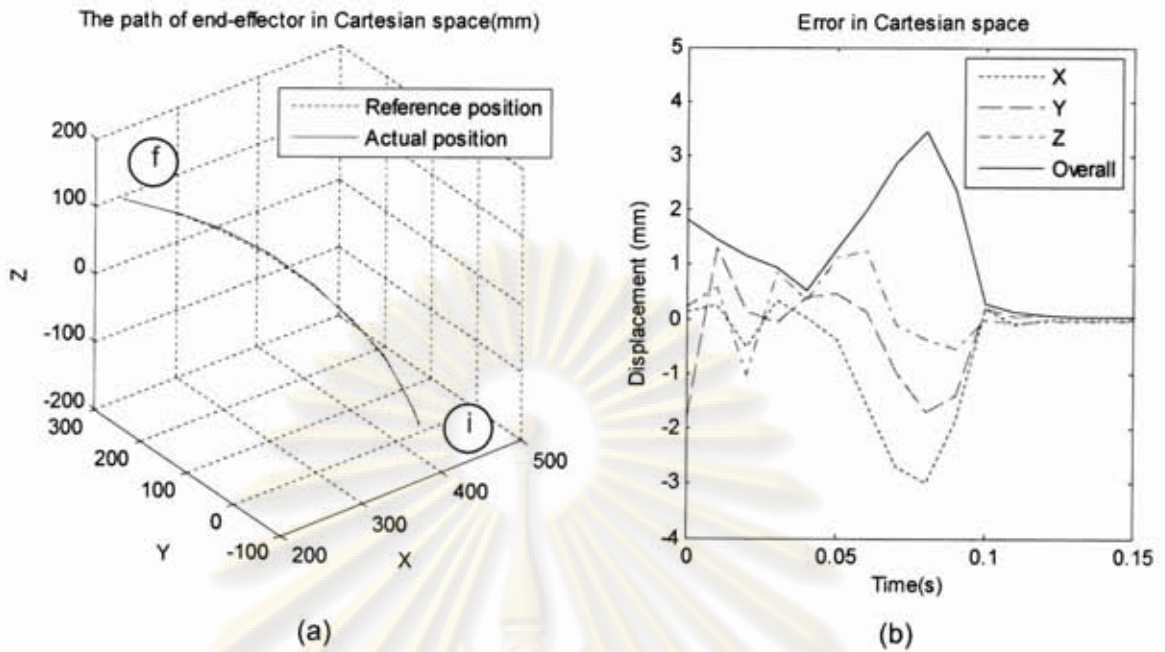
Error in Cartesian space

Figure 7.8: (a) Movement pathss and (b) error in Cartesian space
of the end-effector in Cartesian space (point No.3)

The displacement of the end-effectors in each direction is clearly shown in Figure 7.9. Only small gaps between the reference and actual paths in the X and Y direction can be notified. On the contrary, considerable error in the Z-direction was occurred. The error caused by time delay is occurred during the path. The error remained constant at about 0.332 mm since 0.07 seconds after the test was started.
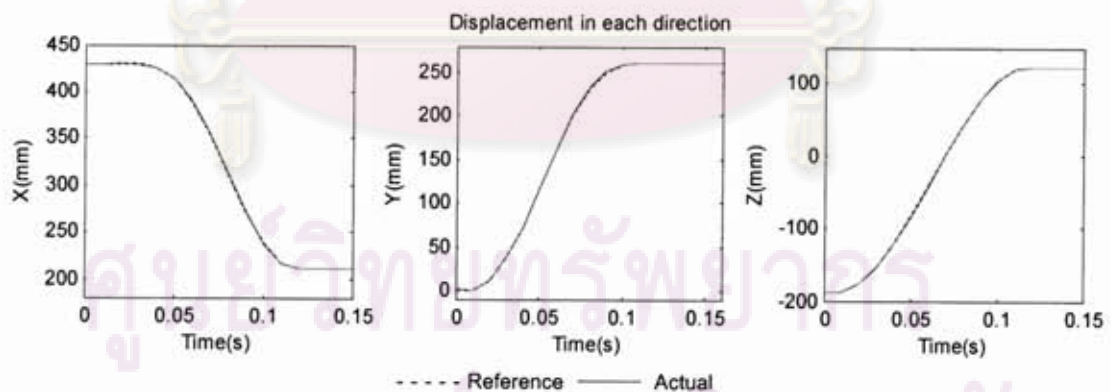

Displacement in each direction
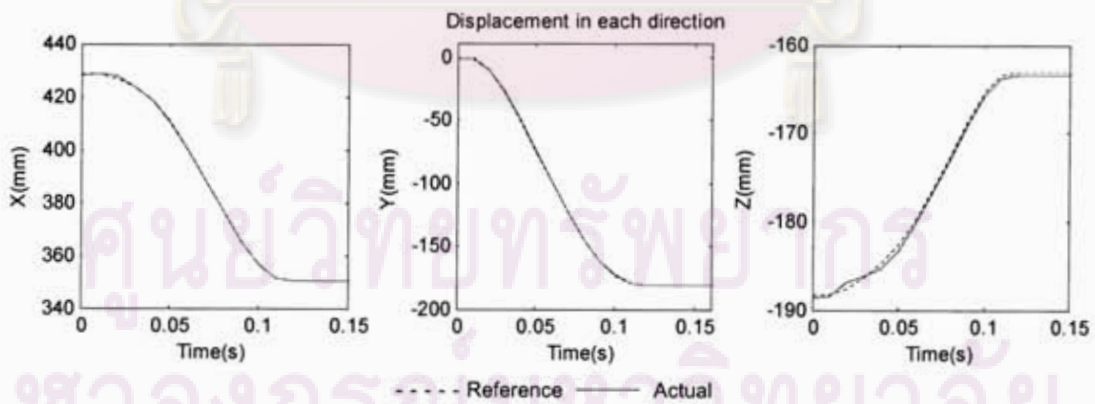
Figure 7.9: Displacement of the end-effector in each direction (point No.3)

7.3.4 Test result of point No.4

Table 7.4: Position errors of point No.4

No.	Joint angle (rad)						Position error (mm)
	θ_1	θ_2	d_3 (mm)	θ_4	θ_5	$\theta_6^{\bullet}$	
1	-0.52339	2.26872	350.00072	0.78451	0.78540	0.78552	0.073
2	-0.52323	2.26856	350.00022	0.78451	0.78548	0.78532	0.146
3	-0.52341	2.26856	349.99972	0.78503	0.78556	0.78568	0.136
4	-0.52323	2.26846	350.00022	0.78481	0.78564	0.78568	0.184
5	-0.52334	2.26865	350.00122	0.78433	0.78512	0.78552	0.010
6	-0.52330	2.26854	350.00072	0.78470	0.78568	0.78560	0.146
7	-0.52323	2.26865	350.00022	0.78466	0.78552	0.78544	0.124
8	-0.52320	2.26858	350.00022	0.78457	0.78580	0.78576	0.146
9	-0.52341	2.26856	349.99972	0.78503	0.78568	0.78568	0.135
10	-0.52323	2.26846	350.00022	0.78481	0.78560	0.78568	0.184
average	-0.52330	2.26857	350.00032	0.78470	0.78555	0.78559	(RMS) 0.138
S.D.	0.00008	0.00008	0.00046	0.00023	0.00019	0.00014	0.034

Table 7.4 shows the data of joint angles and the position errors in the steady state (time = 0.15 second) at the final reference point No.4. The test of this final reference point was repeated for 10 times. Consequently, each position error was computed from the forward kinematics. In summary, the position error was in the range of 0.073 mm to 0.184 mm. The rms was 0.384 mm and S.D was 0.034 mm. The slave manipulator was controlled to move down according to the desired trajectory and path.

Figure 7.10(a) illustrates the movement pathss of both end-effectors in the Cartesian space. They moved from the initial position (point-i) to the final position (point-f). According to Figure 7.10(b), the overall error reached the peak at about 0.08 seconds after the manipulator started moving. Then it dramatically decreased to 0.128 mm at the steady state. However the error in X-direction had the greatest effect to the overall error.

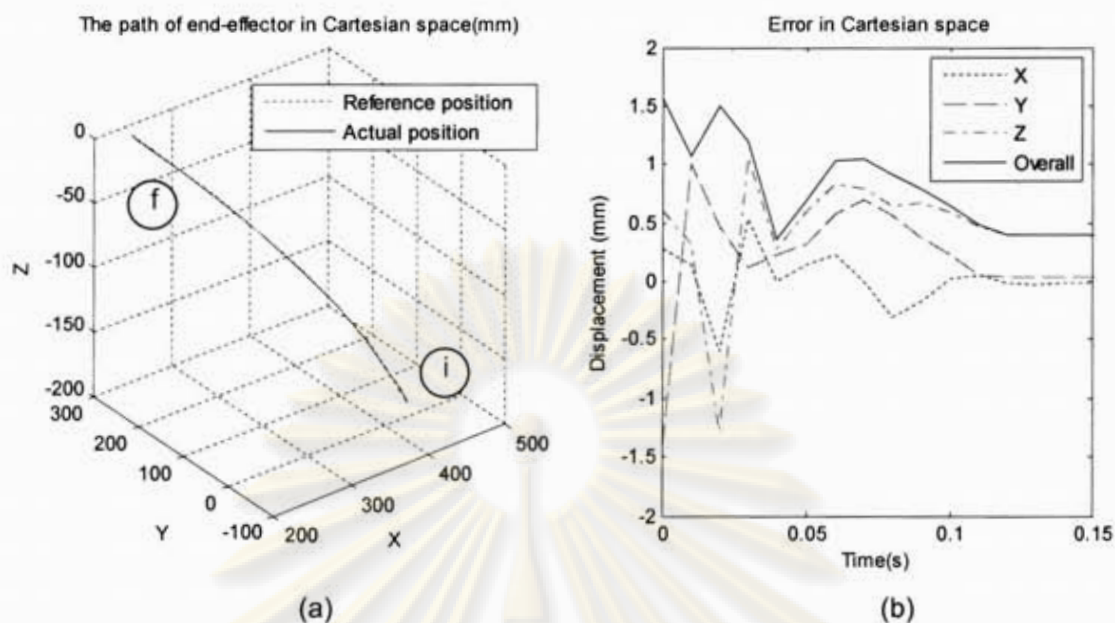The path of end-effector in Cartesian space(mm)

Error in Cartesian space

Figure 7.10: (a) Movement pathss and (b) error in Cartesian space

of the end-effector in Cartesian space (point No.4)

The displacement of the end-effectors in each direction is clearly shown in Figure 7.11. The gaps between the reference and actual paths in all direction can be notified. The errors were occurred in every direction because the 3rd joint cannot move fast enough. Some errors can be notified until 0.1 second had passed. The response of the 3rd joint is shown in Appendix E.

Displacement in each direction
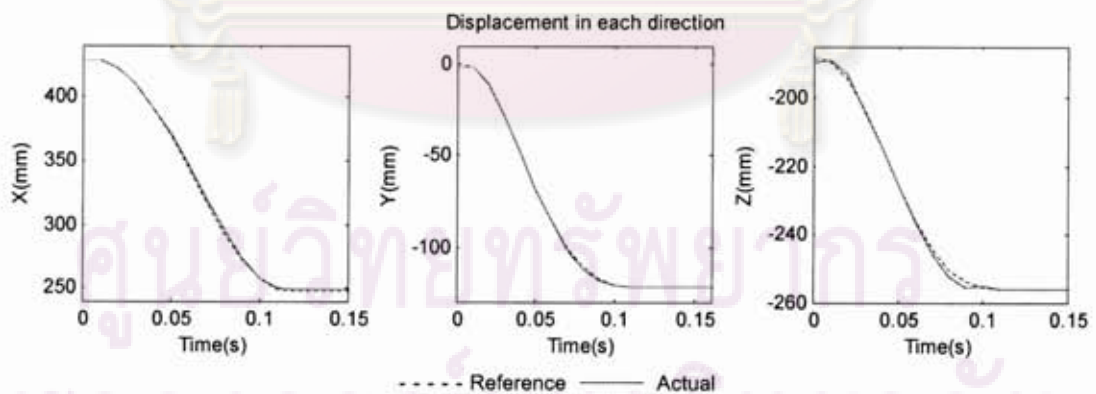
Figure 7.11: Displacement of the end-effector in each direction (point No.4)

7.3.5 Test result of point No.5

Table 7.5: Position errors of point No.5

No.	Joint angle (rad)						Position error (mm)
	θ_1	θ_2	d_3 (mm)	θ_4	θ_5	$\theta_6^\bullet$	
1	-0.78529	2.50786	375.00044	1.39925	1.40040	1.40008	0.177
2	-0.78521	2.50790	375.00044	1.39951	1.40036	1.40034	0.173
3	-0.78529	2.50800	375.00044	1.39923	1.40044	1.40008	0.123
4	-0.78522	2.50788	375.00044	1.39945	1.40040	1.40028	0.177
5	-0.78521	2.50799	374.99994	1.39945	1.40022	1.40036	0.138
6	-0.78526	2.50799	374.99994	1.39919	1.40030	1.40022	0.128
7	-0.78524	2.50799	374.99944	1.39914	1.40050	1.39996	0.128
8	-0.78522	2.50800	375.00044	1.39890	1.40028	1.40036	0.112
9	-0.78521	2.50795	375.00094	1.39893	1.40034	1.40050	0.133
10	-0.78508	2.50807	375.00044	1.39962	1.40020	1.40028	0.123
average	-0.78522	2.50796	375.00029	1.399267	1.40034	1.40025	(RMS) 0.143
S.D.	0.00006	0.00007	0.00041	0.00024	0.00010	0.00016	0.025

Table 7.5 shows the data of joint angles and the position errors in the steady state (time = 0.15 second) at the final reference point No.5. The test of this final reference point was repeated for 10 times. Consequently, each position error was computed from the forward kinematics. In summary, the position error was in the range of 0.112 mm to 0.177 mm. The rms was 0.143 mm and S.D was 0.025 mm. The slave manipulator was controlled to move down according to the desired trajectory and path.

Figure 7.12(a) illustrates the movement pathss of both end-effectors in the Cartesian space. They moved from the initial position (point-i) to the final position (point-f). According to Figure 7.12(b), the overall error reached the peak at about 0.02 seconds after the manipulator started moving. Consequently, it dramatically decreased to 0.142 mm at the steady state. However the error in X and Z-direction greatly affected the overall error.

The path of end-effector in Cartesian space(mm)
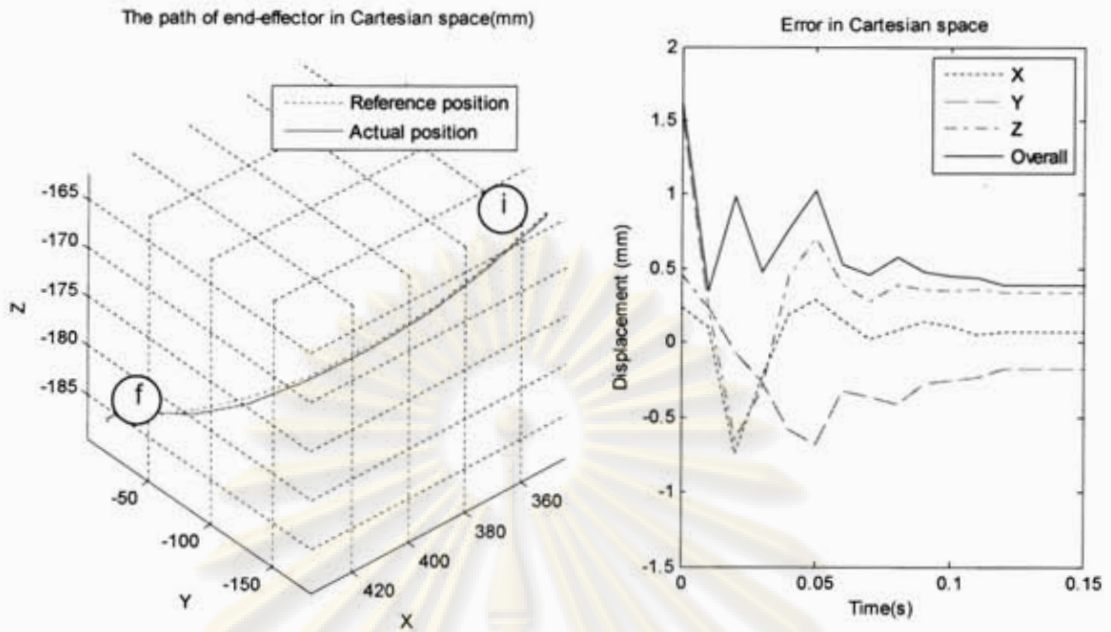
Error in Cartesian space
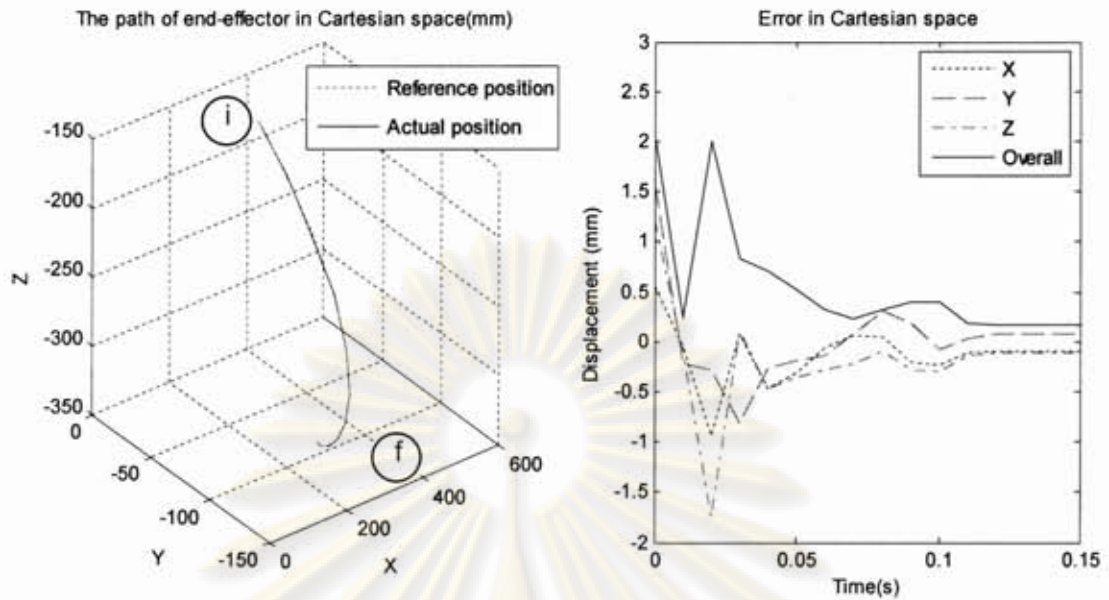
Figure 7.12 (a) Movement pathss and (b) error in Cartesian space
of the end-effector in Cartesian space (point No.5)

The displacement of the end-effectors in each direction is clearly shown in Figure 7.13. Only small gaps between the reference and actual paths in all direction can be notified. The slave manipulator tracked the path very well. Moreover, the steady state errors converged to almost zero.

Displacement in each direction
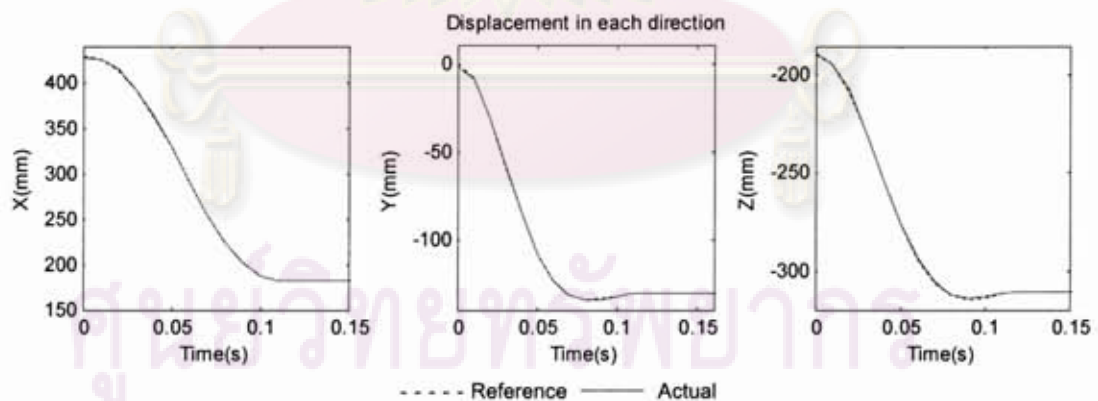
Figure 7.13: Displacement of the end-effector in each direction (point No.5)

7.3.6 Test result of point No.6

Table 7.6: Position errors of point No.6

No.	Joint angle (rad)						Position error (mm)
	θ_1	θ_2	d_3 (mm)	θ_4	θ_5	θ_6^*	
1	0.52344	2.26882	400.00015	0.78457	0.7858	0.78528	0.064
2	0.52344	2.26895	399.99965	0.78503	0.78568	0.78568	0.054
3	0.52348	2.26874	399.99965	0.78468	0.78568	0.78544	0.081
4	0.52346	2.26877	399.99965	0.78433	0.78540	0.78516	0.081
5	0.52355	2.26872	399.99915	0.78470	0.78548	0.78516	0.081
6	0.52355	2.26877	399.99965	0.78446	0.78556	0.78568	0.057
7	0.52346	2.26893	399.99965	0.78459	0.78552	0.78536	0.059
8	0.52348	2.26867	400.00015	0.78455	0.78568	0.78564	0.105
9	0.52353	2.26874	399.99965	0.78451	0.78576	0.78552	0.069
10	0.52353	2.26868	399.99965	0.78451	0.78552	0.78560	0.095
average	0.52349	2.26878	399.9997	0.78459	0.78561	0.78545	(RMS) 0.076
S.D.	0.00004	0.00009	0.00028	0.00019	0.00013	0.00021	0.017

Table 7.6 shows the data of joint angles and the position errors in the steady state (time = 0.15 second) at the final reference point No.6. The test of this final reference point was repeated for 10 times. Consequently, each position error was computed from the forward kinematics. In summary, the position error was in the range of 0.054 mm to 0.105 mm. The rms was 0.076 mm and S.D was 0.017 mm. The slave manipulator was controlled to move down according to the desired trajectory and path.

Figure 7.14(a) illustrates the movement pathss of both end-effectors in the Cartesian space. They moved from the initial position (point-i) to the final position (point-f). According to Figure 7.14(b), the overall error reached the peak at about 0.02 seconds after the manipulator started moving. Consequently, it gradually decreased to 0.075 mm at the steady state.
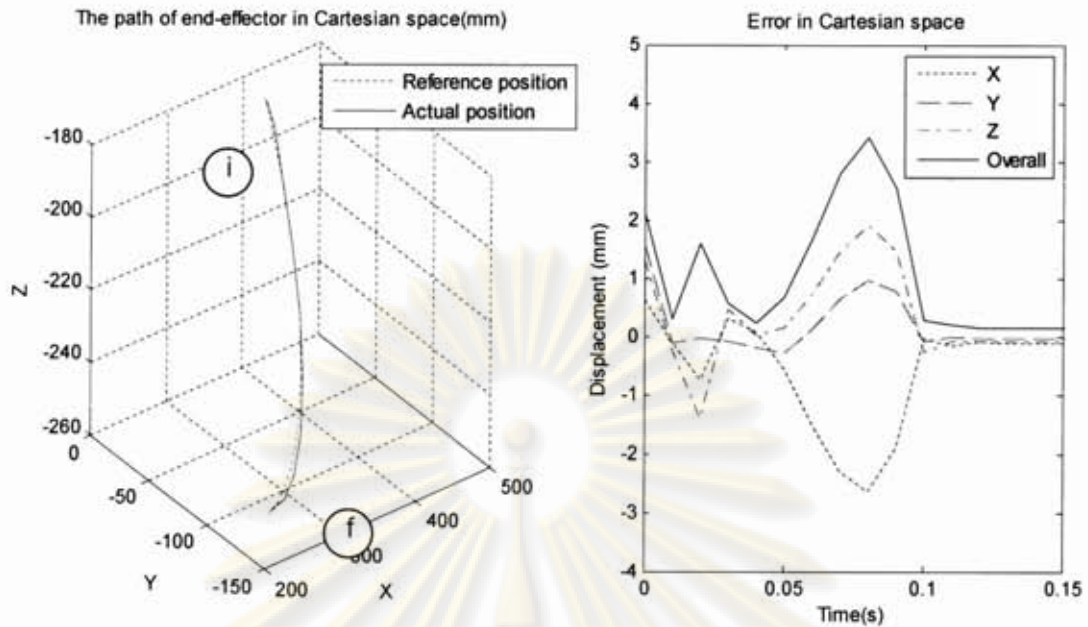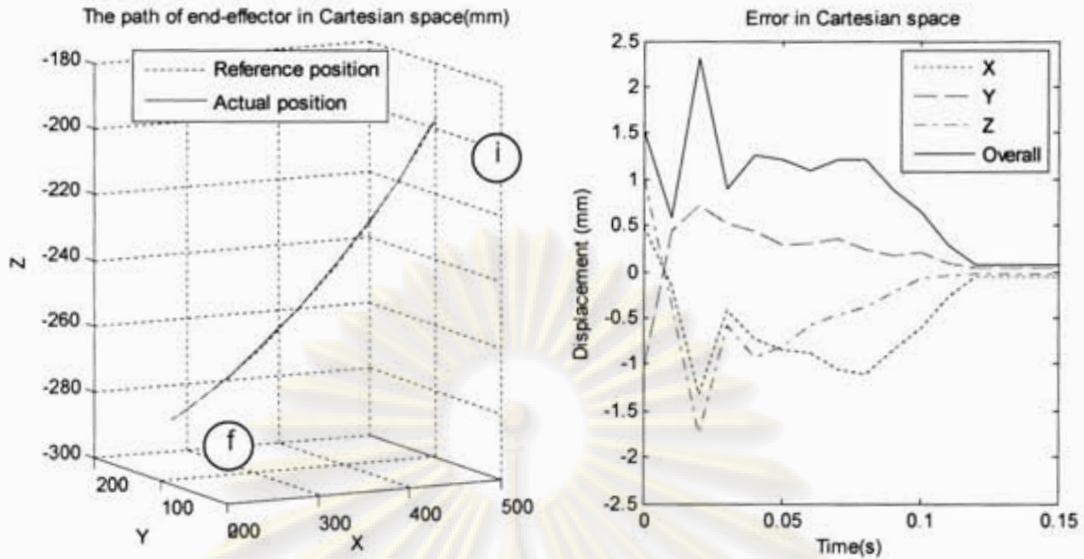
Figure 7.14: (a) Movement pathss and (b) error in Cartesian space
of the end-effector in Cartesian space (point No.6)

The displacement of the end-effector in each direction is shown in Figure 7.15. The response in X and Y direction tracked the reference signal very well. Furthermore, very small error in Z-direction can be notified. However, the steady state error of each joint was almost zero.
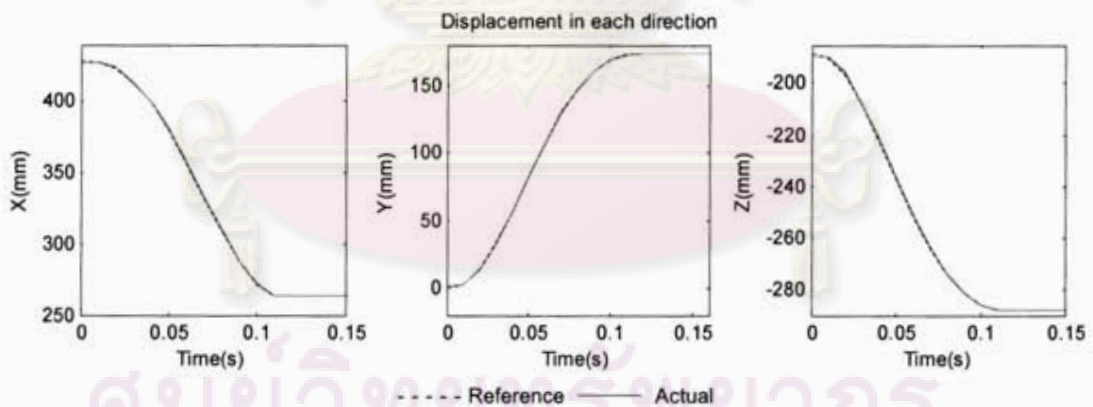
Figure 7.15: Displacement of the end-effector in each direction (point No.6)

7.3.7 Test result summary

Table 7.7: Summary of the precision test

Point No.	Position error in Cartesian space (mm)			
	Average(RMS)	S.D.	Maximum	Minimum
1	0.098	0.039	0.152	0.053
2	0.432	0.025	0.459	0.373
3	0.387	0.050	0.514	0.341
4	0.138	0.033	0.184	0.073
5	0.143	0.025	0.177	0.112
6	0.076	0.017	0.105	0.054

The maximum RMS of the position error was 0.432 mm (with S.D. = 0.025 mm). This value was occurred in the test for the point No.2. On the other hand, the minimum RMS of the position error was about 0.076 mm (with S.D. = 0.017 mm). This minimum value is occurred in the test for the point No.6. Consequently, the data at point No.2 was used in order to determine the precision and repeatability of the RCRT-1 Manipulator.

The precision is determined from the maximum error which was 0.514 mm. The repeatability is determined from 95% probability that the results are expected to lie in. Therefore, it is equal to two times of S.D. which is 0.050 mm.

7.4 The master- slave operation test

In this section, the Phantom was used in order to provide the reference position and orientation of the RCRT-1 Manipulator. Two motion modes, were *coarse motion* (G_M =1) and *fine motion* (G_M = 0.1), were applied in this test.

The main objective of this section is to determine *tracking-ability* of the slave manipulator. Furthermore, the effectiveness of the virtual fixture is examined. The test is done in order to prove how well the virtual wall can limit the boundary of slave manipulator's movements.

In this test, the user moved the Phantom freely inside the desired region. The slave manipulator was moved with respect to these reference paths of the Phantom. Moreover, this region was bounded by the virtual walls. Theoretically, the end-effectors

cannot move through the walls because the counter forces are generated. Furthermore, the PID controller with gravity compensation was used in order to control the movements. The typical procedure of the tests is:

1) Select the motion mode by selecting the motion amplifier gain G_M.

2) Select the desired point and enable the virtual wall.

3) Operate the master-slave system and collect data.

4) Calculate the positions and orientations of the RCRT-Manipulator from its joint space data and forward kinematics.

5) Compare the position and the orientation of the RCRT-Manipulator with respect to the Phantom. Consequently, errors in the Cartesian space are calculated.

7.4.1 Test results of the coarse motion (G_M =1)

The coarse motion gain was set to the system. Afterwards, the end-effector of the slave manipulator was moved randomly during about 40 seconds. This movement path is created with respect to the Phantom. The RCRT-1 Manipulator moved inside the bounded region which was a 30mm $\times$ 30mm $\times$ 30mm cube.

The position of random movement path is shown in Figure 7.16. There was little gap between the reference and the actual path during the operation. The path can be obviously seen that it was bounded in a cube. Hence, it represents an effectiveness of the virtual wall. However, some parts of the movement path moved out of the cube. According to the 1mm thickness of the soft-wall, approximately 1mm errors were occurred in every side of the cube.

The path of end-effector in Cartesian space(mm)

Figure 7.16: Position of the end effector in Cartesian space (G_M=1)

Figure 7.17: Position of the end effector in Cartesian space in each plane (G_M=1)
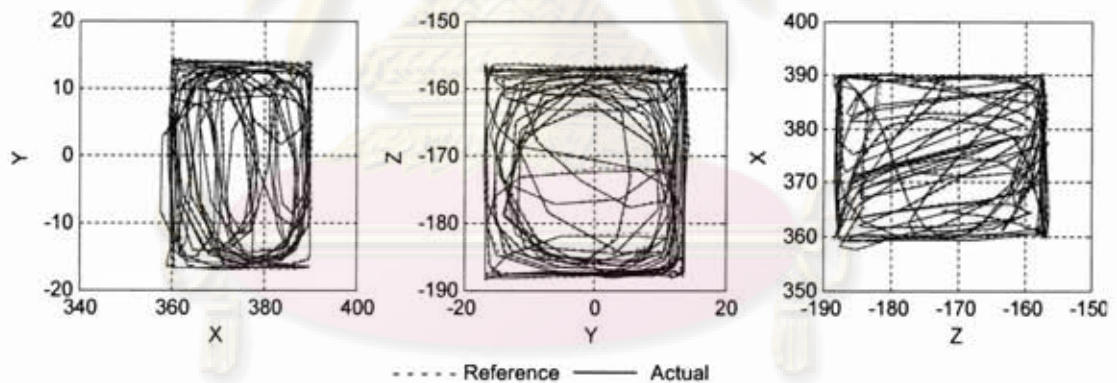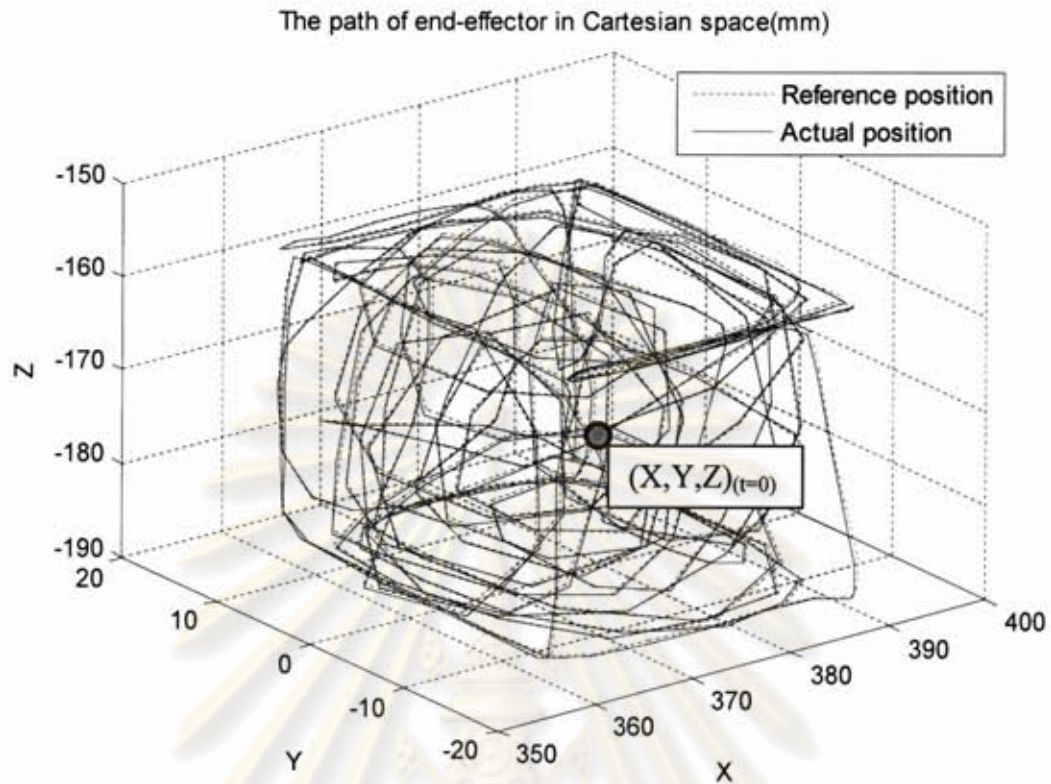
As regard to each plane in Figure 7.17, the path can be bounded very well by the virtual wall. Some of the paths penetrated into the prohibited area, which was the soft-wall region. This error was occurred because the Phantom was moved very fast. Consequently, the force produced from the user movement overcame the counter force. Moreover, some singularities existed at the edges between two walls. This condition leaded to improper forces were produced.

Figure 7.18: Position of the end effector in Cartesian space in each direction (G_M=1)

From Figure 7.18, the absolute position error of the end-effector of the slave manipulator ranged between 0.002 mm and 0.702 mm. RMS of the position error was 0.338 mm.

Each angle of orientation, including roll, pitch, and yaw, was considered individually. The orientation errors are shown in Figure 7.19. The maximum error of roll angle was 0.172 degree. The maximum error of pitch angle was 0.828 degree. The maximum error of yaw angle was 0.537 degree. Overall, the orientation error was less than 0.9 degree. Moreover, the RMS average of each angle is shown in Table 8.7.

Figure 7.19: Orientation error of the end effector in Cartesian space (G_M=1)

Table 7.8: Summary of orientation error (G_M=1)

Error (Degree)	Average(RMS)	Maximum
Roll	0.044	0.172
Pitch	0.092	0.828
Yaw	0.112	0.537

Overall, the slave manipulator was able to track the reference path effectively while using coarse motion gain. The position error during the test was less than 0.7 mm. The orientation error during the test was less than 0.9 degree. However, some of the outstanding errors in both position and orientation can be notified. These errors were caused by the slave manipulator limitation: the 4th joint passed its singularity and the 5th joint reached their limit.

7.4.2 Test results of the fine motion (G_M =0.1)

The fine motion gain was set to the system. Afterwards, the end-effector of the slave manipulator was moved randomly during about 40 seconds. This movement path is created with respect to the Phantom. The RCRT-1 Manipulator moved inside the bounded region which was a 3mm $\times$ 3mm $\times$ 3mm cube.

The position of random movement path is shown in Figure 7.20. The gap between the reference and the actual path can be apparently notified. Even though the path cannot be effectively bounded accurately in the desired cube, the most of movement paths were in the desired region.
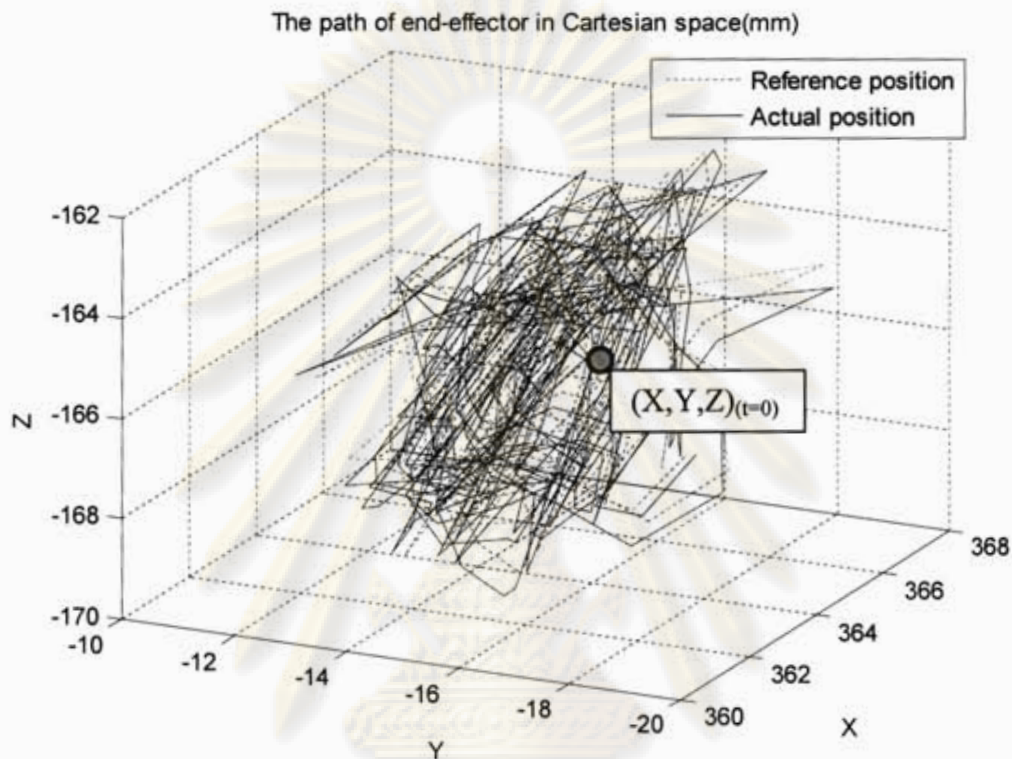
Figure 7.20: Position of the end effector in Cartesian space (G_M=0.1)
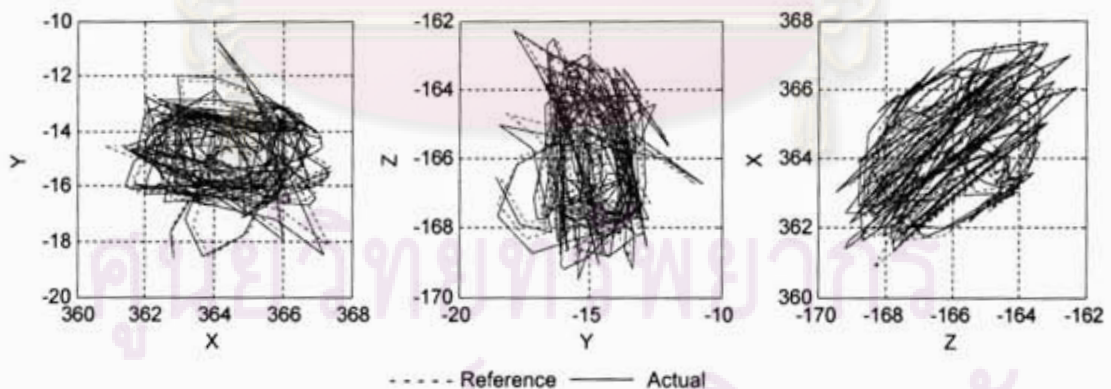
Figure 7.21: Position of the end effector in Cartesian space in each plane (G_M=0.1)

As regard to each plane in Figure 7.21, many parts of the movement path penetrated into the prohibited area, the soft-wall and the hard-wall regions. The soft wall was 1 mm thick. However, most of the movement was still bounded in a 5mm X 5mm X 5mm cube. This clearly shows that the virtual wall allowed the

movement path went into the prohibited region by approximately 1 mm on each side of the wall. However, there are a few parts of the movement that penetrated the hard-wall. This problem occurred because the Phantom was not able to produce a very high force in order to prevent the excess users' movements. However, the problem of singularity and limitation of the Phantom's output force are also occurred in the coarse motion mode.
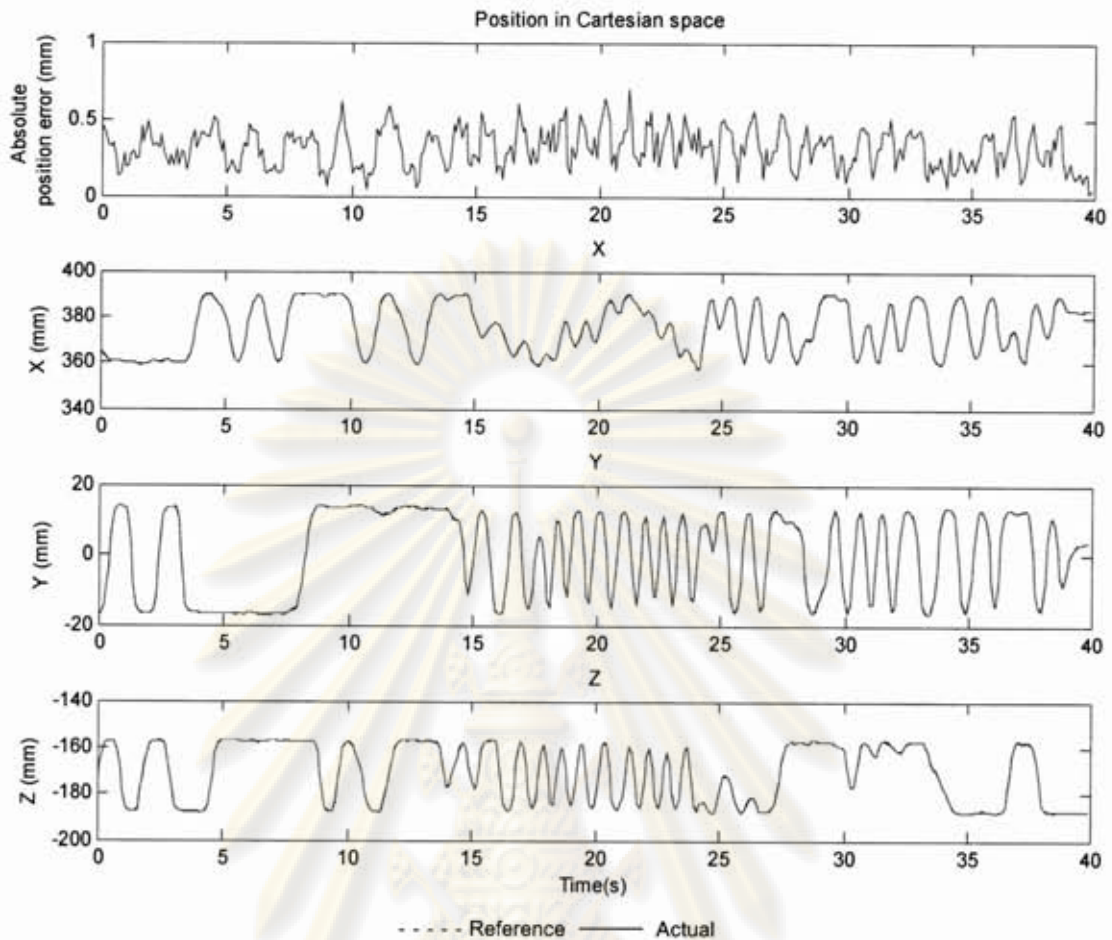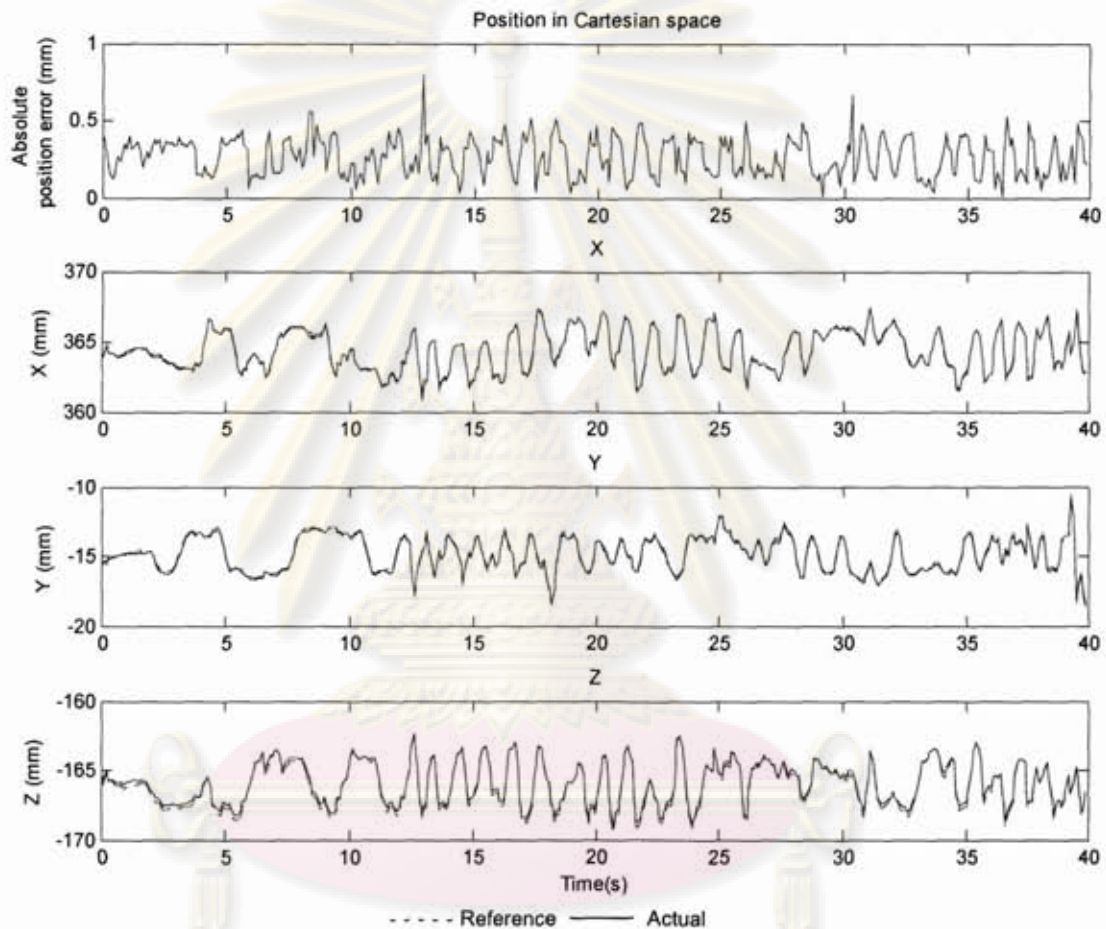

Figure 7.22: Position of the end effector in Cartesian space in each direction (G_M=0.1)

From Figure 7.22, the absolute position error of the end-effector of the slave manipulator ranged between 0.015 mm and 0.266 mm. RMS of the position error was 0.293 mm.

Each angle of orientation, including roll, pitch, and yaw, was considered individually. The orientation errors are shown in Figure 7.23. The maximum error of roll angle was 0.628 degree. The maximum error of pitch angle was 0.832 degree. The maximum error of yaw angle was 0.811 degree. Overall, the orientation error was less than 0.9 degree. Moreover, the RMS average of each angle is shown in Table 7.9.
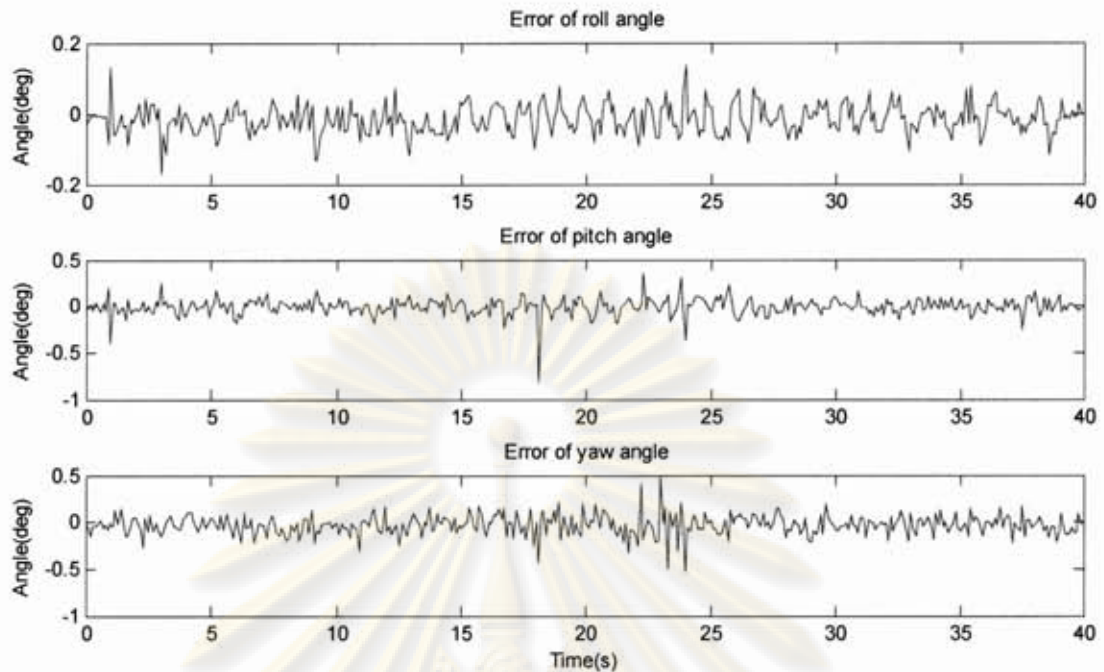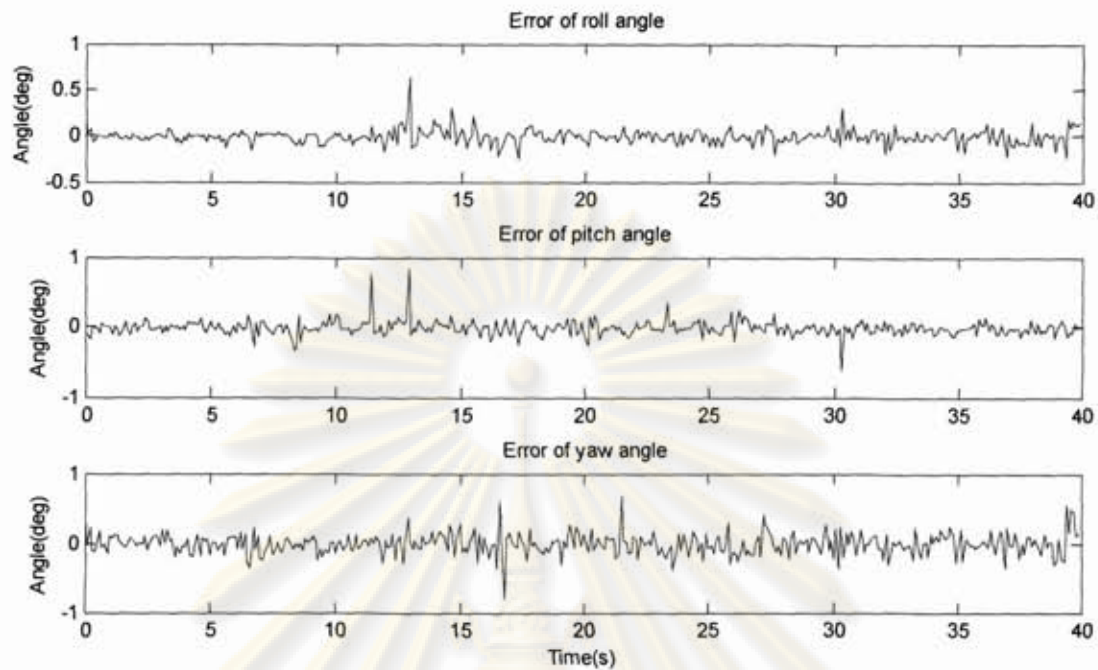
Figure 7.23: Orientation error of the end effector in Cartesian space (G_M=0.1)

Table 7.9: Summary of orientation error (G_M=0.1)

Error (Degree)	Average (RMS)	Maximum
Roll	0.077	0.628
Pitch	0.105	0.832
Yaw	0.153	0.811

Overall, the slave manipulator was able to track the reference path effectively while using fine motion gain. The position error during the test was less than 0.266 mm. The orientation error during the test was less than 0.9 degree. However, some of the considerable errors in both position and orientation can be notified. In addition to the problem described in Topic 7.4.1, the gap of this test can be obviously seen because of the scale of the coordinate. The errors were relatively large due to side of the wall.

7.4.3 Result summary

Little different in errors between two motion modes is presented from the test. The position error was less than 0.8 mm, while the angle error was less than 0.9 degree. Because these errors were measured all the time, the performance of tracking-ability can be determined from these values.

Moreover, there was little difference between position errors of these two modes. The major difference among both modes was the size of the bounded working area. Each bounded area occurred in this test was shown as the movement paths (see Figure 7.24).
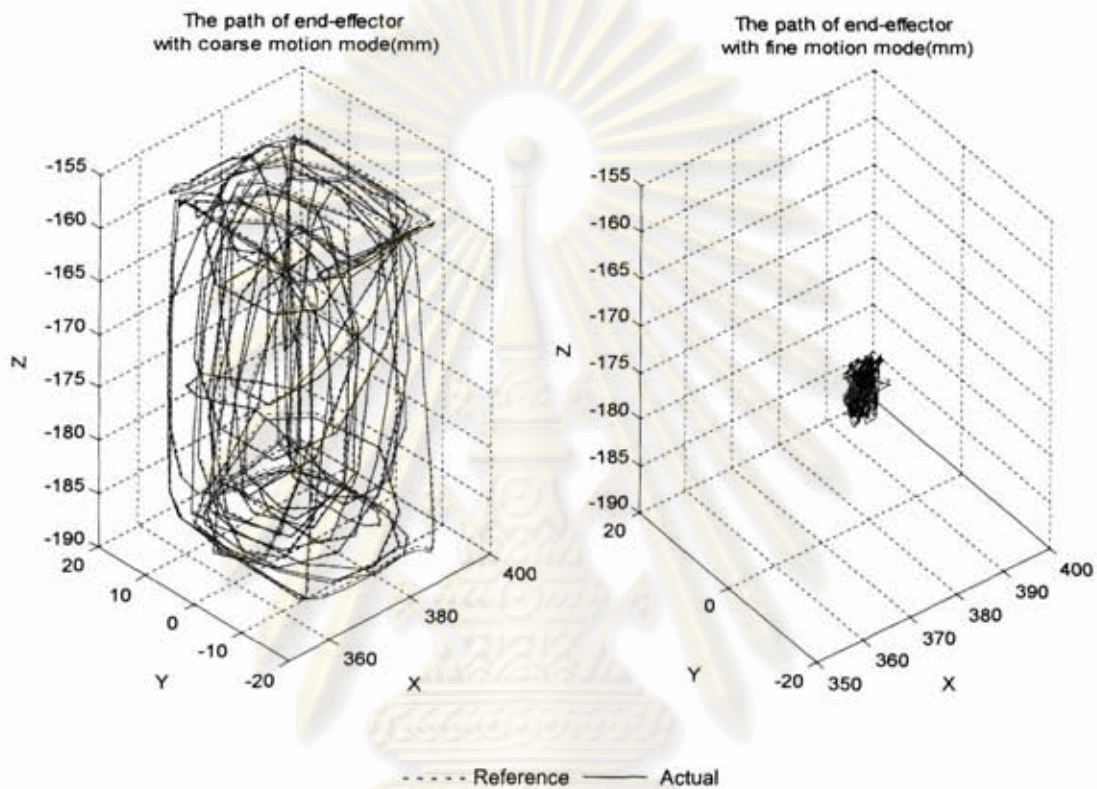
Figure 7.24: The bounded movement paths of two motion mode

7.5 Real task operation test

The main purpose of this test is to determine performance of users' interaction in order to operate this master-slave system. The camera, a digital microscope, was fixed on the platform (base frame {0}) (see Figure 7.25) of the RCRT-1 Manipulator. The real-time images of the operation in the small specific area are captured from this camera.

In the test, users had to control the end-effector of the slave manipulator to move around a large number of fixed points. Only images from the camera can be observed by the users. The electronic PCB board was used as the testing object because it contains a lot of fixed points. Moreover, the points are arranged in the

pattern. On the testing object, each point has about 1 mm in diameter. Furthermore, the distance between each point is approximately 2.5 mm. (see Figure 7.26).
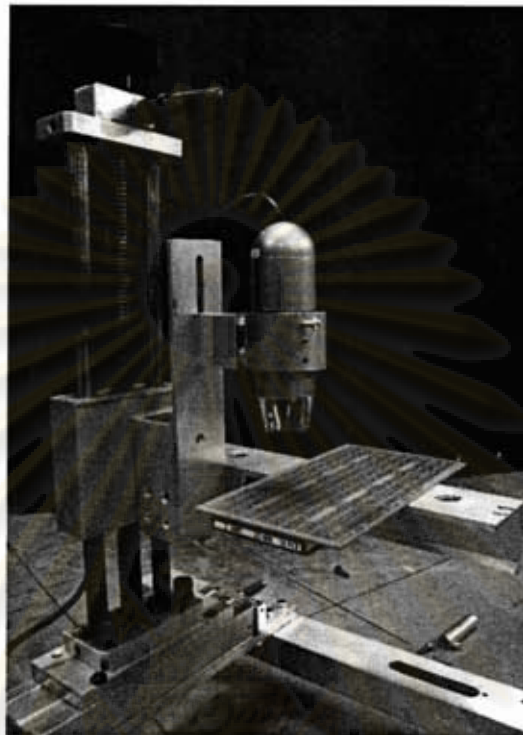
(a)
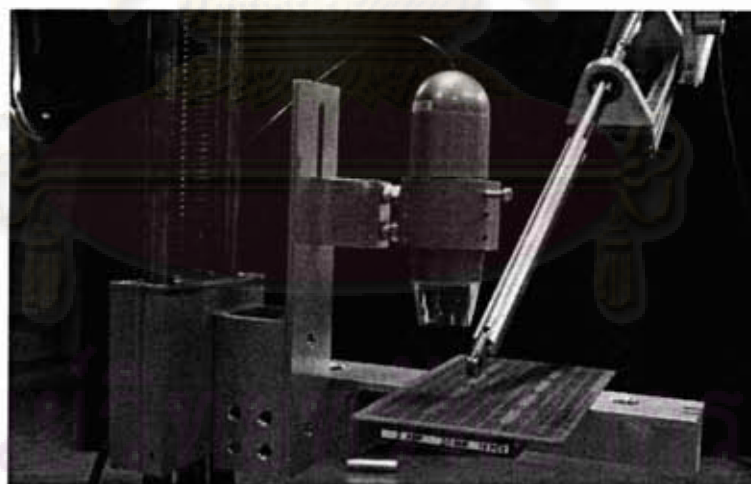
(b)

Figure 7.25: The slave manipulator's platform with the camera

(a) The platform which can be manually translated in 2 directions

(b) The end-effector moved in the working area
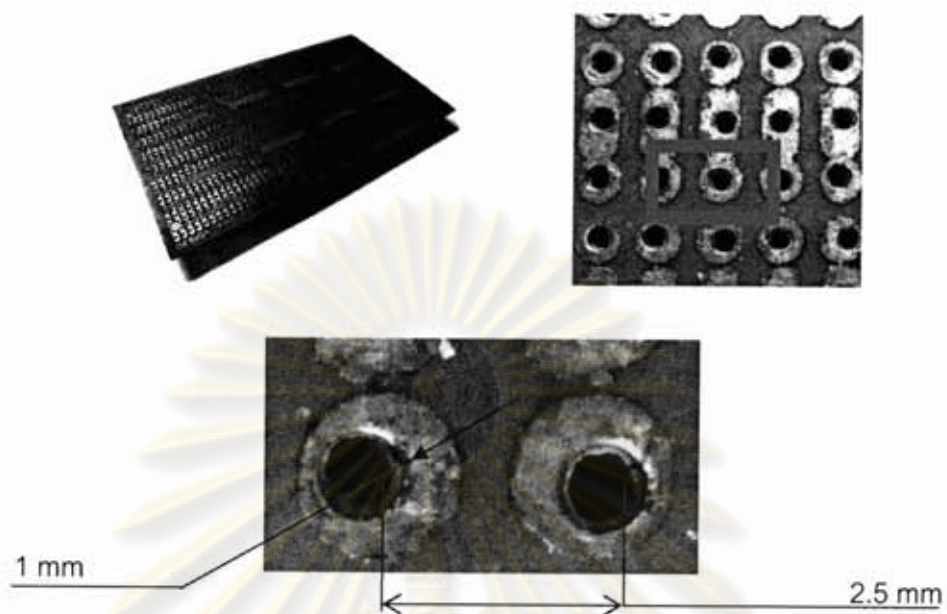
Figure 7.26: The testing object

Inner circle $(1mm\ \phi)$

Center

Outer circle $(2mm\ \phi)$
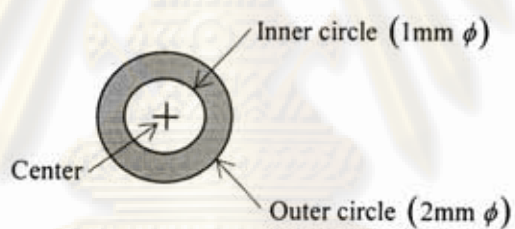
Figure 7.27: The reference point

Figure 7.28: The user was operating through the Phantom on the console
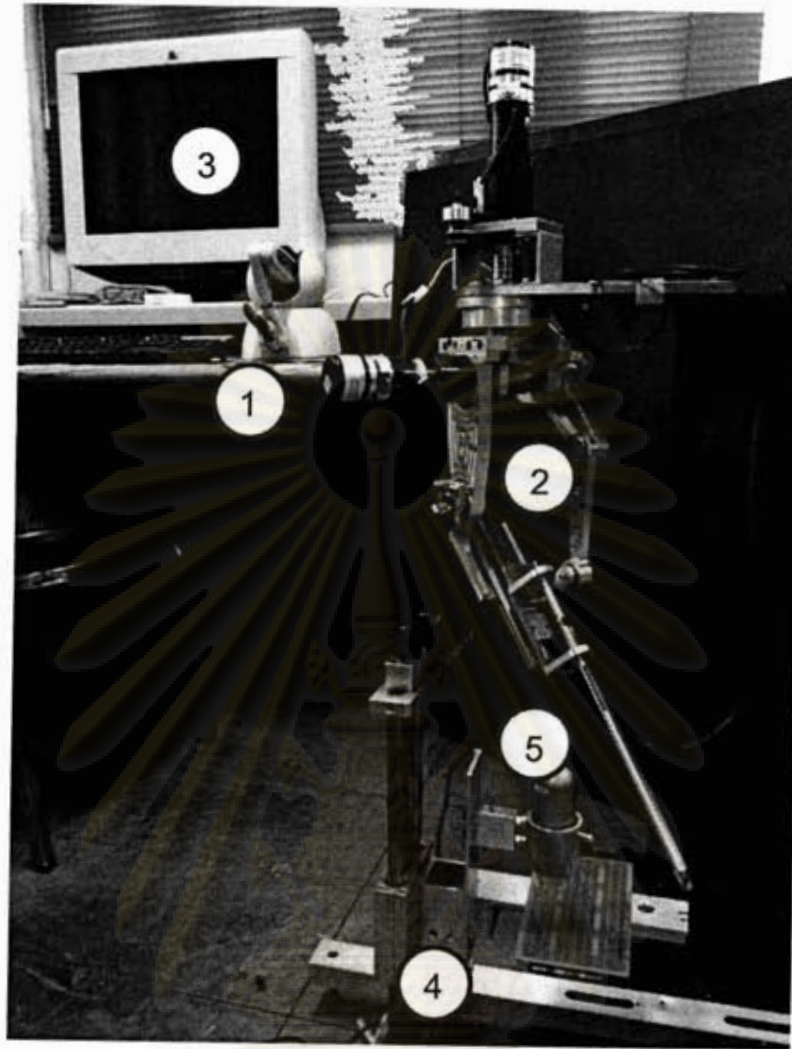
Figure 7.29: The test bed

1) The master device (The Phantom)
2) The slave manipulator
3) The control console
4) Platform
5) Digital microscope

7.5.1 Test results of the real task operation

The testing object
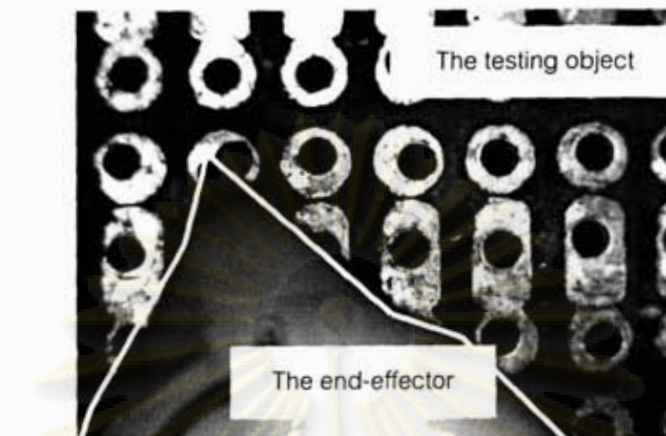
The end-effector

Figure 7.30: Image captured while the end-effector was moving on the test object

The end-effector of the RCRT-1 Manipulator was controlled to move point-to-point on the testing object (see Figure 7.2). The 24 reference points are located on the testing object in the pattern. The user attempted to move the end-effector and stop at the center of each point. Afterwards, the end-effector was controlled to move continuously along the path shown in Figure 7.31. The test was done in approximately 45 seconds.
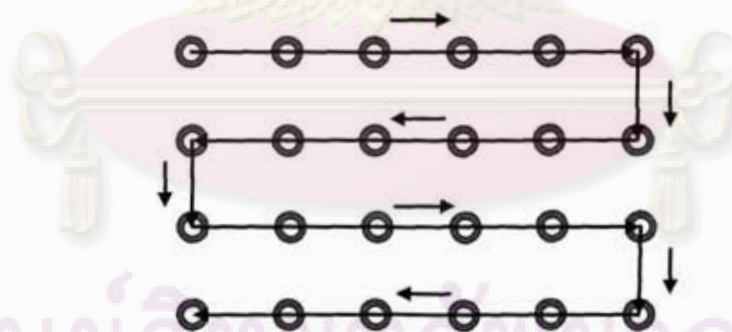
Figure 7.31: The movement path of the end effector on the testing object

According to the test, the user was able to control the end-effector precisely. The end-effector was controlled to point steadily inside the inner circle of the reference points. However, some jittering was occurred due to the movement of user's hand. Moreover, little error caused by time-delay can be notified.

7.6 Conclusion and discussion of the overall results

7.6.1 Accuracy

According to the error, compared between actual position and desired position in the accuracy test, the maximum error was less than 2.0 mm. This error is related to many inaccurate parameters, such as the parameters in kinematics equations. Overall, this little error shows that the manipulator can be control to move to the proper position with medium accuracy. However, the calibration process is necessary in order to improve accuracy of the manipulator.

7.6.2 Precision

Precision of the RCRT-1 Manipulator is determined from the maximum error which was 0.514 mm (with respect to the error from the kinematic calculation). The precision is related to a lot of uncertainties, including frictions, backlash, load handling etc. According to the motion controller, the PID-controller is able to reduce the error from these uncertainties very well. According to the gravity effect, it can be effectively reduced by the gravity compensator.

In brief, the RCRT-1 Manipulator can be moved precisely with respect to this appropriate controller. The overall precision of this manipulator is less than 1 mm which can be acceptable.

7.6.3 Repeatability

Repeatability represents the value which absolute difference between two repeated test results may be expected to lie with a probability of 95%. Therefore, the repeatability of this system is 0.050 mm (with respect to the error from the kinematic calculation). However, the repeatability can be improved by eliminating the uncertainties. In practice, mechanical uncertainties, e.g. gear backlash, tendon extension, and friction, should be removed.

7.6.4 Comparison between coarse and fine motion mode

The average position error occurred in the coarse motion mode was 0.388 mm. Meanwhile, the average position error occurred in the fine motion mode was 0.293 mm. The maximum position error of both modes was less than 0.8 mm. Moreover, as regard to the orientation error in both motion modes, the maximum error in each angle was less than 0.9 degree.

Overall, very little difference between these two motion modes can be notified. Therefore, the performance of the RCRT-1 Manipulator is consistency among two motion modes. Furthermore, the main benefit of this motion switching is speed of the movement that can be dramatically changed all the time. Nevertheless, these little error of movement prove that tracking-ability of this manipulator is good.

7.6.5 Virtual Fixture

The virtual wall can bound the movement of the slave manipulator to move inside the desire region effectively. Sometimes, the end-effector can penetrate the soft-wall and the hard-wall region for approximately 1 mm. The limited size of output forces allow some movements get into the prohibited region. However, the wall is strong enough to assist user in order to work in limited desired area.

7.6.6 User comfort

According to the test, the users with some practice was able to control the tip effectively with little attempt. However, only one view from the camera can be observed in the test. Therefore, the test was able to be done typically in the one plane (2D). In order to improve working capability, multiple camera system is necessary for the operation in the space (3D).

Moreover, the movement of the 5th and 6th axes was somewhat difficult to be controlled accurately. This problem is caused by inappropriate pulley-tendon mechanism.

CHAPTER VIII

CONCLUSIONS AND SUGGESTIONS

In the first section, the working performance of the RCRT-1 Manipulator is clearly presented. Moreover, tracking-ability determined from the errors in the master-slave operation is shown. Next, the problems of this manipulator and useful suggestion are discussed in the second section. Finally, the development plans and practical applications of this master-slave system are presented in the last section.

8.1 Conclusion

8.1.1 The performance of the RCRT-1 Manipulator

Precision and repeatability are determined from the position error in the steady state. These values can be acceptable especially in master-slave operation which the errors will be compensated by user automatically.

Table 8.1: Summary of the slave manipulator performance

Precision (mm)	0.514
Repeatability (mm)	0.005

8.1.2 Errors summary in the master-slave operation

These average and maximum value of position and orientation errors in the master-slave operation represent the tacking-ability of the system. In conclusion, there are little differences between two motion modes. Hence, it can be operated very well in any mode.

Table 8.2: Summary of error in master-slave operation

Error	GM = 1		GM = 0.1	
	Average (RMS)	Maximum	Average (RMS)	Maximum
Position (mm)	0.338	0.702	0.293	0.791
Roll (degree)	0.044	0.172	0.077	0.628
Pitch (degree)	0.092	0.828	0.105	0.832
Yaw (degree)	0.112	0.537	0.153	0.811

8.2 Problem and suggestions

8.2.1 Inaccuracy of the end-effector with respect to the 5th axis

The error is occurred from the 5th axis transmission. The tendon system is used in this axis. Because the actuator is located very far (approximately 30 cm) from the joint, the 0.1 mm nylon tendon is always stretched and extended. The tendon is extended immediately after the actuator start rotating. Consequently, it gradually gets to the normal length at last. These uncertainties act as backlashes which lead to an inaccuracy in the joint angle.

This problem can be solved by changing the tendon material, which has more flexibility and higher strength. The possible material is stainless steel wire.

8.2.2 Inaccuracy of the tip due to the 6h axis

The movement of the 6th axis is suffered from the complicated mechanism, which is coupled with the 5th axis. Because the size of the end-effector is very tiny, the well-polishing pins are used for the tendon arrangement in the wrist box. Some friction is occurred because of these small parts. Sometimes, too much friction obstructs the 6th-axis movement.

This problem requires the new mechanical adjustment, which rearranges the tendon transmission. Perhaps, a very tiny servo-actuator can be placed on the 5th-axis to drive the 6th axis directly in order to eliminate this problem. This solution can simplify the transmission mechanism also.

8.2.3 Inappropriate view of the visual system

Because the digital microscope is the only camera that provides the real-time image of the slave manipulator, the users can observe the operation in 2-D. Consequently, it is impossible to control the manipulator effectively in 3-D workspace.

Two or more cameras should be installed in the system in order to provide the 3-D vision.

8.3 Future works

8.3.1 Improve precision and accuracy

8.3.1.1 Calibration should be done in order to improve accuracy. Because the RCRT-1 Manipulator is designed based on the serial mechanism, the calibration process can be done easily by adding the important parameters in the kinematics model. Therefore, the exact parameters can be found by numerical methods.

8.3.1.2 Advanced control, e.g. inverse dynamics with robust control and adaptive control, should be implemented to the first three axes in order to improve accuracy. As regard to the first three links, they considerably influent on the overall accuracy because the lower arm is very long. In conclusion, the advanced control that deals with the complicated dynamics model can decrease overall error.

8.3.1.3 The tendon transmission for the 5th and the 6th axis should be more reliable. The high strength and easy-to-bend material should be used instead of the recent material. The high strength material, such as stainless steel, should be used. The appropriate size of this wire is smaller than 100 micron.

8.3.2 Development of the master – slave system

8.3.2.1 Intelligent movement regulation, for example jerk filtration and advanced virtual fixtures, will enhance the capability of the operation. As used in the MIS system, jerk filtration can reduce vibrant and prevent undesired movements from the surgeon mistakes.

The smart virtual fixture can provide the guiding paths that help the surgeon to operate easier. Moreover, more complicated shape of virtual walls should be considered.

8.3.2.2 Visual feedback with respect to stereo vision is one of the most important parts of the master-slave operation. The visual feedback provides more interaction between the users and environment. Moreover, the appropriate visual system allows the users to observe the operation in 3-D.

The small size digital microscopes with auto-focus should be used. Moreover, the cameras should be able to move freely around the working area by attaching them to another robot arm.

8.3.2.3 Another arm should be installed to this system in order to enhance the overall capability of manipulating objects. Two-arm system provides more dexterity and larger workspace.
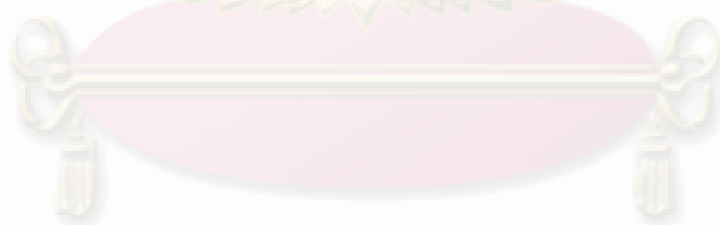
REFERENCE

[1] Mayo Foundation for Medical Education and Research. Minimally invasive surgery [Online]. Available from: http://www.mayoclinic.org/minimally-invasive-surgery, 2008.

[2] The Micromanipulator Company. Biological/MEMS manual manipulators[online]. Available from: http://www.micromanipulator.com/products, 2008.

[3] Blake Hannaford, James Hewitt, Thavida Maneewarn, Steven Venema, Matthew Appleby, and Robert Ehresman. Telerobotic macros for remote handling of protein crystals. Proceedings of the International Conference on Advanced Robotics ICAR97 July 1997.

[4] Venkata Raghavaiah Chowdharykode. Design and characterization of a novel hybrid actuator using shape memory alloy and dc motor for minimally Invasive surgery applications. M.S. Thesis. Department of Electrical Engineering and Computer Science Case Western Reserve University, January 2006.

[5] Intuitive Surgical Inc. The da Vinci surgical system[Online]. Available from: http://www.intuitivesurgical.com, 2008.

[6] Nabil Simaan, Russell Taylor. A dexterous system for laryngeal surgery. IEEE International Conference on Robotics & Automation April 2004.

[7] Iulian Iordachita, Ankur Kapoor, Ben Mitchell, Peter Kazanzides, Gregory Hager, James Handa, and Russell Taylor. Development and application of a new steady-hand manipulator for retinal surgery. IEEE International Conference on Robotics and Automation 2007.

[8] Mr.Natdanai Tantawiroon. Novel design and analysis with force control of the H-4family parallel manipulator. Ph.D.Dissertation. Department of Mechanical Engineering Chulalongkorn University, 2004.

[9]. Mitsubishi Heavy Industries Ltd. Mitsubishi PA-10[Online]. Available from: http://www.robot-arm.com, 2008.

[10] Motoman Yaskawa Company. Automated industrial robots[Online]. Available from: http://www.motoman.com, 2008.

[11] Adept Technology Inc. The fast and flexible Quattro[Online]. Available from: http://www.adept.com, 2008.

[12] Arne Burisch, Sven Soetebier, Jan Wrege, Rolf Slatter. Design of parallel hybrid micro-SCARA robot for high precision assembly. Lecture in Mechrob 1808,

Institute of Machine Tools and Production Technology (IWF), Technical University of Braunschweig, Germany, 2005.

[13] Goo Bong Chung, Jae Heon Chung, Dong Gul Choi, Byung-Ju Yi, Seok Young Han, and Seon Jung Kim. Development of a 5-DOF hybrid micro-manipulator and implementation to needle manipulation process in medical applications, Key Engineering Materials Vols. 326-328 (2006) : 773-776.

[14] Etsuko Kobayashi, Ken Masamun, Takeyoshi Dohi, and Daijo Hashimoto. A new laparoscope manipulator with an optical zoom. Proceedings of the First International Conference on Medical Image Computing and Computer-Assisted Intervention.

[15] Wikipedia. Backlash Gear[online]. Available from: http://en.wikipedia.org/wiki/Backlash_(gear), 2008.

[16] Harmonic Drive LLC. Operating Principles[Online]. Available from: http://www.harmonicdrive.net/reference/operatingprinciples, 2008.

[17] Gerry B. Andeen. Robot design handbook. SRI International. USA: McGraw-Hill Book Company, 1988.

[18] Faulhaber. Miniature drive system catalog. Faulhaber Group, 2005.

[19] Lung-Wen Tsai. Robot analysis: The mechanics of serial and parallel manipulators. A Wiley-Intersescience Publication. USA: John Wiley & Sons, 1999.

[20] Mark E. Rosheim. Robot wrist actuators. A Wiley-Intersescience Publication. USA: John Wiley & Sons, 1989.

[21] John J.Criag. Introduction to robotics: Mechanical and control. International Edition. 3rd ed. USA: Pearson Prentice Hall, 2005.

[22] SensAble Technologies Inc. PHANTOM Omni® Haptic Device[Online]. Available from: http://www.sensable.com/haptic-phantom-omni.htm, 2008.

[23] Mr. Tawee Ngamvilaikorn. Design and development of a master arm for force - reflecting system. M.Eng.Thesis. Department of Mechanical Engineering, Chulalongkorn University, 2001.

[24] SensAble Technologies Inc. Openhaptics™ toolkit version 2.0 : Programmer's guide. USA: SensAble Technologies Inc, 2006.

[25] Viboon Sangveraphunsiri. Control of Dynamic Systems. 2nd ed. Bangkok: Chulalongkorn University Press, 2003.

[26] ANMO Electronics Corporation. Dino Lite Digital Microscope Plus[Online]. Available from: http://www.anmo.com.tw/db/products-more.asp?id=33, 2008.

[27] K.S. Fu, R.C. Gonzalez*, and C.S.G. Lee. Robotics: Control, sensing,vision and intelligence. International edition. Singapore: McGraw-Hill Book Company, 1987

[28] HIWIN Linear Technology. Operating instructions linear stages with motor KK40, KK50, KK60, KK86, KK100, 2006.

[29] Lorenzo Sciavicco and Bruno Siciliano. Modeling and control of robot manipulators. Italy: McGraw-Hill Book Company, 1996.

[30] Jean-Jacques E. Slotine and Weiping Li. Applied nonlinear control. USA: Prentice-Hall Inc., 1991.

[31] Prasatporn Wongkamchang and Viboon Sangveraphunsiri. Control of inertial stabilization systems using robust inverse dynamics control and adaptive control. Ph.D. Dissertation. Department of Mechanical Engineering Chulalongkorn University, 2005.

[32] H. Asada and J.-J.E. Slotine. Robot Analysis and Control. A Wiley-Intersescience Publication. USA: John Wiley & Sons, 1986.

[33] Kummun Chooprasird and Viboon Sangveraphunsiri, Analytical kinematics and dynamics for 5 axis H-4 parallel manipulator. The 22nd Conference of ME Network of Thailand.

APPENDICES

ศูนย์วิทยทรัพยากร
จุฬาลงกรณ์มหาวิทยาลัย

APPENDIX A

MATHEMATICS

A.1 Kinematics

According to the Denavit-Hartenberg description and parameters, the forward kinematics can be calculated from the homogeneous transformation mapping method. All of the related transformation matrices are shown as follows.

$$
{}^0_1T = \begin{bmatrix} c_1 & 0 & -s_1 & 0 \\ s_1 & 0 & c_1 & 0 \\ 0 & -1 & 0 & 0 \\ \hline 0 & 0 & 0 & 1 \end{bmatrix}
\quad
{}^1_2T = \begin{bmatrix} c_2 & 0 & s_2 & 0 \\ s_2 & 0 & -c_2 & 0 \\ 0 & 1 & 0 & 0 \\ \hline 0 & 0 & 0 & 1 \end{bmatrix}
\quad
{}^2_3T = \begin{bmatrix} 1 & 0 & 0 & 0 \\ 0 & 1 & 0 & 0 \\ 0 & 0 & 1 & d_3 \\ \hline 0 & 0 & 0 & 1 \end{bmatrix}
$$

$$
{}^3_4T = \begin{bmatrix} c_4 & 0 & -s_4 & 0 \\ s_4 & 0 & c_4 & 0 \\ 0 & 1 & 0 & 0 \\ \hline 0 & 0 & 0 & 1 \end{bmatrix}
\quad
{}^4_5T = \begin{bmatrix} c_5 & 0 & s_5 & 0 \\ s_5 & 0 & -c_5 & 0 \\ 0 & 1 & 0 & 0 \\ \hline 0 & 0 & 0 & 1 \end{bmatrix}
\quad
{}^5_6T = \begin{bmatrix} c_6 & -s_6 & 0 & 0 \\ s_6 & c_6 & 0 & 0 \\ 0 & 0 & 1 & L_6 \\ \hline 0 & 0 & 0 & 1 \end{bmatrix}
$$

Then, the forward kinematics is expressed by:

$$
{}^0T_6\left(\theta_1,\theta_2,d_3,\theta_4,\theta_5,\theta_6\right) = {}^0_1T\,{}^1_2T\,{}^2_3T\,{}^3_4T\,{}^4_5T\,{}^5_6T = \begin{bmatrix} n_x & o_x & a_x & p_x \\ n_y & o_y & a_y & p_y \\ n_z & o_z & a_z & p_z \\ \hline 0 & 0 & 0 & 1 \end{bmatrix}.
$$

(a.1.1)

The closed-form solution of the forward kinematics is shown in Equation (4.4.1). The solution of R-R-P-R-R-R serial manipulator is presented in many documents, for example [32] H. Asada and J.-J.E. Slotine.

A.2 Trajectory generation

The trajectories are presented in the precision test (Chapter VII). They were generated with respect to the cubic polynomials, which is expressed as Equation (a.2.1).

$$\theta(t) = a_0 + a_1 t + a_2 t^2 + a_3 t^3 \qquad \text{(a.2.1)}$$

Assign the initial and final conditions as in Equation (a.3.2).

$$\theta(0) = \theta_0, \ \theta(t_f) = \theta_f, \ \dot{\theta}(0) = 0, \ \dot{\theta}(t_f) = 0 \qquad \text{(a.2.2)}$$

Then, find the constants a_0, a_1, a_2, and a_3 which satisfied Equation (a.2.1). The solutions are:

$$a_0 = \theta_0, \ a_1 = 0, \ a_2 = \frac{3}{t_f^2}(\theta_f - \theta_0), \ a_3 = -\frac{2}{t_f^2}(\theta_f - \theta_0) \qquad \text{(a.2.3)}$$

The angular velocity and acceleration are expressed as Equation (a.2.4) and (a.3.5)

$$\dot{\theta}(t) = a_1 + 2a_2 t + 3a_3 t^2 \qquad \text{(a.2.4)}$$

$$\ddot{\theta}(t) = 2a_2 + 6a_3 t \qquad \text{(a.2.5)}$$

(a)　　　　(b)
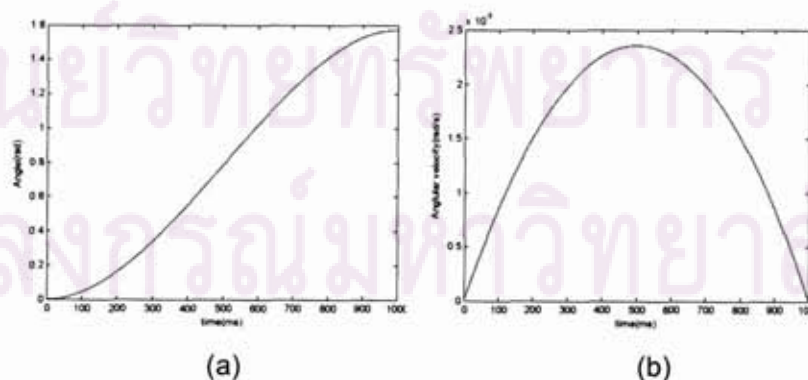
Figure A.1: Trajectory of (a) Position and (b) velocity

the position computed from the cubic polynomial equation

A.3 Dynamics model

Dynamics model of the first three axes of the RCRT-1 Manipulator has been derived from Lagrange-Euler formulation. The mechanical details of each main part, including mass, center of gravity, and inertia, are acquired from CAD model. In addition, the inertia of motor and the gear reduction ratio are modeled. However, some undesirable factors, especially friction force, have not been considered in this research.

The procedure of finding the dynamics model is explained as follows.

1) Construct the approximate CAD model and measure mechanical specifications, consist of mass, center of gravity, and inertia.

2) Compare these specifications to the actual measured value.

3) Find the value of the motor inertia and gear-reduction ratio from the catalog.

4) Follow the Lagrange-Euler formulation to find dynamics model.

According to the simple design, the 1st link (Figure A.3) and the 3rd link (Figure A.5) can be considered straightforwardly. On the other hand, two auxiliary links are presented in addition to the main 2nd link. However, the link-2b has little movement which produces little Coriolis force, centrifugal force, and gravity effect. As regard to the link-2a, it always moves in the same way as the 2nd link does. Hence the link-2b is neglected while the link-2a is attached to the 2nd link as shown in Figure A.4. This attachment does not affect the driving torque of the 2nd axis. The specifications of each link are shown in Table (A.2).
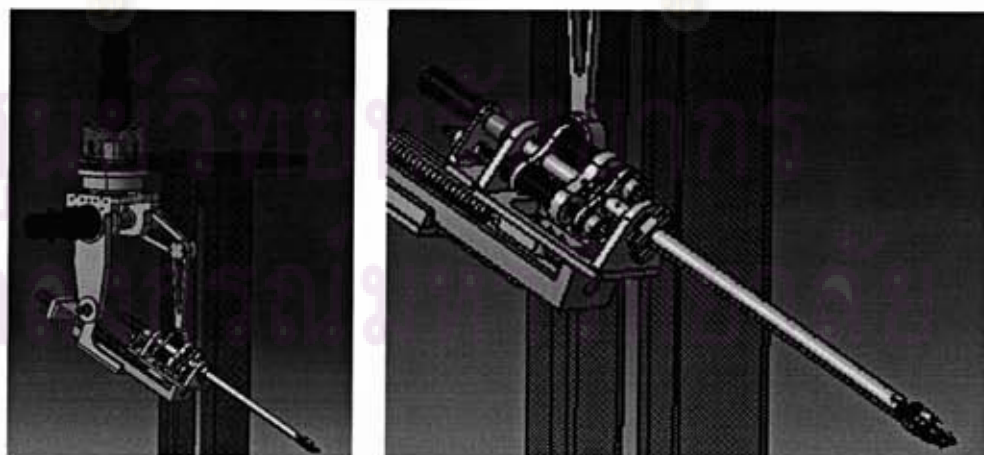
Figure A.2: The CAD model of the RCRT-1 Manipulator
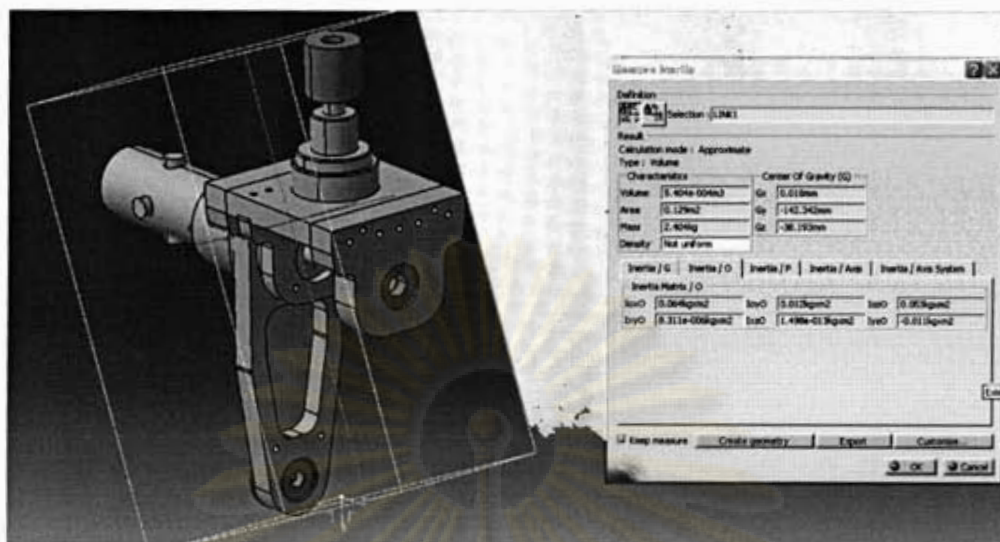
Figure A.3: The CAD model of Link-1
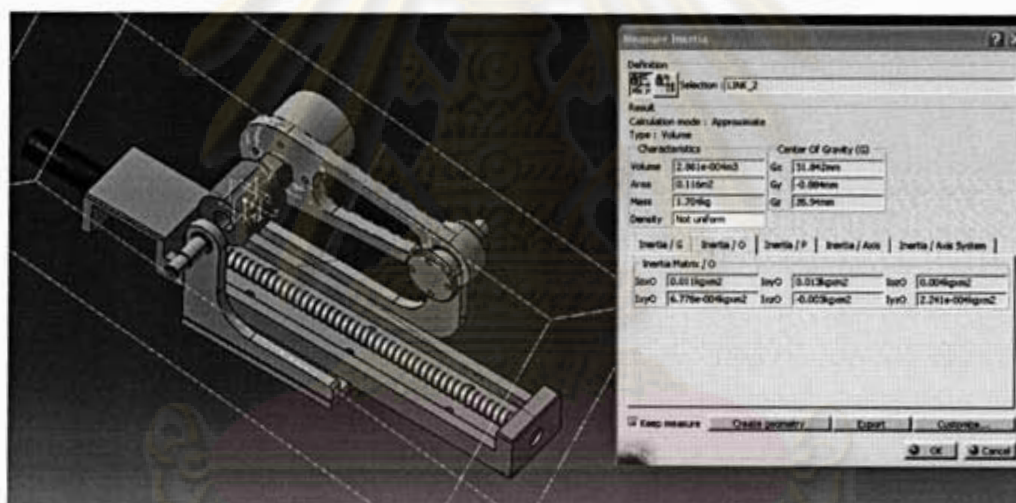
Figure A.4: The CAD model of Link-2
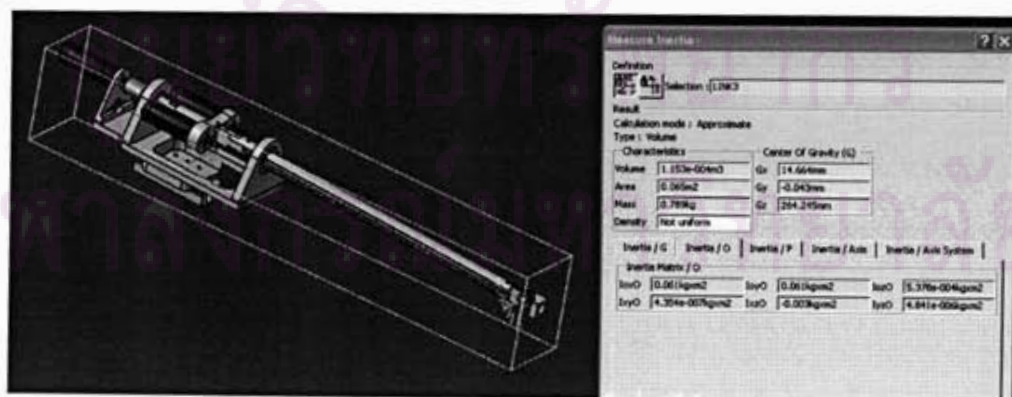
Figure A.5: The CAD model of Link-3

Table A.1: the approximate specifications of each link from CAD model

	Link #1	Link #2	Link #3	Unit
Mass (m_i)	2.404	1.704	0.789	kg
C.G. along x-axis ($\overline{x}_i$)	0	31.842	14.664	
C.G. along y-axis ($\overline{y}_i$)	-142.342	0	0	mm
C.G. along z-axis ($\overline{z}_i$)	-38.193	35.94	264.245	
I_{xx}	0.064	0.011	0.061	
I_{yy}	0.012	0.013	0.061	
I_{zz}	0.053	0.004	5.378×10^{-4}	
I_{xy}	0	6.778×10^{-4}	0	kg·m²
I_{xz}	0	3.0×10^{-3}	3.0×10^{-3}	
I_{yz}	-0.011	2.24×10^{-4}	0	
Motor inertia*	81.6	81.6	5.4	
Gear reduction ratio*	90:1	90:1	3.71	-

information from catalog

According to the Lagrange-Euler formulation (without considering friction force), the dynamics model is expressed as Equation (a.3.1) and each term is explained as follows.

$$\tau = \mathbf{D}(q)\ddot{q} + \mathbf{h}(q,\dot{q}) + \mathbf{c}(q) \tag{a.3.1}$$

τ represents computed torque for the revolute joint and computed force for the prismatic joint.

A.3.1 The acceleration-related symmetric matrix $\mathbf{D}(q)$

$$\mathbf{D}(q) = \begin{bmatrix} D_{11} & D_{12} & D_{13} \\ D_{21} & D_{22} & D_{23} \\ D_{31} & D_{32} & D_{33} \end{bmatrix} \tag{a.3.2}$$

Where

$$D_{ik} = \sum_{j=\max(i,k)}^{3} Tr\left(\mathbf{U}_{jk}\mathbf{J}_{j}\mathbf{U}_{ji}^{T}\right) \qquad i, k = 1, 2, 3 \qquad (a.3.3)$$

$$\frac{\partial^{0}\mathbf{A}_{i}}{\partial q_{j}} \triangleq \mathbf{U}_{ij} = \begin{cases} {}^{0}\mathbf{A}_{j-1}\mathbf{Q}_{j}{}^{j-1}\mathbf{A}_{i} & j \leq i \\ 0 & j > i \end{cases} \qquad i, j = 1, 2, 3$$

$$(a.3.4)$$

${}^{i}\mathbf{A}_{j}$ = transformation matrix j with respect to frame j

$\mathbf{J}_{i}$ = inertia tensor, which i = 1, 2, 3

$$\mathbf{J}_{i} = \begin{bmatrix} \dfrac{-I_{xx} + I_{yy} + I_{zz}}{2} & I_{xy} & I_{xz} & m_{i}\bar{x}_{i} \\[2mm] I_{xy} & \dfrac{I_{xx} - I_{yy} + I_{zz}}{2} & I_{yz} & m_{i}\bar{y}_{i} \\[2mm] I_{xz} & I_{yz} & \dfrac{I_{xx} + I_{yy} - I_{zz}}{2} & m_{i}\bar{z}_{i} \\[2mm] \hline m_{i}\bar{x}_{i} & m_{i}\bar{y}_{i} & m_{i}\bar{z}_{i} & m_{i} \end{bmatrix} \qquad (a.3.5)$$

$\mathbf{Q}_{i}$ is expressed as the 4×4 matrix that depended on the type of each joint, which are:

For a revolute joint: $\mathbf{Q}_{i} = \begin{bmatrix} 0 & -1 & 0 & 0 \\ 1 & 0 & 0 & 0 \\ 0 & 0 & 0 & 0 \\ 0 & 0 & 0 & 0 \end{bmatrix}$ \qquad (a.3.6)

For a prismatic joint: $\mathbf{Q}_{i} = \begin{bmatrix} 0 & 0 & 0 & 0 \\ 0 & 0 & 0 & 0 \\ 0 & 0 & 0 & 1 \\ 0 & 0 & 0 & 0 \end{bmatrix}$ \qquad (a.3.7)

A.3.2 The Coriolis and centrifugal terms $\mathbf{h}(q,\dot{q})$

$$\mathbf{h}(q,\dot{q}) = \begin{bmatrix} h_1 \\ h_2 \\ h_3 \end{bmatrix} \tag{a.3.8}$$

Where

$$h_1 = \left(h_{112}+h_{121}\right)\dot{\theta}_1\dot{\theta}_2 + \left(h_{113}+h_{131}\right)\dot{\theta}_1\dot{\theta}_3 + \left(h_{123}+h_{132}\right)\dot{\theta}_2\dot{\theta}_3 + h_{122}\dot{\theta}_2^2 + h_{133}\dot{\theta}_3^2$$

$$h_2 = \left(h_{212}+h_{221}\right)\dot{\theta}_1\dot{\theta}_2 + \left(h_{213}+h_{231}\right)\dot{\theta}_1\dot{\theta}_3 + \left(h_{223}+h_{232}\right)\dot{\theta}_2\dot{\theta}_3 + h_{211}\dot{\theta}_1^2 + h_{133}\dot{\theta}_3^2$$

$$h_3 = \left(h_{312}+h_{321}\right)\dot{\theta}_1\dot{\theta}_2 + \left(h_{313}+h_{331}\right)\dot{\theta}_1\dot{\theta}_3 + \left(h_{323}+h_{332}\right)\dot{\theta}_2\dot{\theta}_3 + h_{311}\dot{\theta}_1^2 + h_{322}\dot{\theta}_3^2$$

Each term is computed from the following equations.

$$h_{ikm} = \sum_{j=\max(i,k,m)}^{3} Tr\left(\mathbf{U}_{jkm}\mathbf{J}_j\mathbf{U}_{ji}^T\right) \qquad \text{i, k, m} = 1, 2, 3 \tag{a.3.9}$$

$$\frac{\partial \mathbf{U}_{ij}}{\partial q_k} \Box \, \mathbf{U}_{ijk} = \begin{cases} {}^0\mathbf{A}_{j-1}\mathbf{Q}_j{}^{j-1}\mathbf{A}_{k-1}\mathbf{Q}_k{}^{k-1}\mathbf{A}_i, & i \geq k \geq j \\ {}^0\mathbf{A}_{k-1}\mathbf{Q}_k{}^{k-1}\mathbf{A}_{j-1}\mathbf{Q}_j{}^{j-1}\mathbf{A}_i, & i \geq j \geq k \\ 0 & i < j \ \text{or} \ i < k \end{cases} \tag{a.3.10}$$

A.3.3 The gravity terms $\mathbf{c}(q)$

$$\mathbf{c}(q) = \begin{bmatrix} C_1 \\ C_2 \\ C_3 \end{bmatrix} \tag{a.3.11}$$

Where

$$C_i = \sum_{j=1}^{3}\left(-m_j\mathbf{g}\mathbf{U}_{ji}{}^j\overline{r}_j\right) \qquad \text{i} = 1, 2, 3 \tag{a.3.12}$$

$\mathbf{g}$ = gravity constant vector

${}^j\overline{r}_j$ = center of gravity location with respects to itself

After every term was computed, substitute them in Equation (a.3.1). The computed force of the 3rd axis (a prismatic joint) actually needs to transform to the computed torque for commanding the motor. Using Equation (a.3.13) or (a.3.14) depends on the moving direction. Equation (a.3.13) is used when the ball-screw is driven upward because the additional force is needed to overcome the self-locking characteristic. On the other hand, Equation (a.3.14) is used for the opposite direction.

$$\tau_i = \frac{F_i D_p}{2}\left[\frac{L_d + \mu\pi D_p}{\pi D_p - \mu L_d}\right] + \left(J_{motor} + J_{screw}\right)\left(\frac{2\pi\ddot{d_i}}{L_d}\right) + \tau_{friction} \qquad (a.3.13)$$

$$\tau_i = \frac{F_i D_p}{2}\left[\frac{\mu\pi D_p - L_d}{\pi D_p + \mu L_d}\right] + \left(J_{motor} + J_{screw}\right)\left(\frac{2\pi\ddot{d_i}}{L_d}\right) - \tau_{friction} \qquad (a.3.14)$$

Where

D_p = pitch diameter of ball screw = 7 mm

L_d = lead of the screw in mm per revolution = 1mm

μ = coefficient of friction for rolling contact = 0.01687

$J_{motor} + J_{screw}$ = Inertia of motor and ball screw = 6.627×10^{-7} kg·m^2 [33]

$\tau_{friction}$ = overall resistance torque

Finally, the solution of dynamics model is shown in Equation (4.6.3) to (4.6.8).

A.4 Overall resolution of the RCRT-1 Manipulator

The overall resolution has been typically computed with respect to the first three joints. The other joints have been neglected.

From Equation (3.3), resolution of the 1st and the 2nd axis are in Equation (a.4.1) and (a.4.2), respectively.

$$resolution_{axis-1} = \left(\frac{2\pi}{90 \times 1000 \times 4} \right) \cdot 460mm = 8.029 \times 10^{-3}mm \qquad (a.4.1)$$

$$resolution_{axis-2} = \left(\frac{2\pi}{90 \times 1000 \times 4} \right) \cdot 460mm = 8.029 \times 10^{-3}mm \qquad (a.4.2)$$

From Equation (3.2), resolution of the 3rd axis (prismatic joint) is:

$$resolution_{axis-3} = \frac{1mm}{3.71 \times 512 \times 4} = 1.316 \times 10^{-4}mm \qquad (a.4.3)$$

From Equation (3.4) and Equation (a.4.1) – (a.4.3), the overall resolution of the manipulator is:

$$resolution_{overall\ manipulator} = \sqrt{\left(8.029 \times 10^{-3}\right)^2 + \left(8.029 \times 10^{-3}\right)^2 + \left(1.316 \times 10^{-4}\right)^2}$$

$$= 11.355 \times 10^{-3}mm \qquad (a.4.4)$$

ศูนย์วิทยทรัพยากร

จุฬาลงกรณ์มหาวิทยาลัย

APPENDIX B

MECHANICAL & ELECTRICAL HARDWARE

B.1 Harmonic drive DC servo motor

The RH-14D-GH1 Hi-T Drive servo motor provides 18.5 W output power. Meanwhile, it is attached with 90:1 reduction ratio harmonic gears. This motor is produced by Harmonic Drive System Inc. These of motors are mounted on the slave manipulator for driving the first two joints. Moreover, the 1000 ppr optical incremental encoder from HONTKO is mounted on each motor for angular displacement sensing.

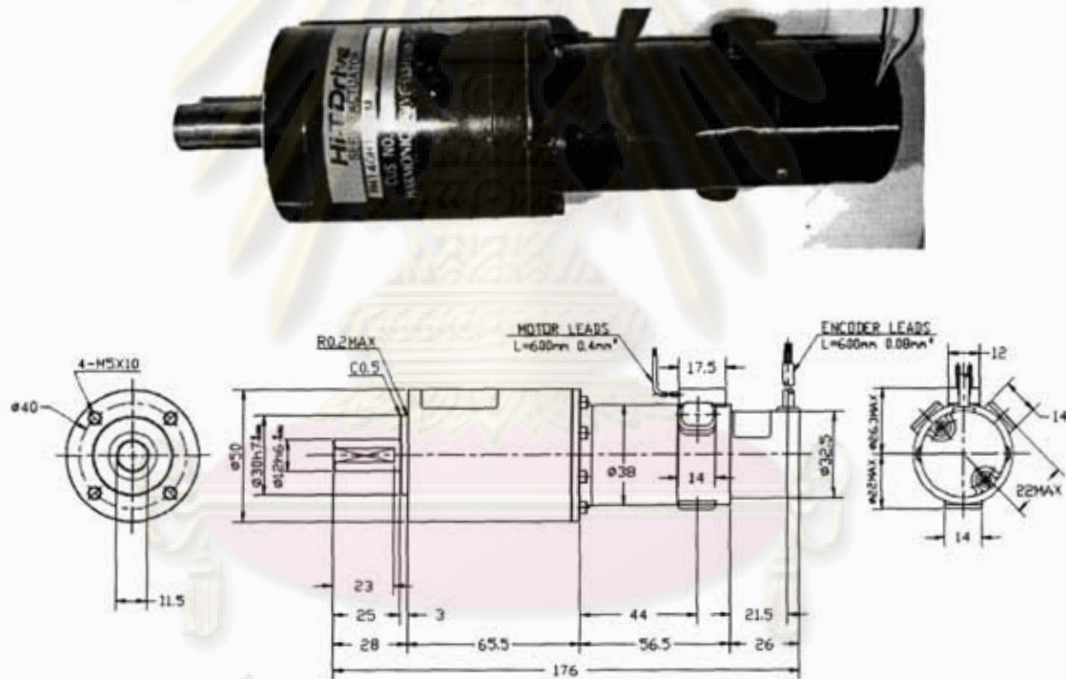Figure B.1: RH-14D-GH1 Hi-T Drive servo motors

B.2 Miniature zero backlash motor

Mini sized servo motors with zero-backlash gear heads, from Faulhaber Company, drive the 3rd to the 6th joints of the RCRT-1 Manipulator. Variety combinations among actuator models, gear heads, and magnetic incremental encoders were selected

to meet each joint requirement. The selected motor system for each joint is shown in Table B.1.

Figure B.2: Faulhaber miniature motor with zero backlash gear head

Table B.1: Miniature zero backlash Motors for the 3rd to the 6th axis

joint	motor		encoder		Gear head	
	Model	Power (W)	Model	Resolution (ppr)	Model	Reduction ratio
3	1624012SR	1.44				3.71:1
4	1524E012SR	1.75	IE-512	512	15/8	141:1
5,6						76:1

B.3 Absolute encoder

The MAE3 is a 10-bits analog output absolute encoder manufactured by the US Digital company, is used for indicating the slave manipulator's home position. This encoder is well designed, leading to the simple assembly. I can also accept little shaft misalignment. This encoder is tiny, high sampling rate, and low-cost.

Figure B.3: MAE3 absolute encoder from US Digital Company

B.4 Linear stage (Ball-screw and linear slide)

The KK40 01P 200 A1 F0 is a high precision linear stage with 200 mm rail length in the KK40 series from HIWIN. It is used as the prismatic joint of the RCRT-1 Manipulator. The screw has 1mm-lead. Hence the linear stage can provide high precision, ± 0.003 mm repeatability and 0.010 mm accuracy.

Figure B.4: KK40 linear stage from HIWIN Company

B.5 Power amplifier

The power amplifiers, model 4122P from Copley Control Corp., are used for amplifying electrical current. All joint in the RCRT-1 Manipulator are driven by these devices. It can continuously supply 10A current and 20A for 2 seconds as a peak current. Six amplifiers are used in this research with the constant 24 V supplied from the external 240 W power supply.
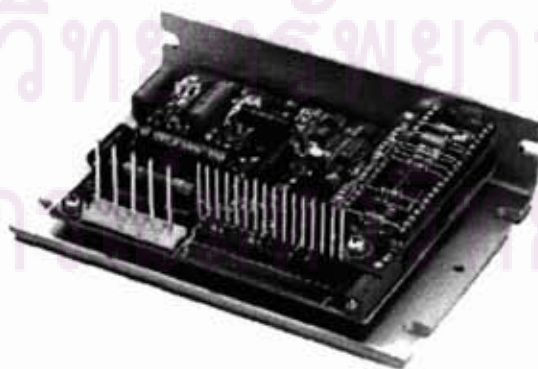
Figure B.5: Power amplifier 4122P: Copley Control Corp.

B.6 Dino-Lite digital microscope

The Dino-Lite plus is a compact portable digital microscope from ANMO Electronics Corporation. It provides 20X - 230X magnification with 30 - 45 fps. This microscope can be connected to the computer via USB port and captures the real time image. It is always fixed on the base of the RCRT-1 Manipulator in order to capture the real-time image during operations.

Figure B.6: Dino-Lite Plus digital Microscope

Figure B.7: User interface of Dino-Lite

APPENDIX C

PC INTERFACE I/O PORT CONNECTION

Table C.1: Control box 1

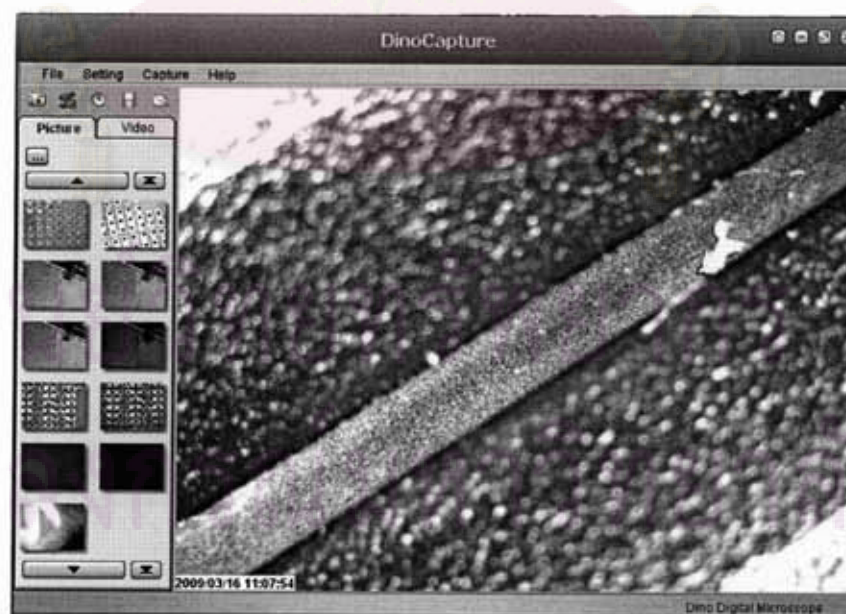|		module	description	pin No. (sensoray)	pin No. (port)	wire
BOARD 1	J4	encoder#1	5V	6	14	RED
			GND	3	15	BLACK
			A	2	1	VIOLET
			B	5	2	VIOLET/
		encoder#2	5V	12	16	RED/
			GND	9	17	BLACK/
			A	11	3	BLUE
			B	14	4	BLUE/
		encoder#3	5V	24	18	ORANGE
			GND	21	19	BROWN
			A	20	5	AQUA
			B	23	6	AQUA/
	J5	encoder#4	5V	6	20	ORANGE/
			GND	3	21	BROWN
			A	2	7	AQUAMARINE
			B	5	8	AQUAMARINE/
		encoder#5	5V	12	22	PINK
			GND	9	23	BLACK
			A	11	9	GREEN
			B	14	10	GREEN/
		encoder#6	5V	24	24	PINK/
			GND	21	25	BLACK
			A	20	11	YELLOW
			B	23	12	YELLOW/
	J1	DAC#1	V	42		GREEN
			GND	37		YELLOW
		DAC#2	V	44		GREEN
			GND	38		YELLOW
		DAC#3	V	46		GREEN
			GND	39		YELLOW

Table C.1: Control box 1 (continue)

		module	description	pin No.		wire
				(sensoray)	(port)	
BOARD 1 (continue)	J1	ADC#1	AD0+	4	1	ORANGE
			AD0-	3		
		ADC#2	AD1+	6	3	ORANGE/
			AD1-	5		
		ADC#3	AD2+	8	5	BROWN
			AD2-	7		
		ADC#4	AD3+	10	7	BROWN/
			AD3-	9		
		ADC#5	AD4+	8	9	PINK
			AD4-	7		
		ADC#6	AD5+	10	11	PINK/
			AD5-	9		
			V		14,19	RED
			GND	2,19,20	20	WHITE
BOARD 2	J1	DAC#4	V	42		GREEN
			GND	37		YELLOW
		DAC#5	V	44		GREEN
			GND	38		YELLOW
		DAC#6	V	46		GREEN
			GND	39		YELLOW
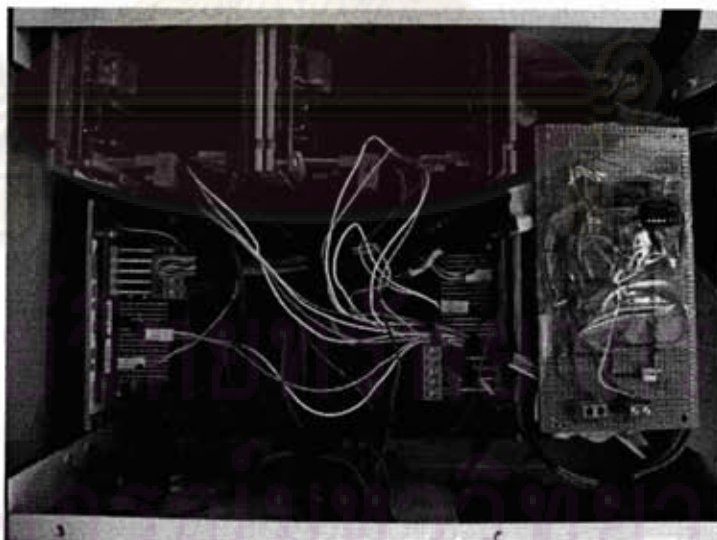
Figure C.1: The Control box 1

Table C.2: Control box 2

pin	from box1	description	description	from box1	pin
1	VIOLET	1A	V+	RED	14
2	VIOLET/	1B	GND	BLACK	15
3	BLUE	2A	V+	RED/	16
4	BLUE/	2B	GND	BLACK/	17
5	AQUA	3A	V+	ORANGE	18
6	AQUA/	3B	GND	BROWN	19
7	AQUAMARINE	4A	V+	ORANGE/	20
8	AQUAMARINE/	4B	GND	BROWN	21
9	GREEN	5A	V+	PINK	22
10	GREEN/	5B	GND	BLACK	23
11	YELLOW	6A	V+	PINK/	24
12	YELLOW/	6B	GND	BLACK	25

pin	from box1	description
1	ORANGE	analog-1
3	ORANGE/	analog-2
5	BROWN	analog-3
7	BROWN	analog-4
9	PINK	analog-5
11	PINK/	analog-6
14	RED 14,19	V+
20	WHITE 20,25	GND

Figure C.2: Control box 2
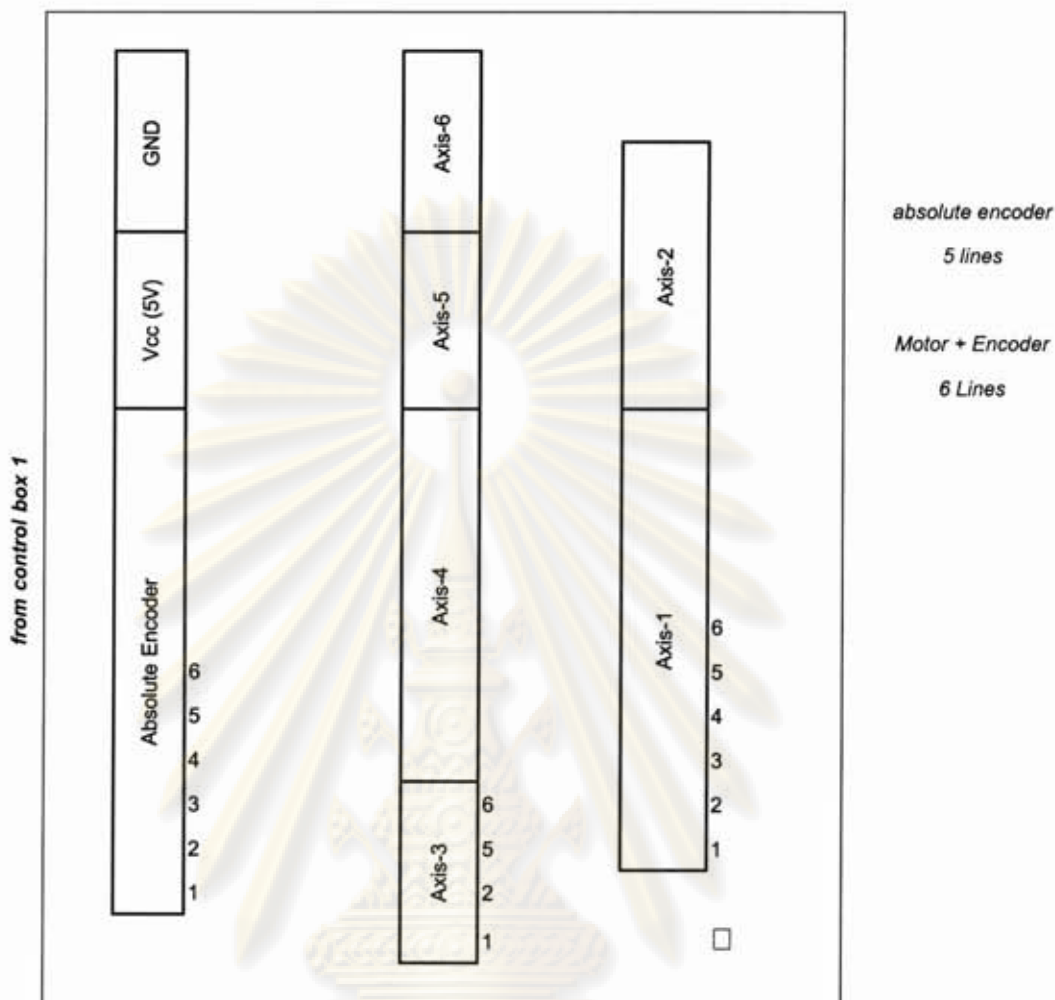
Figure C.3: Control box 2 (diagram)

Table C.3: Lines from Control box 2 to each motor

*pin	description	line
1	M-	Black
2	M+	Red
3	GND	White
4	Vcc	Yellow
5	A	Brown
6	B	Green

* pin order refers to FAULHABER catalog [18]
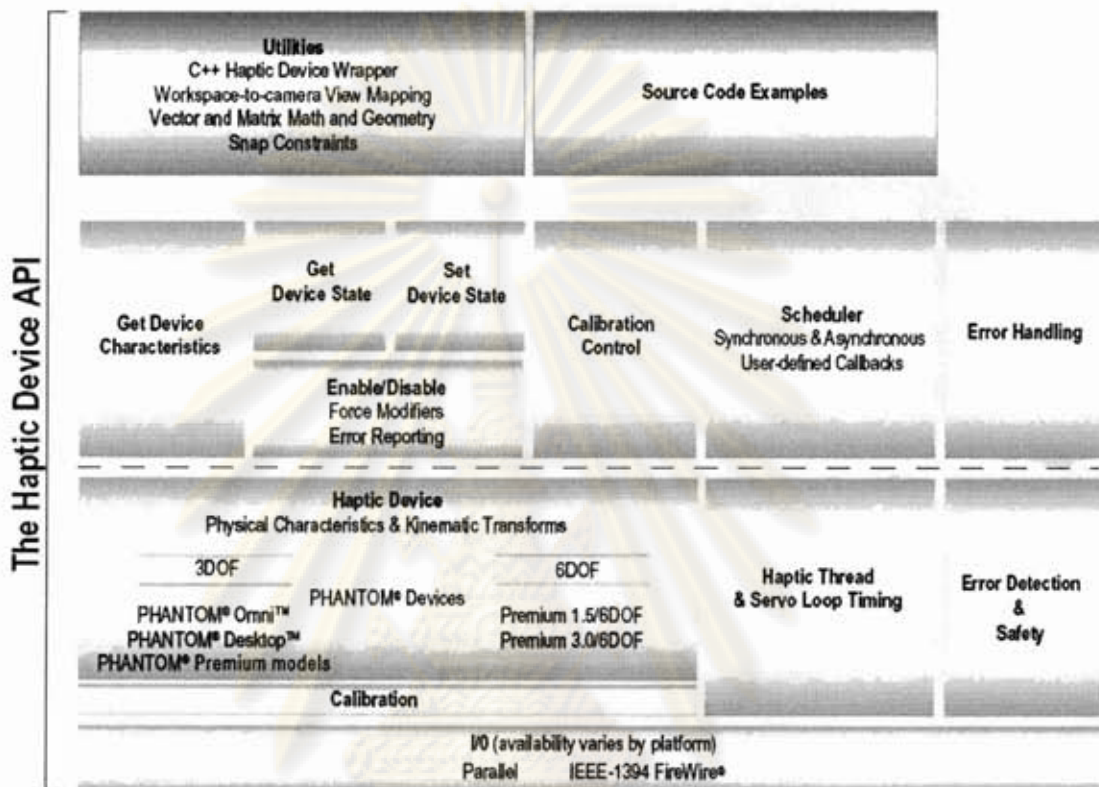
APPENDIX D

PHANTOM HDAPI

Figure D.1: The chart of the overall functions of HDAPI

ศูนย์วิทยทรัพยากร

จุฬาลงกรณ์มหาวิทยาลัย

APPENDIX E

ADDITIONAL EXPERIMENTS AND RESULTS

E.1 Accuracy test (Detail)

The accuracy of this manipulator is approximated from the position error of the end-effector in steady state. The error is the difference between "the actual position from measurement" and "the desired position". The actual positions are measured from a standard ruler (0.5 mm resolution). This ruler is attached to the platform of the manipulator.

These errors represent how exact of the parameters in the kinematics equations. The purpose of this test is to roughly prove that the manipulator can be moved in the proper direction with some accuracy.

E.1.1 The procedure of the test

In brief, the slave manipulator is controlled to move to the reference points. Afterwards, the position errors are calculated. The gains of the controller are different from that of the other tests. The gain was adjusted in order to totally eliminate the steady state error (without considering of the tracking-ability).

The test was done in three directions along the coordinated axes. In each axis, 10 reference points are located every 10 mm incremental along the axis. For X and Z directions, the end-effector can be moved directly from home position to these reference points. As regard to the Y-direction, the end-effector has to move to the escape position first because it reaches the boundary singularity. Figure E.1 presents position of the reference points. Moreover, the orientation of the end-effector is set to be parallel to the X-axis of coordinate frame {0} at each reference point. The typical procedure of the test is described as follows:

1) Determine the fixed reference points, which the exact positions with respect to the frame {0} (the base frame of the manipulator) are known from measurement.

2) Compute the joint angles of this fixed point by inverse kinematics.

3) Operate the manipulator to move from home position to this location.

4) Wait until the manipulator approach the steady state. Measure the actual distance that the end-effector moves. (Measure by the ruler)

5) Compare the actual position to the desired position.

6) Repeat this procedure for 10 incremental values for each axis.
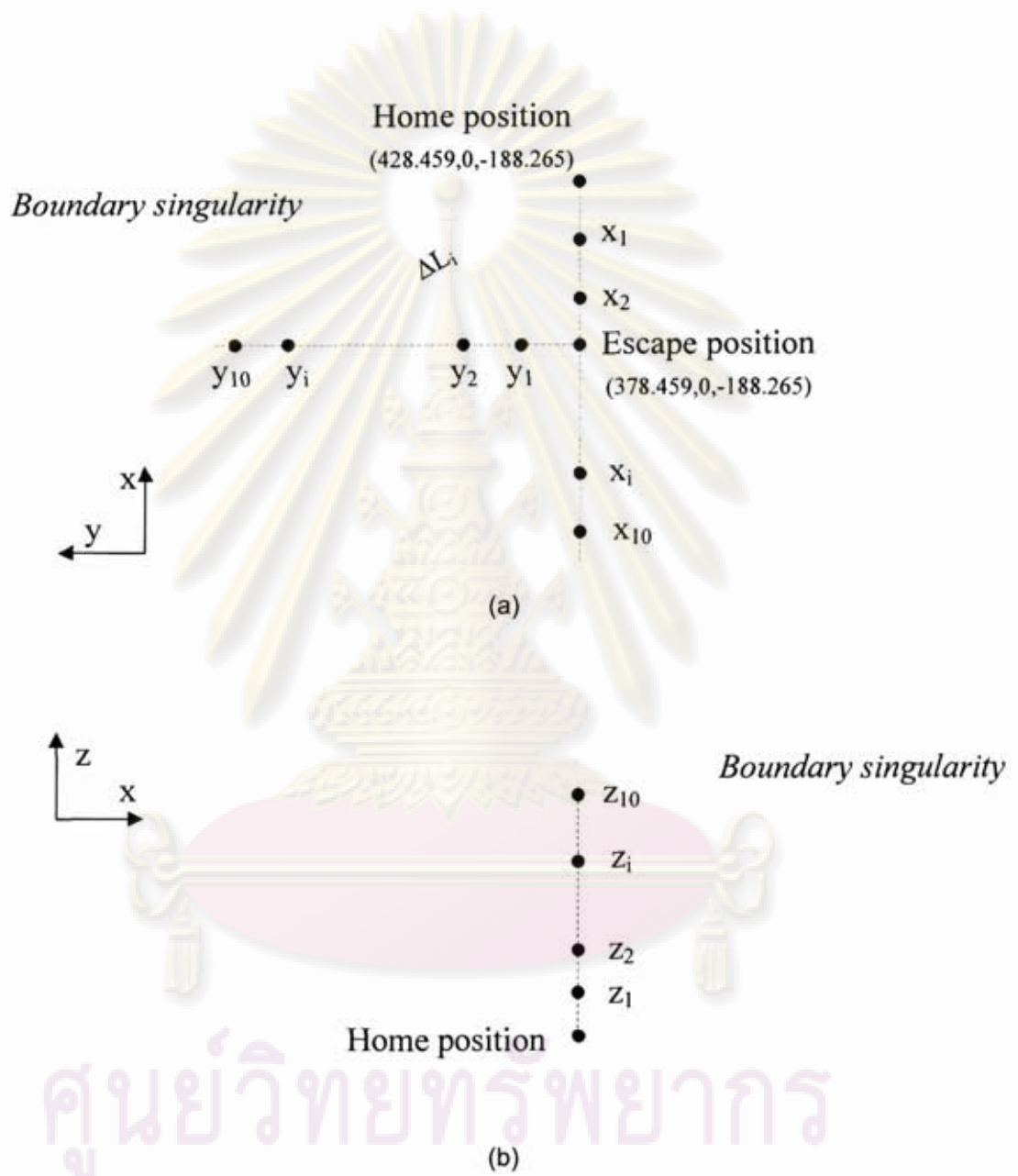

Figure E.1: Reference positions along three directions
(a) XY-plane (b) ZX-plane

E.1.2 Test results

Table E.1: Actual errors of the end-effector for the X-direction movement

No.	Distance moved in X-direction		Error (mm)
	Desired	Actual Δx	
1	10.00	10.25	-0.25
2	20.00	20.00	0.00
3	30.00	30.00	0.00
4	40.00	40.25	-0.25
5	50.00	50.25	-0.25
6	60.00	60.50	-0.50
7	70.00	70.50	-0.50
8	80.00	79.50	0.50
9	90.00	90.00	0.00
10	100.00	100.25	-0.25
		Average (RMS)	0.32
		S.D.	0.29

Table E.1 presents the actual error in X-direction. The RMS average of the actual error is 0.32 mm. The S.D. of the actual error is 0.29 mm. The absolute maximum error was 0.50 mm.

Table E.2: Actual errors of the end-effector for the Y-direction movement

No.	Distance moved in Y-direction (mm)			Error (mm)
	Desired	Measurement		
		From home	Actual Δy *	
1	10.00	31.50	9.61	0.39
2	20.00	36.00	19.90	0.10
3	30.00	43.00	30.81	-0.81
4	40.00	50.50	40.62	-0.62
5	50.00	58.50	50.22	-0.22
6	60.00	68.00	61.03	-1.03
7	70.00	77.00	70.92	-0.92
8	80.00	86.50	81.13	-1.13

9	90.00	96.00	91.19	-1.19
10	100	105.50	101.15	-1.15
			Average (RMS)	0.85
			S.D.	0.56

* Note Δy is calculated from $\Delta y = \sqrt{(\Delta y)^2 - (30.00)^2}$ (see Figure E.1(a))

Table E.2 presents the actual error in Y-direction. The RMS average of the actual error is 0.85 mm. The S.D. of the actual error is 0.56 mm. The absolute maximum error was 1.19 mm. The further calculation of Δy may lead to some errors.

Table E.3: Actual errors of the end-effector for the Z-direction movement

| No. | Distance moved in X-direction | | Error (mm) |
	Desired	Actual Δz	
1	10.00	10.00	0.00
2	20.00	20.00	0.00
3	30.00	29.50	0.50
4	40.00	40.50	-0.50
5	50.00	50.50	-0.50
6	60.00	60.00	0.00
7	70.00	71.00	-1.00
8	80.00	81.00	-1.00
9	90.00	91.75	-1.75
10	100.00	102.00	-2.00
	Average (RMS)		0.99
	S.D.		0.81

Table E.3 presents the actual error in Z-direction. The RMS average of the actual error is 0.99 mm. The S.D. of the actual error is 0.81 mm. The absolute maximum error was 1.75 mm.

Table E.4: Position errors summary

Position error (mm)	Average(RMS)	S.D.	Maximum (absolute value)
X	0.32	0.29	0.50
Y	0.85	0.56	1.19
Z	0.99	0.81	2.00

In summary, as the summary in Table 7.4, the RMS of the error in each direction was less than 1 mm. The maximum absolute error was 2.00 mm. This value was occurred in the Z-direction. Overall, the accuracy determined from the maximum value which is 2.00 mm. This value can be acceptable as regard to the main purpose of this manipulator, the master-slave operation. However, the accuracy can be improved by calibration.

E.2 Responses of the joint angles (in precision test)

The time response the joint angles of each final reference point are presented.
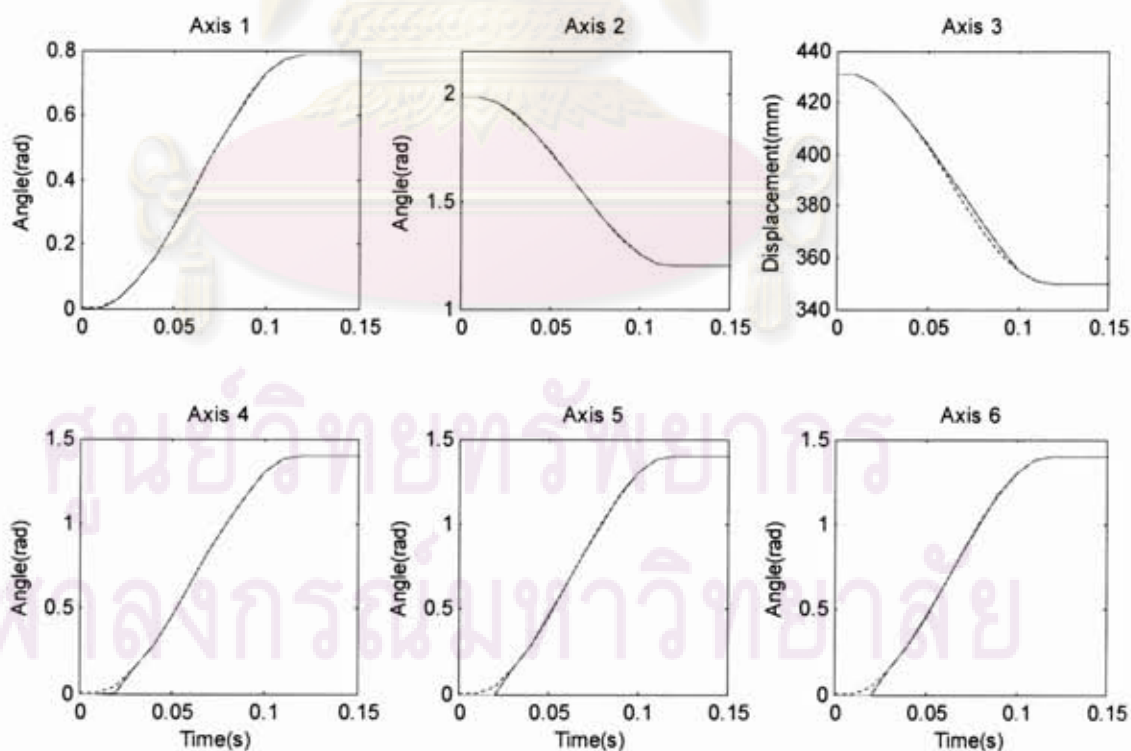
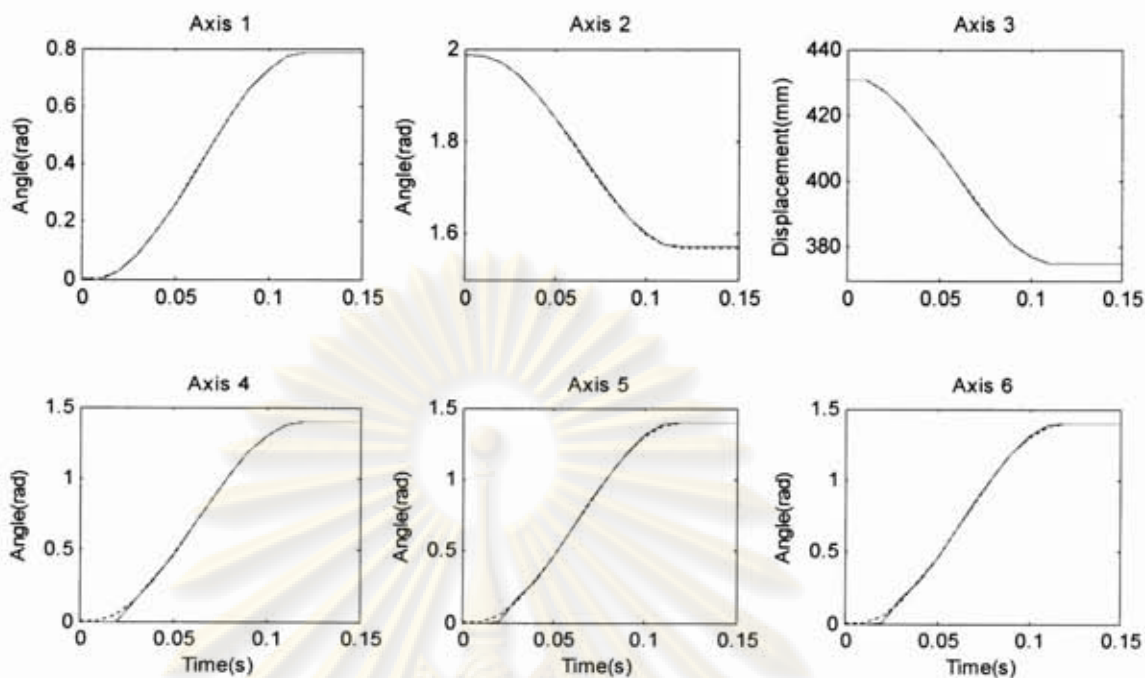Figure E.1: Joint angles (point No.1) - - - - - Reference ———— Actual

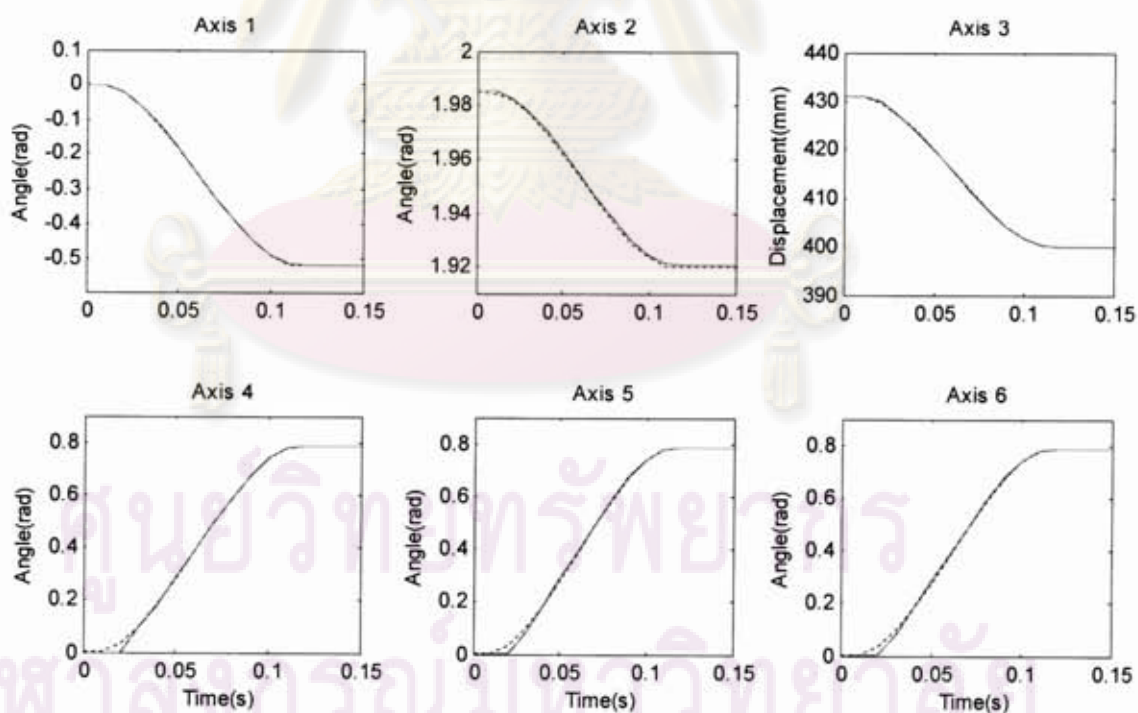Figure E.2: Joint angles (point No.2) ----- Reference ——— Actual

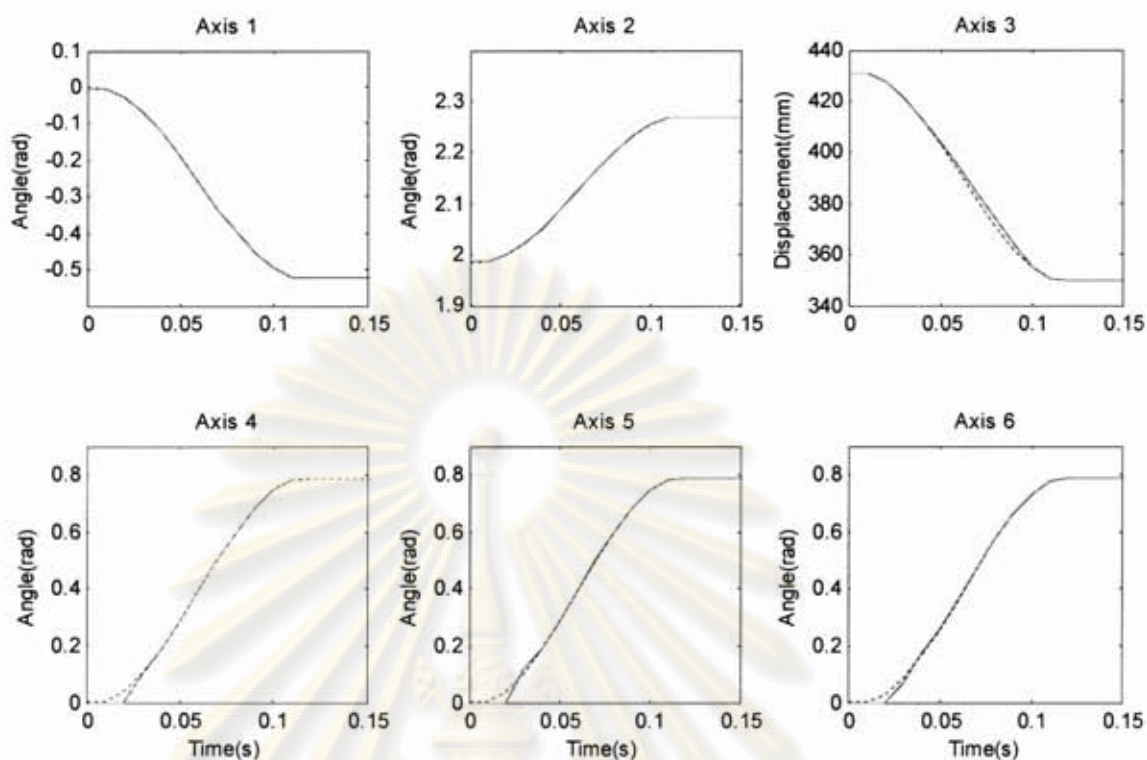FigureE.3: Joint angles (point No.3) ----- Reference ——— Actual

Figure E.4: Joint angles (point No.4) - - - - Reference ——— Actual
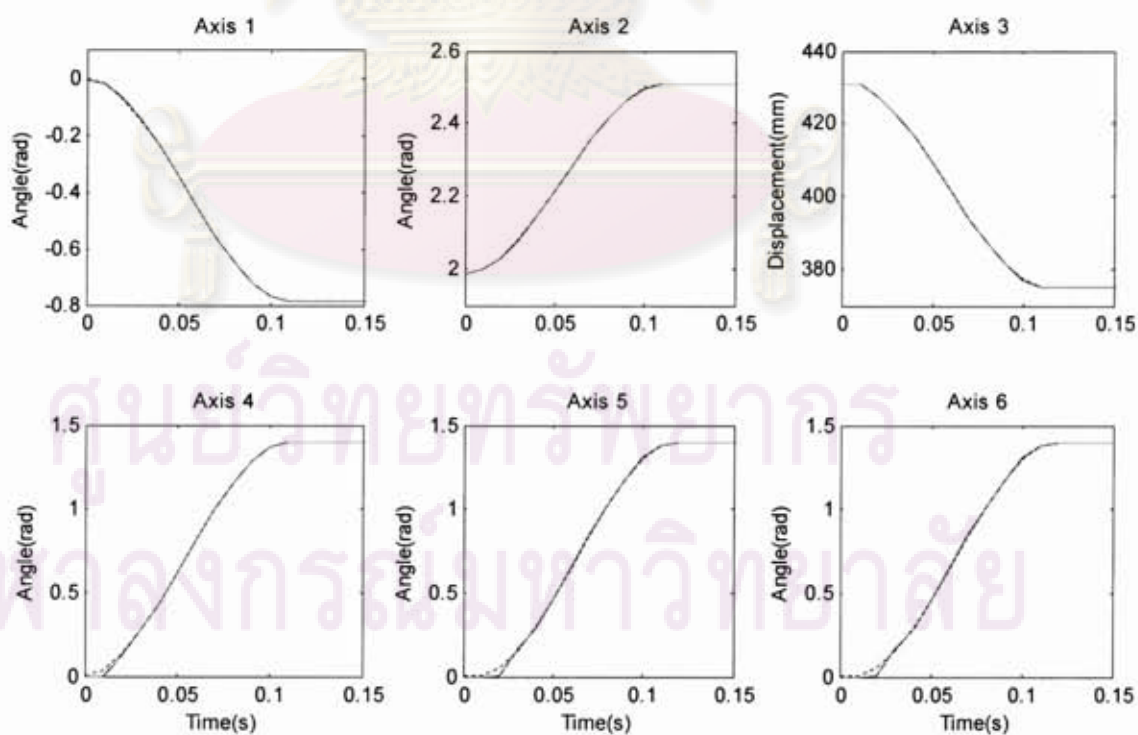

FigureE.5: Joint angles (point No.5) - - - - Reference ——— Actual
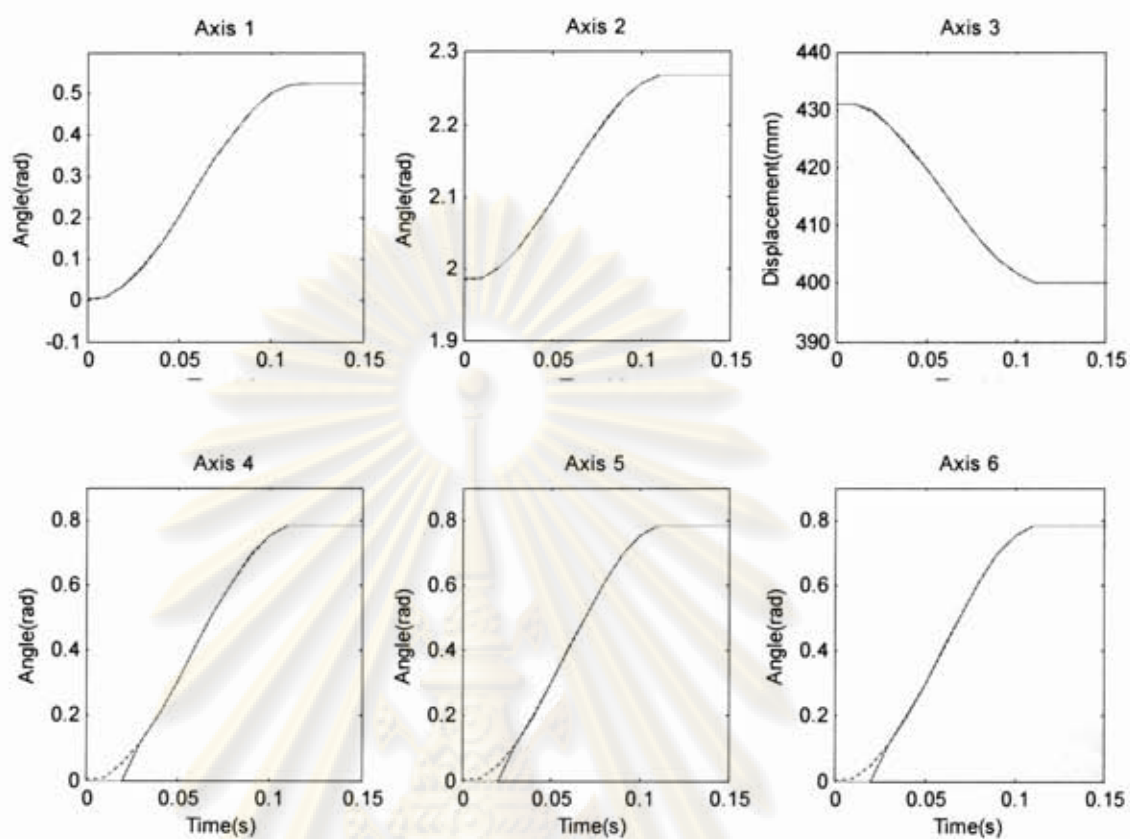
FigureE.6: Joint angles (point No.6) ----- Reference ——— Actual

BIOGRAPHY

Supachai Vongbunyong was born on November 17, 1983 in Bangkok, Thailand. He obtained his Bachelor's Degree in Mechanical Engineering in 2005 at Chulalongkorn University. Afterwards in 2006, he continued attending Master of Engineering program at this university.